AGU PUBLICATIONS

JGR

Journal of Geophysical Research: Solid Earth

RESEARCH ARTICLE

10.1002/2013JB010697

Key Points:
- Complete study of the earthquake cycle in the area of the Tohoku earthquake
- Inversion performed using a new inversion method
- The coseismic, postseismic, and interseismic phases are studied consistently

Correspondence to:
H. Perfettini,
hugo.perfettini@ird.fr

Citation:
Perfettini, H., and J. P. Avouac (2014), The seismic cycle in the area of the 2011 M_w9.0 Tohoku-Oki earthquake, *J. Geophys. Res. Solid Earth*, *119*, 4469–4515, doi:10.1002/2013JB010697.

Received 23 SEP 2013
Accepted 31 MAR 2014
Accepted article online 3 APR 2014
Published online 27 MAY 2014

The seismic cycle in the area of the 2011 M_w9.0 Tohoku-Oki earthquake

H. Perfettini[1,2] and J. P. Avouac[3]

[1]IRD, Grenoble, France, [2]ISTerre, University of Grenoble Alpes, Grenoble, France, [3]Tectonics Observatory, Caltech, Pasadena, California, USA

Abstract We model seismic and aseismic slip on the Japan megathrust in the area of the M_w9.0, 2011 Tohoku-Oki earthquake based on daily time series from 400 GPS stations of the GEONET network and campaign measurements of six sea floor displacements. The coseismic and postseismic slip distributions are inverted simultaneously using principal component analysis-based inversion method (PCAIM). Exploring a wide range of boundary conditions and regularization constraints, we found the coseismic slip distribution to be quite compact with a peak slip between 30 and 50 m near the trench. Our model shows deep afterslip fringing the downdip edge of the coseismic rupture but also a dominant zone of shallow afterslip. Afterslip over the first 279 days following the main shock represents about 40% of the coseismic moment. We compare the coseismic and postseismic models with an interseismic coupling model derived from inland and sea bottom measurements determined in a self-consistent manner. Assuming that seismic and aseismic slip had to match the long-term slip rate along the megathrust, the recurrence time of M_w9.0 earthquakes is estimated to 100–300 years, while historical and paleotsunami records suggest a return period more of the order of 1000 years. The discrepancy is smaller if the shallower portion of the megathrust is assumed to produce both aseismic slip, as the afterslip model suggests, and seismic slip during occasional large tsunamigenic earthquakes.

1. Introduction

The Tohoku-Oki earthquake occurred on 11 March 2011 along the Japan trench offshore Northern Honshu [*Ozawa et al.*, 2011]. Its large magnitude (M_w9.0 according to the Japan Meteorological Agency or the U.S. Geological Survey) makes it the fourth largest earthquake ever recorded. It struck within one of the best monitored area in the world. The geometry of the megathrust is quite well constrained, thanks to the presence of dense seismic networks which have been operating for decades and to numerous geophysical investigations of this area. Surface deformation was in particular recorded by the GEONET geodetic Global Positioning System (GPS) network [*Sagiya et al.*, 2000] which consists of more than 1200 stations, including 400 stations in Northern Honshu (Figure 1). Also, an unprecedented set of sea bottom geodetic measurements gives some constraints on the magnitude of the seafloor displacement near the trench [*Sato et al.*, 2011; *Ito et al.*, 2011; *Iinuma et al.*, 2012]. This earthquake occurred in an area where geodetic strain has been monitored for decades allowing for a precise characterization of interseismic deformation [*Suwa et al.*, 2006; *Hashimoto et al.*, 2009; *Loveless and Meade*, 2011]. Finally, it happened in an area with a remarkably well-documented historical seismicity [e.g., *Tsumura*, 2005]. The Tohoku-Oki earthquake therefore offers a quite unique opportunity to analyze a major megathrust earthquake with good constraints on preseismic, coseismic, and postseismic geodetic strain as well as on past seismicity. In this study, we use this information to develop a model of the seismic cycle on the Japan megathrust.

A difference between our study and previous studies of geodetic strain associated to the Tohoku-Oki earthquake is that we analyze all phases of the seismic cycle (preseismic, coseismic, and postseismic slip) jointly and in a self-consistent manner. In addition, we include the seafloor measurements acquired both before [*Matsumoto et al.*, 2008] and after the Tohoku-Oki earthquake [*Kido et al.*, 2011; *Iinuma et al.*, 2012]. Previous studies of coseismic slip have either ignored the seafloor measurements [*Ozawa et al.*, 2011; *Simons et al.*, 2011] or considered that the displacements obtained comparing the positions measured before and after the earthquake represented only the coseismic phase [*Ozawa et al.*, 2012; *Iinuma et al.*, 2012; *Wei et al.*, 2012]. This assumption is questionable as these postearthquake measurements were acquired 17 to 31 days after the main shock. The contribution of postseismic deformation to these seafloor displacements could in fact be significant. In that regard, we note that some coseismic models which were determined

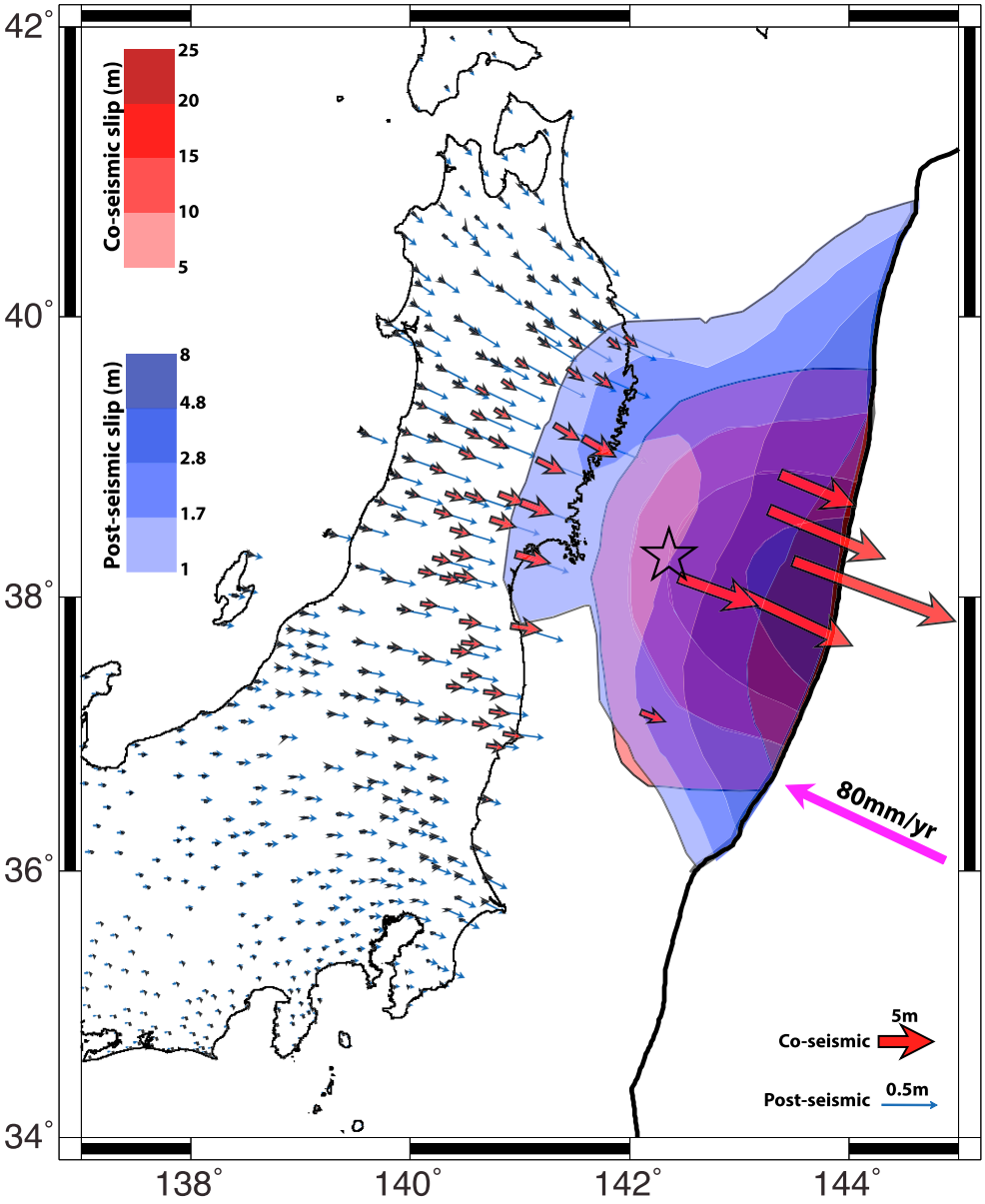

Figure 1. Coseismic (red) and postseismic (blue) slip distribution of the Tohoku-Oki earthquake of our preferred model. Note that a logarithmic scale has been used for the postseismic slip distribution for better readability. Red vectors represent the measured coseismic displacement vectors at the GEONET GPS stations, and the blue vectors represent postseismic displacements over 279 days following the Tohoku-Oki earthquake. The six near-trench stations include coseismic slip and 21 days of postseismic slip. Star shows main shocks epicenter [*Wei et al.*, 2012].

without the seafloor measurements actually predict the tsunami wave relatively accurately [*Simons et al.*, 2011], although they would predict coseismic sea-floor displacements significantly smaller than the measured displacement. On the other hand, the comparison of slip models derived by inverting either the GPS data alone or the GPS data combined with tsunami waveforms suggests that some amount of near-trench slip is needed to explain the tsunami data [*Romano et al.*, 2012]. It is possible that the tsunami would have been generated by the coseismic seafloor displacement augmented by early afterslip. Based on theoretical considerations early afterslip could be very energetic [*Perfettini and Ampuero*, 2008] and some observations support this conjecture. For instance, afterslip following the 1994 Sanriku-Haruka-Oki earthquake which struck north of the Tohoku-Oki earthquake released as much as one third of the coseismic moment in the first 24 h following the main shock [*Heki and Tamura*, 1997]. A particularly intriguing point is that, if the seafloor displacements are interpreted to be coseismic, they would imply large seismic slip (>40 m) on

the shallow portion of the megathrust beneath the accretionary prism which is commonly thought to be aseismic [e.g., *Byrne et al.*, 1988; *Scholz*, 1998]. This view is mostly consistent with the rate-strengthening frictional properties of clays which form the bulk of the sediments filling subduction trenches and are dragged down along the subduction interface and incorporated to the accretionary prism [*Hyndman et al.*, 1997; *den Hartog et al.*, 2012b].

In the following, we first present the data sets analyzed in this study and give a brief overview of the principal component analysis-based inversion method (PCAIM) which is used to determine the spatiotemporal evolution of slip on the megathrust. We next present our preferred coseismic, postseismic, and interseismic models and discuss the reliability of our results based on resolution and sensitivity tests. We finally discuss the seismic cycle in the Tohoku-Oki area.

2. The Data

To build the coseismic and postseismic slip models, we consider the daily solutions of GEONET provided by the Geospatial Information Authority of Japan (http://www.geospatialworld.net). We used the time series from 400 stations located on Honshu Island (see Figure 1) covering 279 days after the main shock. Based on the a posteriori root-mean-squares of model residuals, we found the 1σ uncertainty to be about 6 mm on horizontal positions and 29 mm on the vertical positions (see section A4). These uncertainties are larger than the standard deviation of horizontal and vertical positions which are estimated to 3 mm and 15 mm, respectively [*Nakagawa*, 2009; *Ozawa et al.*, 2012], probably because our estimates account for the uncertainties on measured positions but also for the model uncertainties. We also included measurements of seafloor displacements at six stations (GJT3, MYGI, MYGW, FUKU, KAMN, and KAMS) [*Kido et al.*, 2011; *Kato and Igarashi*, 2012; *Iinuma et al.*, 2012] (see Figure 1). The postearthquake seafloor data were acquired 17 to 31 days after the main shock, while the preseismic measurements were acquired between November 2005 and February 2011 [see *Iinuma et al.*, 2012, Table 1]. We suppose that interseismic displacements at those sites are negligible in view of the measurement uncertainties which are estimated to about 0.5 m both for the horizontal and vertical components [*Iinuma et al.*, 2012]. In total, our coseismic and postseismic inversions include measurements of horizontal and vertical displacements at 406 geodetic sites.

To build our interseismic model, we used the GPS velocities and associated uncertainties determined at the GEONET stations [*Sagiya et al.*, 2000] as reported in *Loveless and Meade* [2010]. We also added two measurements of interseismic seafloor displacements from *Matsumoto et al.* [2008] (stations MYGI and FUKU). We then perform a block correction considering the NE Honshu and Okhotsk blocks using the poles given in *Loveless and Meade* [2010] in order to refer the measurements to NE Honshu. In total, our interseismic models are based on data from 401 sites.

In order to evaluate the goodness of fit of the models presented here, we use a reduced chi-square criterion (in effect the weighted root-mean-square of the residuals) defined as

$$\chi_r^2 = \frac{1}{N \times M} \Sigma_{i=1}^{N} \Sigma_{j=1}^{M} \frac{[X^{\mathrm{obs}}(i,j) - X^{\mathrm{pred}}(i,j)]^2}{\sigma(i,j)^2}, \quad (1)$$

where N is the number of geodetic sites $\times$ the number of displacement (or velocity) components and M the number of measurements at each site. The elements $X^{\mathrm{obs}}(i,j)$, $X^{\mathrm{pred}}(i,j)$, and $\sigma(i,j)$ represent respectively the observed, predicted, and corresponding uncertainty of the displacement measured at site i at epoch j. To give more weight to the seafloor data in the inversion, we divided the uncertainties originally assigned to these measurements by a factor 2 which was chosen by trial and error so that the models would show some sensitivity to these data. The weighting is thus defined by uncertainties of 2 mm and 15 mm on the daily GPS horizontal and vertical positions and of 0.25 m on seafloor measurements. As detailed below, we tested the sensitivity of our results to this choice by also carrying separate inversions of each data set. Interseismic coupling models are determined using the uncertainties on interseismic velocities reported in *Matsumoto et al.* [2008] and *Loveless and Meade* [2010].

3. Modeling Methods and Assumptions

3.1. Megathrust Geometry

We use the U.S. Geological Survey global subduction zone model of *Hayes et al.* [2012] (http://earthquake.usgs.gov/research/data/slab/) to construct the megathrust geometry. We extracted the data points and built

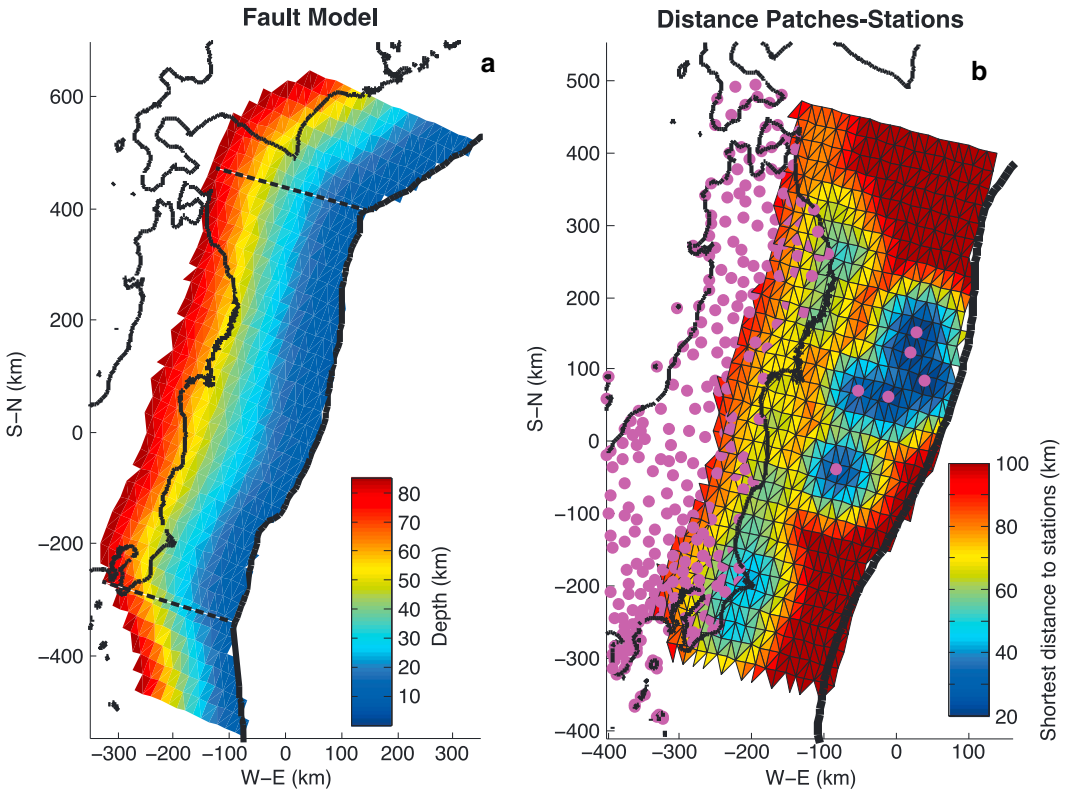

Figure 2. (a) Fault model used for interseismic deformation. The origin of the axes correspond to the earthquake's epicenter. The coseismic model is outlined by the dotted lines. Fault geometry is based on *Hayes et al.* [2012]. (b) Distance from each patch to the nearest station for coseismic and postseismic slip models.

an interface consisting of a triangular mesh using the routine make_fault_model.m of the PCAIM package (http://www.tectonics.caltech.edu/resources/pcaim/). This routine uses a Laplacian operator to smooth the fault surface. We choose the weight put on smoothing based on the L-curve [*Hansen*, 1992; *Hansen and O'Leary*, 1993]. The megathrust model used to determine interseismic coupling extends from 33 to 43°N along strike and from the trench to a depth of about 90 km (see Figure 2a). It is composed of 1296 patches with an average patch area of 262 km^2 corresponding to a mean distance between mesh nodes of about 23 km.

To determine the co- and post-seismic slip distributions, we use a megathrust model with a denser meshing but smaller extent so that the total number of patches is similar (Figure 2a). It extends approximately from 35 to 41°N along strike, and from the trench to a depth of about 90km along dip. The co-seismic fault model is composed of 1268 patches with a mean size of about 19 km, corresponding to an average patch area of 183 km^2.

3.2. The PCAIM Inversion Method

The PCAIM inversion algorithm is described in detail in *Kositsky and Avouac* [2010], *Perfettini et al.* [2010], and in the PCAIM manual (http://www.tectonics.caltech.edu/resources/pcaim/). The basic idea is that the data set is first decomposed using a principal component analysis. The data are stored in a matrix $\mathbf{X_{dat}}$, the number of rows being equal to the number of stations × the number of GPS components, while the number of columns is equal to the number of measurements epochs. In the case of the coseismic and postseismic inversion presented here, $\mathbf{X_{dat}}$ is a 1218 × 279 matrix.

The method allows handling incomplete data set as missing data points can be assigned an infinite uncertainty. The decomposition algorithm returns the matrix $\mathbf{U}$, $\mathbf{S}$, and $\mathbf{V}$, with $\mathbf{U_k}$ and $\mathbf{V_k}$ being unit vector, such that

$$\mathbf{X_{dat}} = \Sigma_{k=1}^{n_{comp}} \mathbf{U_k S_k V_k^t}, \quad (2)$$

where the upper index $(\ldots)^t$ means matrix transpose and n_{comp} is the number of components considered in the decomposition. The matrix $\mathbf{U_k}$ has the dimension $3n_{stat} \times 3n_{stat}$ and is only space dependent. The matrix $\mathbf{V_k}$ has the dimension $n_{meas} \times n_{meas}$ and is only time dependent. The matrix $\mathbf{S_k}$ is a $3n_{stat} \times n_{meas}$ diagonal matrix. The diagonal elements quantify the fraction of the data variance explained by each component.

The coseismic phase, which lasted about 200 s should appear as a discontinuous step in the time series of daily positions. Consequently, in order to isolate this component, we impose the time function associated to the first component $\mathbf{V_1}$ to be a Heaviside function (Figure A1). The number of components needed to reconstruct the original time series within uncertainties can be determined from an *F* test. Here we find that only two components are needed to reconstruct the original time series (whether the test is carried on using the original uncertainties or our a posteriori uncertainties makes no difference). The standard procedure consists in inverting all the components jointly to insure mutual orthogonality. However, an iterative scheme may be advantageous as it is computationally faster and may be more stable, although not optimal mathematically (the components are not necessarily orthogonal in that case). We also tested this approach as discussed in section C.

The second component is left free of any constraints. The vector $\mathbf{V_2}$ evolves as a logarithmic function of time (Figure A2) typical of postseismic relaxation [e.g., *Marone et al.*, 1991; *Melbourne et al.*, 2002; *Miyazaki et al.*, 2004; *Perfettini and Avouac*, 2004a; *Hsu et al.*, 2006a; *Perfettini et al.*, 2010].

The inversion step solves for the slip distribution $\mathbf{L}$ such that, within uncertainties,

$$\mathbf{X_{dat}} = \mathbf{GL}, \tag{3}$$

where $\mathbf{G}$ is the Green function operator that relates a unit slip on the fault to the corresponding displacements at the sites where surface deformation is measured. The Green functions are computed assuming point sources in a homogeneous elastic half-space [*Okada*, 1992], with a Poisson coefficient of 0.25. For a homogeneous half-space the surface displacements are independent of the shear modulus. However, we assume a shear modulus of 50 GPa to estimate moments. In reality, the shear modulus must increase with depth as demonstrated by seismic tomographic results [e.g., *Nishida et al.*, 2008], and we have considered only some mean value over the 0–60 km depth range of our model.

To regularize the inversion, we apply a Laplacian smoothing. In practice, we augment the linear system with the equation

$$\mathbf{\Delta L} = 0, \tag{4}$$

where $\mathbf{\Delta}$ is a Laplacian numerical operator described in the PCAIM manual (http://www.tectonics.caltech.edu/resources/pcaim/). The Laplacian operator is normalized by the decimal logarithm of the distance between every patch and their nearest station in order to modulate the smoothing effect according to the resolution (the weight put on smoothing is reduced where the spatial resolution of the slip inversion is best). This procedure, inspired by *Lohman* [2004], penalizes slip in areas of low resolution. The weight γ put on smoothing is determined from the L-curve [*Hansen*, 1992; *Hansen and O'Leary*, 1993]. The spatial resolution of our inversions is discussed and illustrated in Appendix. Variable boundary conditions are considered, namely, a blocked or freely slipping trench, and are accounted for in the computation of the Laplacian operator $\mathbf{L}$.

Combining equations (2) and (3) yields

$$\mathbf{L} = \Sigma_{k=1}^{n_{comp}} \left(\mathbf{G}^{-1}\mathbf{U_k}\right) \mathbf{S_k} \mathbf{V_k^t}. \tag{5}$$

No temporal smoothing is applied. The system being linear, the full (decomposition and inversion) process is extremely fast (a few minutes on a standard personal computer).

In fact, and as discussed in detail in section 3.3, equation (5) is solved considering a covariance matrix $\mathbf{C_U}$ for $\mathbf{U}$, in order to weight the inversion according to the measurement uncertainties. We have also used a simplified form for this operator, namely, $\mathbf{C_U} = \text{diag}(\text{MEAN}(\sigma^2))$, so that $\mathbf{C_U}$ becomes a diagonal matrix (section C). Doing so, $\mathbf{U}$ is weighted using the mean error in the time series at a given site. The advantage of this approach is that it is extremely fast numerically so that it facilitates carrying on a large number of inversions while still penalizing the stations that contains large measurement errors.

The determination of interseismic models is based on the inversion of a single data set of velocity measurements and therefore does not require any decomposition. Also, interseismic models are determined using the back slip approach [*Savage*, 1983], meaning that strain of the overriding plate is modeled as the result of a virtual fault sliding backward. Slip on the megathrust is obtained by adding the slip rate representing the long-term subduction of the Pacific Plate beneath Honshu to the back slip rate determined from the inversion. The back slip model applies in principle only to a perfectly planar fault but is a reasonable approximation for a fault with modest curvature [*Vergne et al.*, 2001; *Kanda and Simons*, 2010] as is the case here and for most megathrusts.

Many of the models shown in this study were obtained imposing fault slip to occur along a given azimuth. In that case the rake is imposed (but can vary on each subfault if the fault is not planar as is the case here). This azimuth is supposed to equal the direction of the plate motion of the Pacific Plate relative to Honshu. For the coseismic and postseismic model, we determine the best fitting azimuth, assumed uniform over the study area as the blocks model of *Loveless and Meade* [2010] suggests, to be 112°SE (Figure A5). The interseismic value of the back slip azimuth was chosen to 292°NW (= 112° + 180°, because of the back slip formulation) for consistency with the best fitting coseismic and postseismic slip azimuth. This value is within 6° from the best fitting value (Figure A8).

3.3. Implementation and Resolution of the Inversions

We solve for

$$\begin{pmatrix} \mathbf{C}'_{\mathbf{u}}\mathbf{U} \\ 0 \end{pmatrix} = \begin{pmatrix} \mathbf{C}'_{\mathbf{u}}\mathbf{G} \\ \gamma\mathbf{L} \end{pmatrix} \mathbf{m}, \tag{6}$$

$\mathbf{C}'_{\mathbf{u}}$ being obtained from the Cholesky decomposition so that

$$\mathbf{C}'^{\mathbf{t}}_{\mathbf{u}}\mathbf{C}'_{\mathbf{u}} = \mathbf{C}^{-1}_{\mathbf{u}}, \tag{7}$$

where $\mathbf{C}_{\mathbf{u}}$ is the covariance matrix of $\mathbf{U}$, $(...)^t$ meaning matrix transpose.

In the simplified covariance matrix presented in section C, $\mathbf{C}'_{\mathbf{u}} = \text{diag}\left(\frac{1}{\sigma_i}\right)$, where σ_i is the uncertainty associated with measurement $i = 1, N$. In the free azimuth case, the model vector $\mathbf{m}$ contains $2n_{\text{patches}}$ components or degrees of freedom, where n_{patches} is the number of triangular dislocations of the fault model. If the azimuth is imposed, the number of degrees of freedom of the model reduces to n_{patches}. Thanks to the Laplacian regularization, the equation system (6) is overdetermined (provided $\gamma \neq 0$).

The distance from each node of the megathrust to the nearest station is a convenient way of visualizing the data constraints on the slip models [*Loveless and Meade*, 2011] (Figure 2b). Figures 3a and 3b show (on a logarithmic scale) the contribution of each triangular patch to the total displacement of the network (inland and near-trench stations). Figures 3c and 3d are similar to Figures 3a and 3b considering only the inland stations. The contribution of each patch is calculated dividing the cumulated displacement (scalar sum of displacements at all the stations) induced by 1 m of slip at that patch by the maximum displacement calculated for 1 m of slip uniformly distributed over the fault model. Figure 3a is calculated for purely strike-slip motion and Figure 3b for purely dip-slip motion. Not surprisingly, the normalized contribution of each patch decays with the distance to the coast and inclusion of the near-trench stations improves significantly the resolution of the patches in their vicinity. The updip resolution near the trench is better than the one along strike, a reassuring feature since most of the motion is reverse. These tests also show for example that our coseismic and postseismic inversions are about 10 times less sensitive to slip near the trench than to slip beneath the coast where the megathrust is closest to the stations (the contribution of 10 m of slip at the trench to the geodetic signal is comparable to the contribution of 1 m of slip beneath the coast).

Figure 4a shows, for each patch, the distance to the nearest station in our interseismic fault model. This figure is similar to *Loveless and Meade* [2011, Figure 4B]. Figures 4b and 4c show the contribution (normalized by its maximum value) of each triangular patch to the total displacement of the network (inland and near-trench stations) for the interseismic phase, assuming respectively a homogeneous strike-slip and updip slip of unit 1. This figure is comparable to *Loveless and Meade* [2011, Figure 4A] but shows that the resolution of our inversion near the trench is better due to the inclusion of the two sea bottom sites of *Matsumoto et al.* [2008].

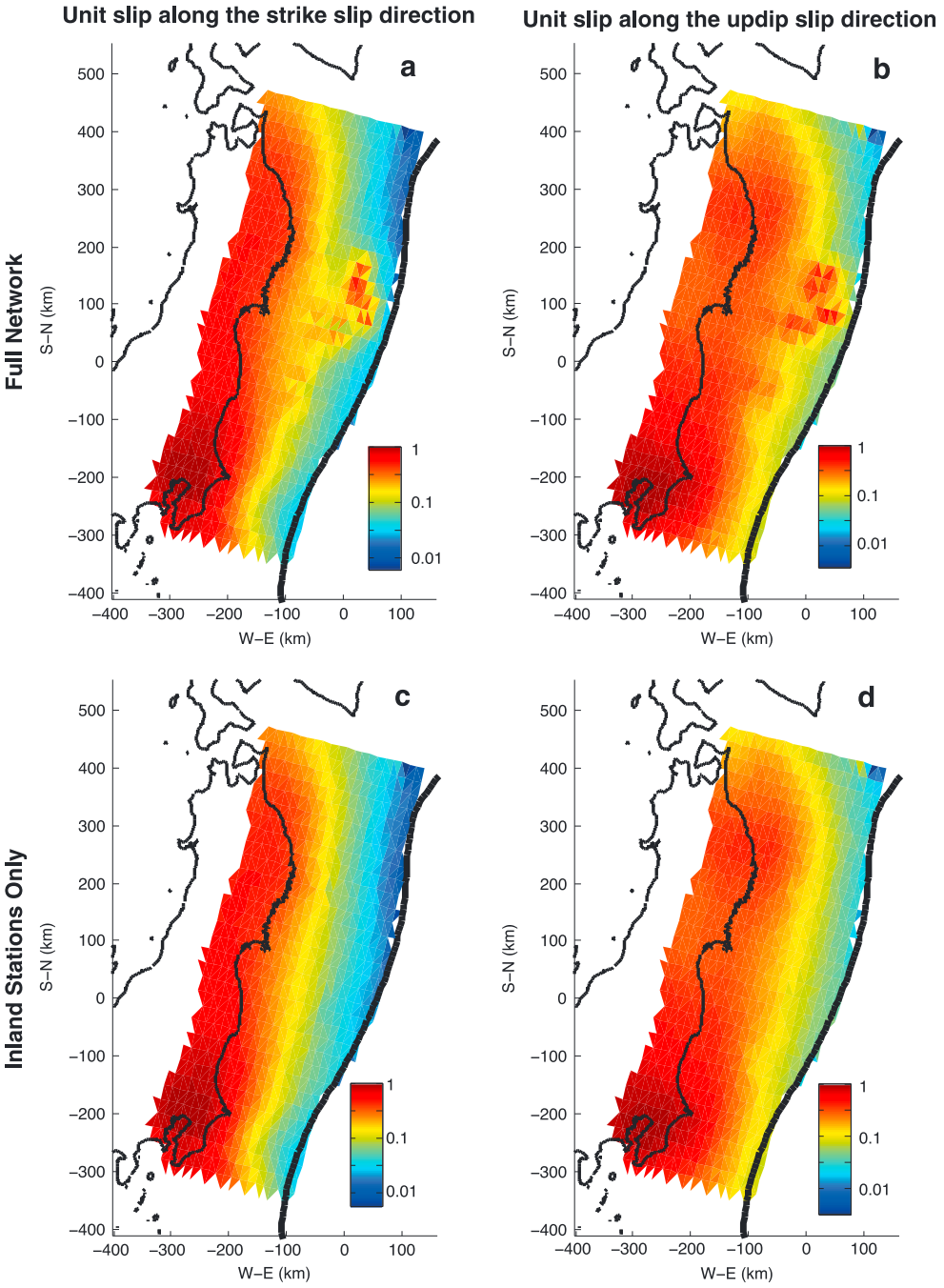

Figure 3. (a) Normalized contribution of each patch to the total displacement of the full network assuming a homogeneous strike slip of unit (inland and near-trench stations). (b) Same as Figure 3a for the updip contribution. (c) Normalized contribution of each patch to the total displacement of the full network assuming a homogeneous strike slip of unit 1 (inland stations only). (d) Same as Figure 3c for the updip contribution.

Additional resolution and sensitivity tests are presented in Appendices B1 and B2 (see Figures B1–B5). Those tests show that the inversions cannot resolve details of the slip distribution at a scale smaller than about 80 km at the trench.

4. Results

4.1. Coseismic and Postseismic Models

We have explored a wide range of coseismic and postseismic slip models and test their sensitivity to the model assumptions. We have considered models with constrained or unconstrained slip azimuth, varied

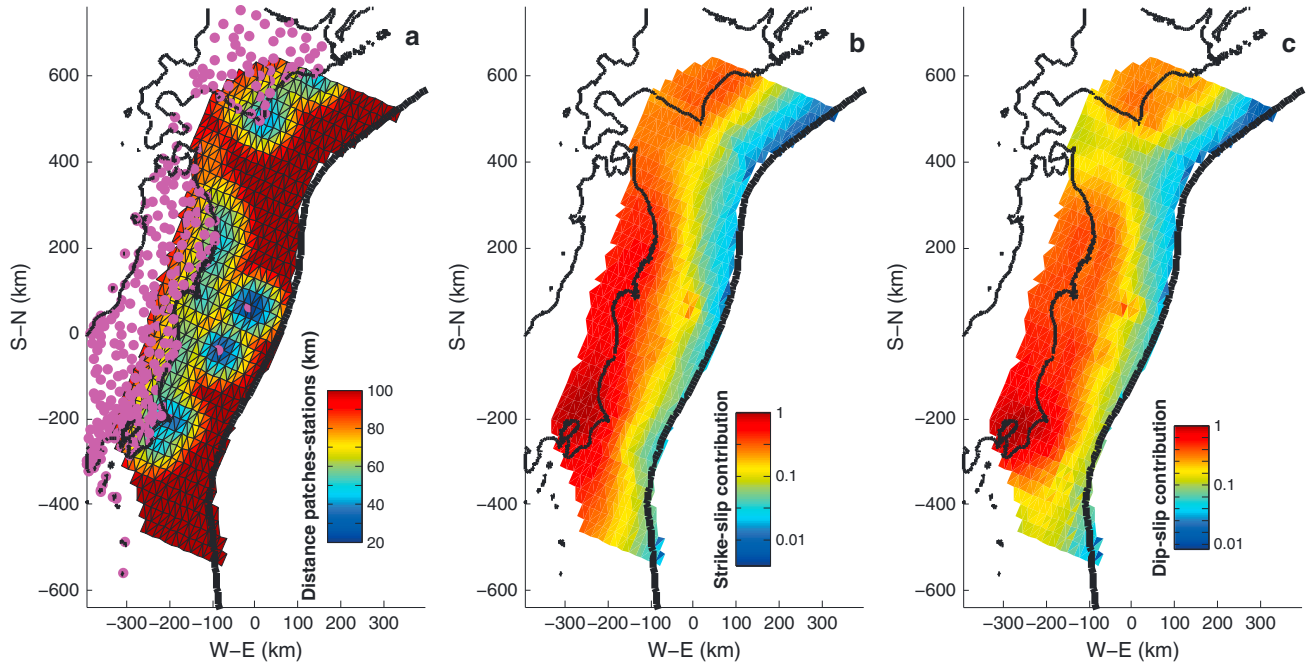

Figure 4. (a) Distance (in km) to the nearest station for the interseismic coupling with creeping trench. (b) Normalized contribution of each patch to the total displacement of the full network assuming a homogeneous strike slip of unit 1 (inland and near-trench stations). (c) Same as Figure 4b for the updip contribution.

the boundary condition at the trench with either free slip (FT for free trench) or no slip at the trench (BT for blocked trench) and varied the weight put on smoothing. A selection of these models are presented in section A2.1. The coseismic and postseismic slip distributions are inverted jointly so that the consistency of the coseismic and postseismic models is warranted.

Figure A4 shows that a smoothing parameter of the order of $\gamma = 5 \times 10^5$ yields a good compromise between the goodness of fit and model roughness for both the coseismic and postseismic inversions. The coseismic and postseismic slip distributions (Figure 5) obtained considering a variable slip azimuth show only small variations of slip azimuth. For the same value of the smoothing parameter, the variance of the weighted residuals (equivalently the chi-square) is reduced by about 15% if the azimuth of slip is left free, while the number of free parameters increases by a factor of 2 (from 2536 to 1268). The free azimuth model is probably a more accurate representation of coseismic and postseismic slip during the Tohoku-Oki earthquake, but the model with fixed slip azimuth is more appropriate to build a model of the seismic cycle. Indeed, the rake at one point of the megathrust might vary from one earthquake to the other, while the rake averaged over repeated ruptures must be consistent with the azimuth of slip required by the plates convergence. We determine the optimal slip azimuth ϕ which minimizes the reduced chi-square (Figure A5). For all boundary conditions (free or blocked trench), the optimum value is of the order of $\phi \approx 112°$.

Figure 6a shows our preferred coseismic model considering the optimal values of the smoothing parameter and slip azimuth (namely, $\gamma = 5 \times 10^5$ and $\phi = 112°$) and assuming free slip at the trench. Observed and predicted coseismic displacements and residuals are plotted in Figures 6b, 7a, and 7b. Figure 8a shows the corresponding postseismic model (also determined with $\gamma = 5 \times 10^5$ and $\phi = 112°$) and assuming free slip at the trench. The fit between the observed and predicted time series of positions at some sites is shown in Figure 9. Observed and predicted cumulative postseismic displacements and residuals are plotted in Figures 8b, 10a, and 10b.

The coseismic model yields a peak slip of about 30 m and a released moment of 4.44×10^{22} N m, equivalent to a moment magnitude of $M_w = 9.03$. The postseismic model indicates a peak slip of about 9 m and a cumulative moment of 1.58×10^{22} N m released during the first 279 days. This joint solution for coseismic and postseismic slip implies that afterslip released a moment equivalent to about 36% of the coseismic moment over the 279 days following the main shock. The sum of the scalar moments of all aftershocks within the area covered by our afterslip model add to a moment of 1.28×10^{21} N m over this time period

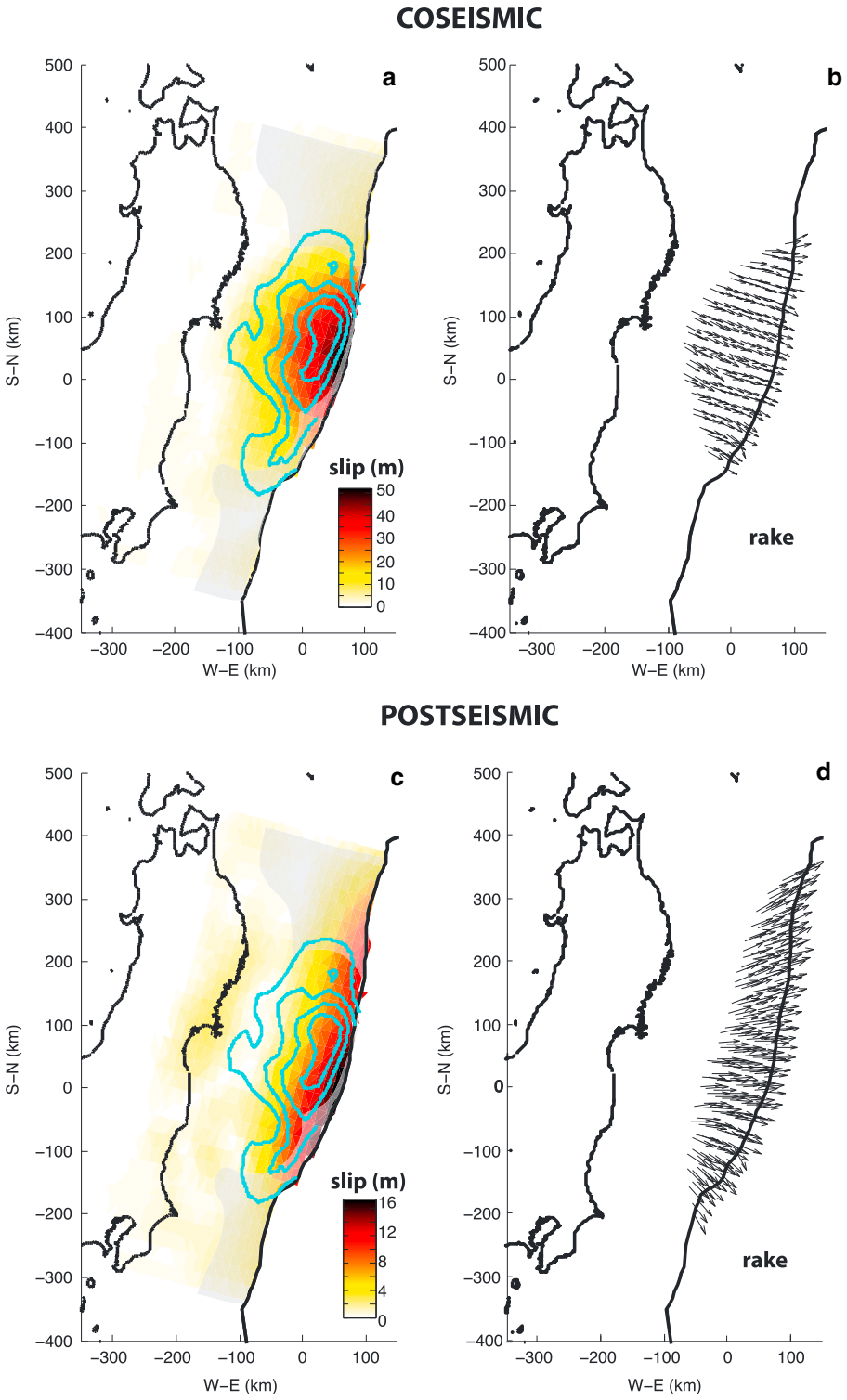

Figure 5. Best (a) coseismic and (c) postseismic slip models for the free azimuth case for a smoothing parameter of $\gamma = 10^5$. A free trench boundary condition has been imposed. The green vectors show the slip azimuth (hanging wall relative to footwall). The cyan contours correspond to the coseismic contours of *Wei et al.* [2012] (10, 20, 30, and 40 m), and the blue contours are the slip contours of the coseismic model of the left panel. (b and d) The azimuth vectors for the coseismic and postseismic models of Figures 5a and 5c. The gray transparent area represents the area of low resolution of Figure 3.

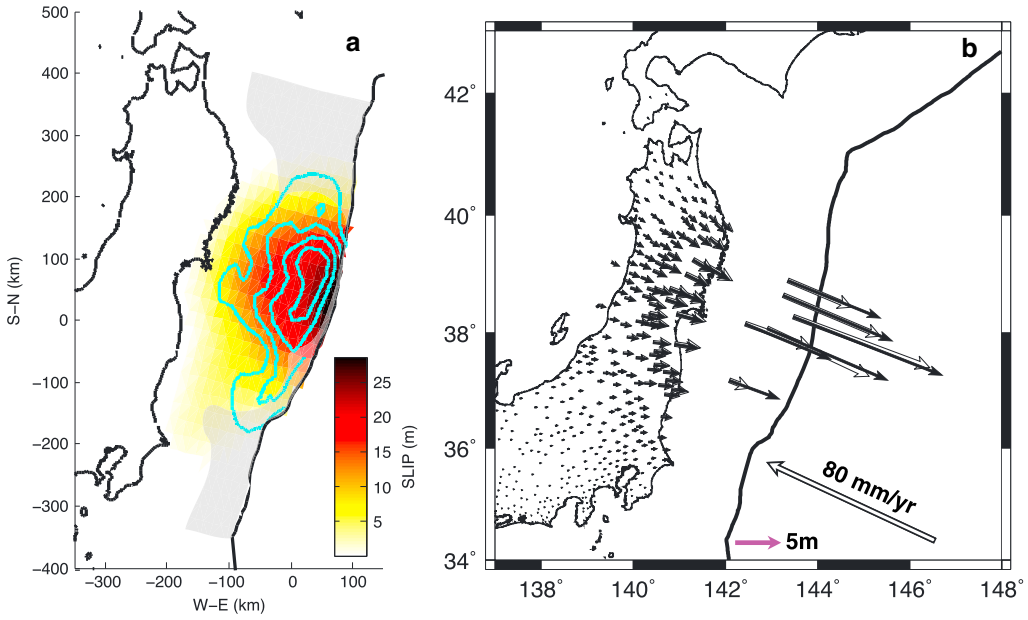

Figure 6. (a) Preferred coseismic slip distribution model. This model was obtained with slip left free at the trench, a slip azimuth constrained to $\phi = 112°$, and a smoothing parameter $\gamma = 5 \times 10^5$. This model was determined jointly with the postseismic model of Figure 8a. Blue lines show slip contours of the coseismic model of *Wei et al.* [2012] (10, 20, 30, and 40 m), derived from the joint inversion of the high-rate GPS times series of the GEONET stations, accelerometric waveforms and seafloor displacements. The gray transparent area represents the area of low resolution of Figure 3. (b) Corresponding coseismic displacement field (black arrows). The data are shown as open arrows. The white arrow labeled "80 mm/yr" is oriented according to the slip azimuth of our best interseismic model ($\phi = 292°$).

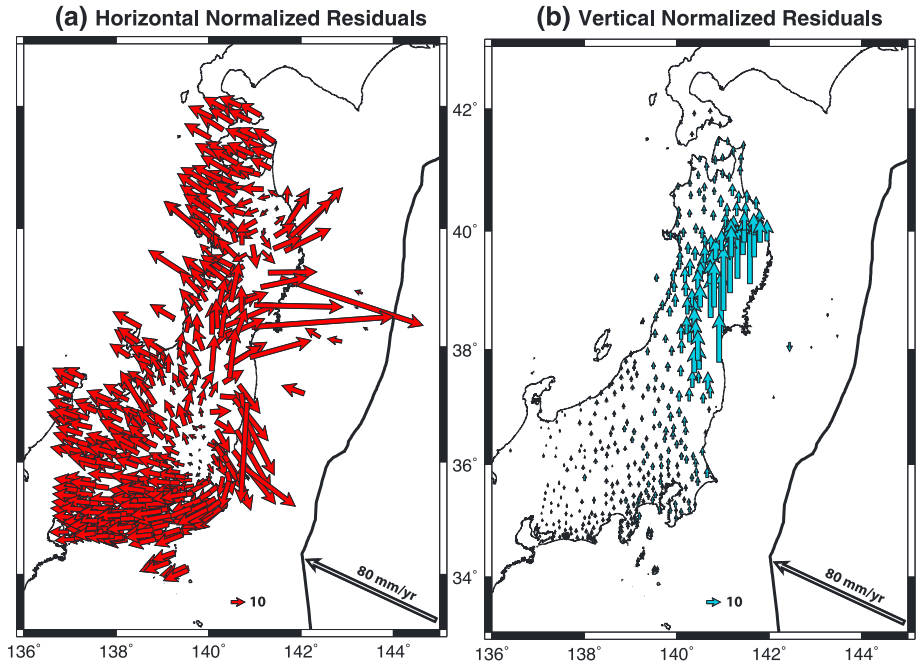

Figure 7. (a) Horizontal and (b) vertical residual displacement normalized by the rescaled uncertainties for the coseismic model of Figure 6.

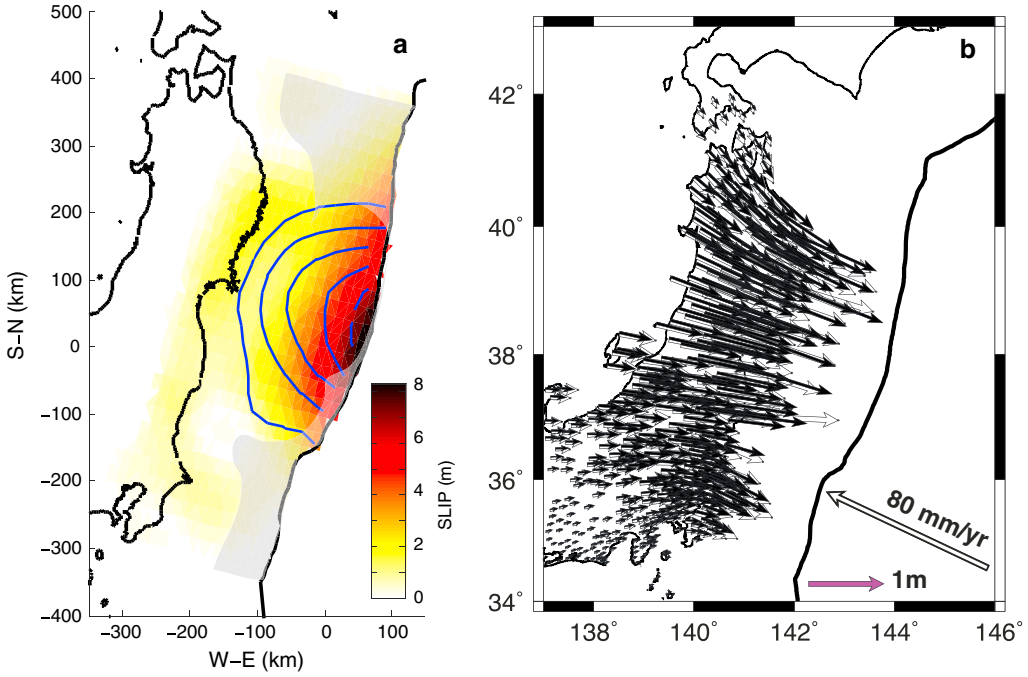

Figure 8. (a) Preferred model of cumulated postseismic slip over 279 days following the main shock. This model was obtained with slip left free at the trench, a slip azimuth constrained to $\phi = 112°$, and a smoothing parameter $\gamma = 5\times10^5$. This model was determined jointly with the coseismic model of Figure 6a. The blue contour corresponds to our preferred coseismic model of Figure 6a, each line corresponding to 5 m of slip increment. The gray transparent area represents the area of low resolution of Figure 3. (b) Corresponding postseismic displacement map.

(using the National Earthquake Information Center catalog with $M_w > 5$), representing about 8% of the moment released by our preferred postseismic model of Figure 8a. As many of these aftershocks might not have happened on the plate interface, and since the summation of the scalar moment is overestimating their cumulative contribution, we infer that more than 92% of the afterslip measured from geodesy has been aseismic.

Our model systematically underestimates the vertical displacements. Such a feature is probably due to an improper fault geometry below the continent or an inadequate assumption of homogeneous elastic properties.

4.2. Interseismic Deformation Model

For the interseismic model, we consider again two distinct boundary conditions: (i) a locked trench (label LT) and (ii) a freely creeping trench (label CT).

Figure A6 shows the reduced chi-square as a function of the smoothing parameter considering variable and fixed slip azimuth and varied boundary conditions (freely creeping or locked trench). A value of the smoothing parameter of the order of $\gamma = 10$ offers a reasonable compromise between the goodness of fit and model roughness for most cases. Figures A7a and A7b show that variations of slip azimuth are modest so that, as in the coseismic and postseismic case, imposing a uniform slip azimuth seems appropriate to first order.

Figure A8 shows the misfit between the data and the model as a function of the slip azimuth. A value of the order of $\phi \approx 298°$ appears as optimal and is nearly parallel to the coseismic and postseismic optimal azimuth ($\phi \approx 112°$). Under the back slip assumption, perfect collinearity is obtained for $\phi \approx 118°$ ($= 298–180°$). Hereafter, we assume a constant slip azimuth $\phi = 112°$ to warrant consistency between the coseismic, postseismic, and interseismic models.

Figure 11a shows our preferred interseismic model considering the optimal values of the smoothing parameter and slip azimuth ($\phi = 112°$) assuming a locked trench. Comparison between observed and predicted velocities and model residuals are plotted in Figures 12a and 12b. Figures 11b, 13a, and 13b show the same

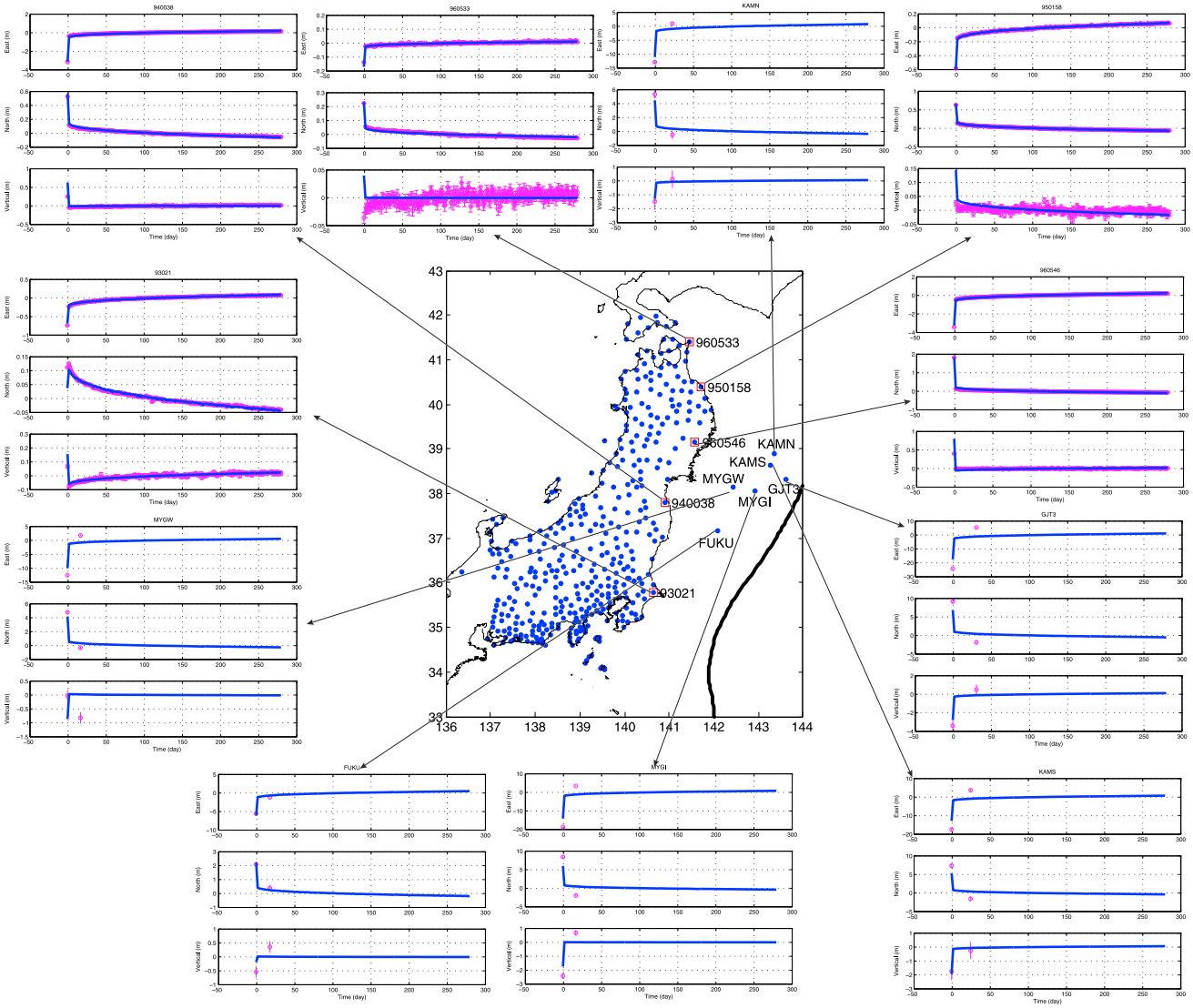

Figure 9. Time series at selected stations for our preferred model of Figures 6a and 8a. The model (blue line) is in close agreement with the data (pink dots).

for the model obtained assuming free creeping at the trench. For both boundary conditions, our models are close to the models of *Loveless and Meade* [2010], a nonsurprising result as we have used the same data set, except for the two additional seafloor measurements that we included. A noticeable feature of Figures 11a and 11b is that the rupture area of the Tohoku-Oki earthquake was mostly locked in the interseismic period.

The strongly coupled patches at the northern and southern edges of the model are less meaningful. This is due to two main features: (i) edge effects near the boundaries of our fault model and (ii) a more complex regional tectonic model should be considered to take into account the subduction of the Philippine Sea Plate along the Sagami and Nankai troughs on the southern side and the Okhotsk Plate on the northern side of our model [*Loveless and Meade*, 2010]. Also, additional GPS stations especially on the Hokkaido Island would need to be included to resolve the coupling pattern at the northern edge.

The residuals near the coast, assuming either a locking (Figures 12a and 12b) or free creeping at trench (Figures 13a and 13b), are small and look mostly randomly distributed. Residual velocities tend to point westward at eastern stations and eastward at western stations. Those residuals probably reflect the influence of secondary tectonic structures within Honshu but are small enough that the interseismic coupling models are probably not biased. The residuals on the southern and northern part of the model are large due to the Okhotsk and Philippine Sea Plates not being taken into account in our model.

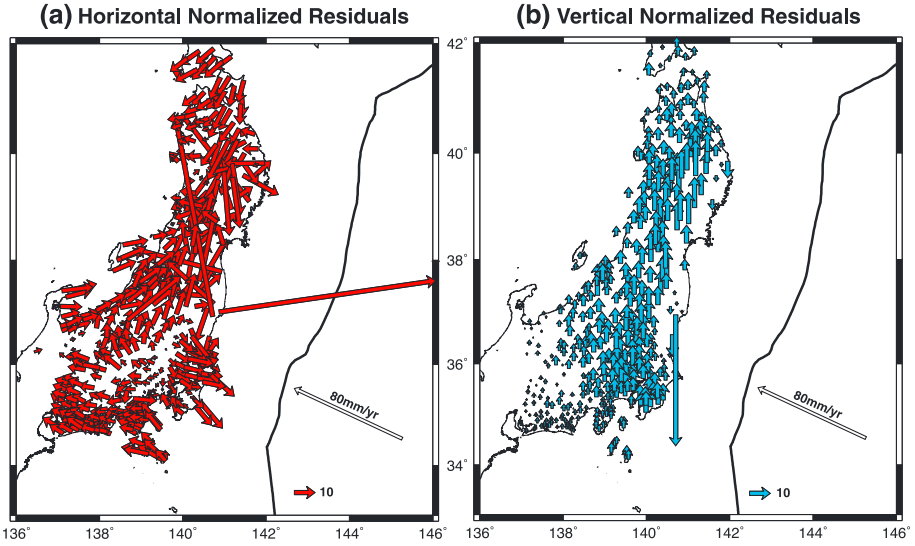

Figure 10. Normalized residual displacement map for the postseismic model of Figure 8b.

5. Sensitivity Tests and Robustness of Modeling Results

5.1. Influence of the Decomposition

The decomposition procedure, with $\mathbf{V}_1$ imposed to be a step function, was designed to separate coseismic and postseismic displacements. However, the shallow patch of afterslip could be taken as suggesting that the fraction of sea bottom displacements interpreted as postseismic could be erroneous. Here we show that

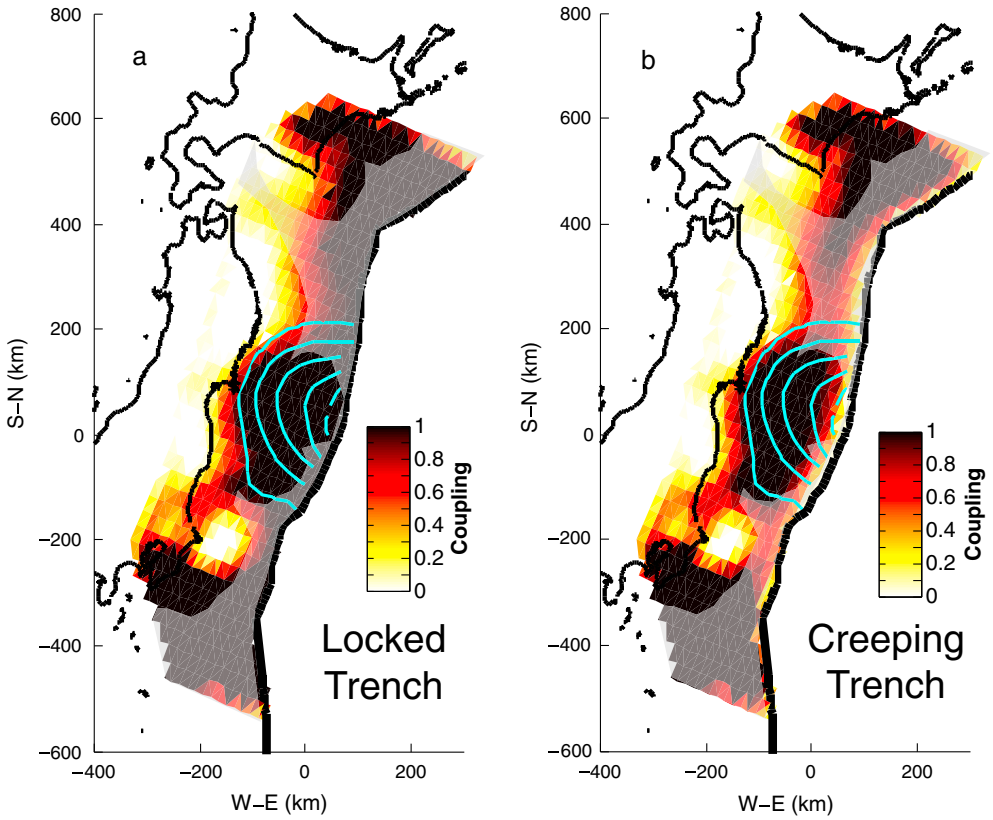

Figure 11. Best interseismic coupling model derived with a fixed slip azimuth (slip azimuth $\phi = 292°$) assuming (a) locking at the trench or (b) a creeping trench. The smoothing parameter is $\gamma = 10$. The cyan contours correspond to the coseismic model of Figure 6a. The gray transparent area represents the area of low resolution of Figure 4.

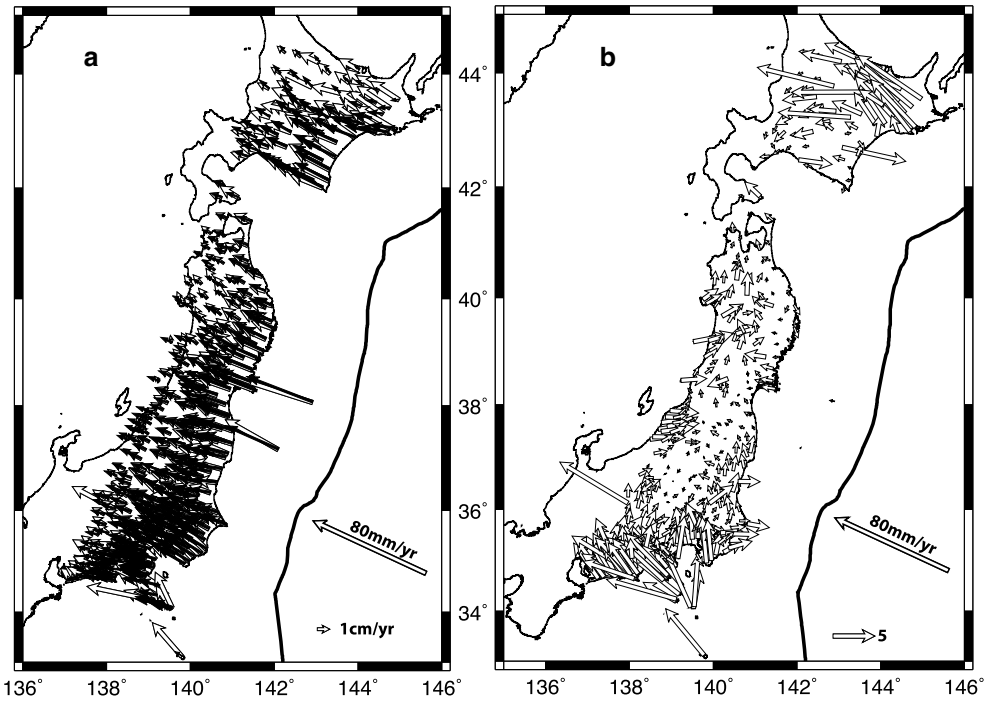

Figure 12. (a) Interseismic velocity map for our best fit model ($\gamma = 10$, $\phi = 292°$) with locked trench. The white arrow labeled "80 mm/yr" is oriented according to the slip azimuth of our best interseismic model ($\phi = 292°$). (b) Residual velocity map normalized by the uncertainties. The white horizontal arrow corresponds to a normalized velocity of 5.

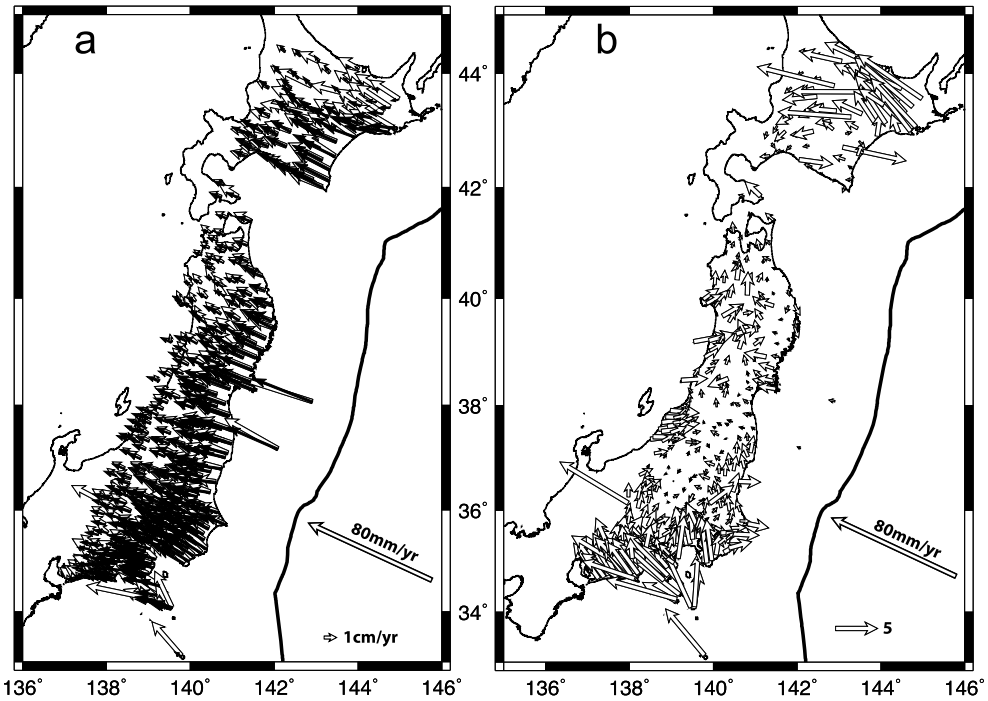

Figure 13. (a) Interseismic velocity map for our best fit model ($\gamma = 10$, $\phi = 292°$) with creeping trench. The white arrow labeled "80 mm/yr" is oriented according to the slip azimuth of our best interseismic model ($\phi = 292°$). (b) Residual velocity map normalized by the uncertainties. The white horizontal arrow corresponds to a normalized velocity of 5.

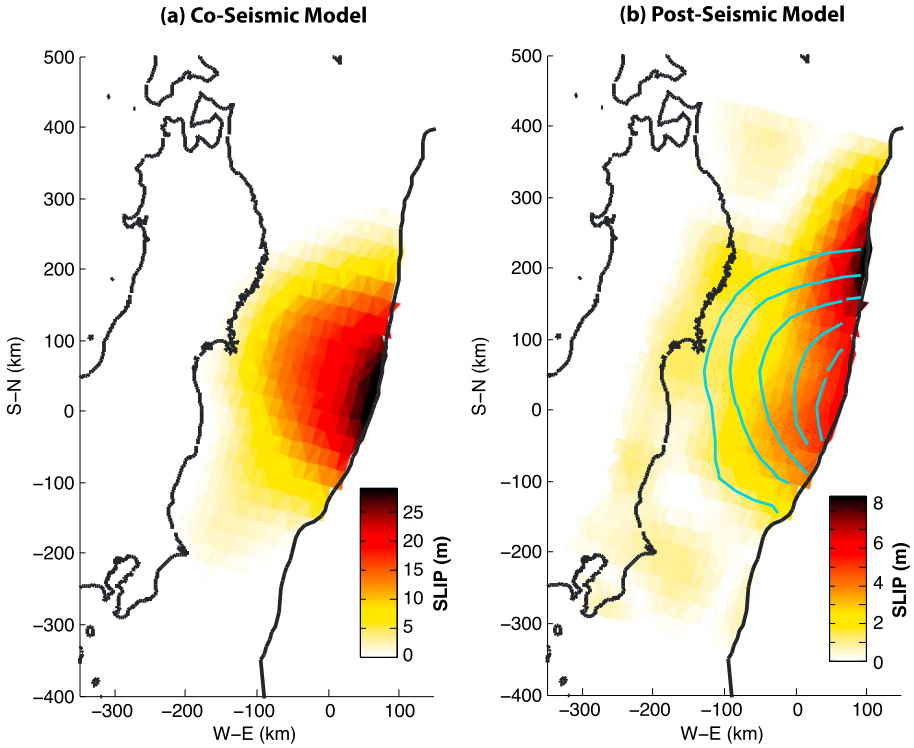

Figure 14. (a) Reference coseismic model considering the iterative decomposition with simple $\mathbf{U}$ covariance and free trench ($\gamma = 10^4$, $\phi = 112°$) . (b) Same for the postseismic case. The cyan contour corresponds to the coseismic model in Figure 14a with 5 m slip increments.

this feature is not due to coseismic slip leaking into the postseismic slip distribution. To address this issue, we have determined postseismic slip considering only the postseismic time series, i.e., from day 1 to 279 meaning that the sea bottom measurements had to be excluded. In this case, the PCAIM decomposition is carried on considering only one free component. Figure A12 shows the obtained postseismic slip distribution. This model is very close to our preferred model of Figure 8a obtained simultaneously with the coseismic slip distribution. The similarity of the two solutions demonstrates that the decomposition operates consistently when considering the postseismic data alone or together with the coseismic data. We obtained similar conclusions when considering the coseismic data alone, i.e., when performing a static inversion of the coseismic displacements.

Our two component model implies that during the postseismic phase, the temporal evolution of slip is the same all over the fault: the spatial distribution of postseismic is stationary with the slip amplitude increasing with time as $\mathbf{V_2}$. We have performed static inversions (not shown here) between two variable epochs and found that the spatial pattern is roughly stationary (only the slip amplitude is different depending on the two epochs chosen), a result consistent with our finding that only two components are sufficient to explain most of the data variance.

The sensitivity of the modeling results to the decomposition technique is interesting, too. Figure 14 shows the result obtained using the iterative decomposition with the simple covariance matrix of $\mathbf{U}$ (see section C for more details). The overall fit to the data is comparable to our preferred model, although somewhat better due to slightly lower smoothing constrains. The coseismic rupture is not changed much. The main difference is that the shallow afterslip zone is split into two patches respectively to the north and south of the coseismic rupture because of the poor along-strike spatial resolution at the trench.

In all models obtained in this study, some significant overlap exists between the coseismic and postseismic slip distributions. As discussed in section 5.3, this overlap is not due to a particular data set. The resolution tests presented in section B1. (Figures B1 and B2) demonstrate that this overlap is not only due to the limited spatial resolution of our inversions. To confirm this point, we have performed some resolution tests creating a synthetic set of data that mimics our preferred models (see section B2 for details). Figure B3 clearly shows

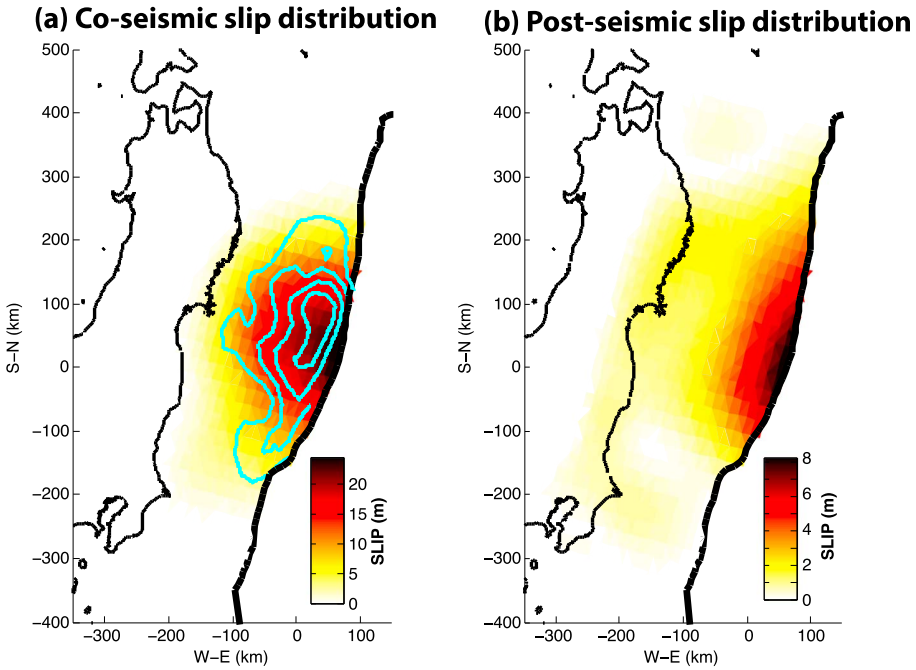

Figure 15. (a) Coseismic and (b) postseismic distribution considering only the inland stations, with an imposed slip azimuth $\phi = 112°$ and a smoothing parameter $\gamma = 3 \times 10^5$. The cyan contour corresponds to the coseismic model of *Wei et al.* [2012] for comparison (10, 20, 30, and 40 m contours).

that our inversion scheme has the ability to resolve this overlap which seems required by the data. This is true when considering the inland data only as shown in Figure B5.

5.2. Robust Features of Our Inversions

Comparison of the various models determined in this study (see the various sensitivity and resolution tests presented in the appendices) allows identifying the robust features of the inversions. All the models show a relatively compact zone of coseismic slip. The largest amount of afterslip occurs near the trench. A deeper zone of afterslip also exists but shows much smaller slip amount than the shallow afterslip region. This deeper region of afterslip outlines the coseismic rupture with a small degree of overlap, especially in the case of rough slip models (Figures A9 and A10). By contrast, the shallower slip zone always largely overlaps with the coseismic rupture. However, the details of the slip distributions and the value of peak slip and moment vary considerably.

The coseismic or postseismic peak slip values vary in particular quite significantly depending on the weight put on smoothing, the boundary condition at the trench, and the constraints put on slip azimuth: for instance, the model obtained with no constraint on slip azimuth and free slip at the trench (Figures 5a and 5b) predicts larger coseismic slip than our preferred model with imposed slip azimuth. The peak slip in the coseismic model exceeds 50 m and the coseismic moment increases to 6.9×10^{22}N m assuming a shear modulus of 50 GPa, yielding a moment magnitude M_w9.16. If we choose the coseismic slip distribution of *Wei et al.* [2012] as a reference model, a value of 38 GPa has to be considered instead of our 50 GPa so that the moment calculated with a constant shear modulus yields the same moment as the one calculated for a depth-varying model. For 38 GPa, the moment of the coseismic model with variable azimuth drops to 5.2×10^{22}N m, a value quite close to the seismological estimate (5.31×10^{22} N m according to the Global Centroid Moment Catalog (GCMT) solution). The postseismic slip distribution is also affected (compare Figures 8a and 5b) yielding a postseismic peak slip of about 17 m, and the postseismic moment increases to 2.7×10^{22} for a rigidity of 50 GPa and 2.1×10^{22} for a rigidity of 38 GPa. The ratio of postseismic to coseismic moment released is about 39% and remains comparable to the 36% found for the models of Figures 6a and 8a.

The amount of slip greatly depends on the smoothing parameter (Figures A9 and A10). Rougher models ($10^4 \leq \gamma < 10^5$) tend to promote larger slip, a low coseismic moment ($M_w^{cos} \approx$ 8.9–9.0), a larger postseismic moment ($M_w^{post} \approx$ 8.9–9.1) and a smaller but still significant overlap. Smoother models ($10^5 < \gamma \leq 10^6$) tend

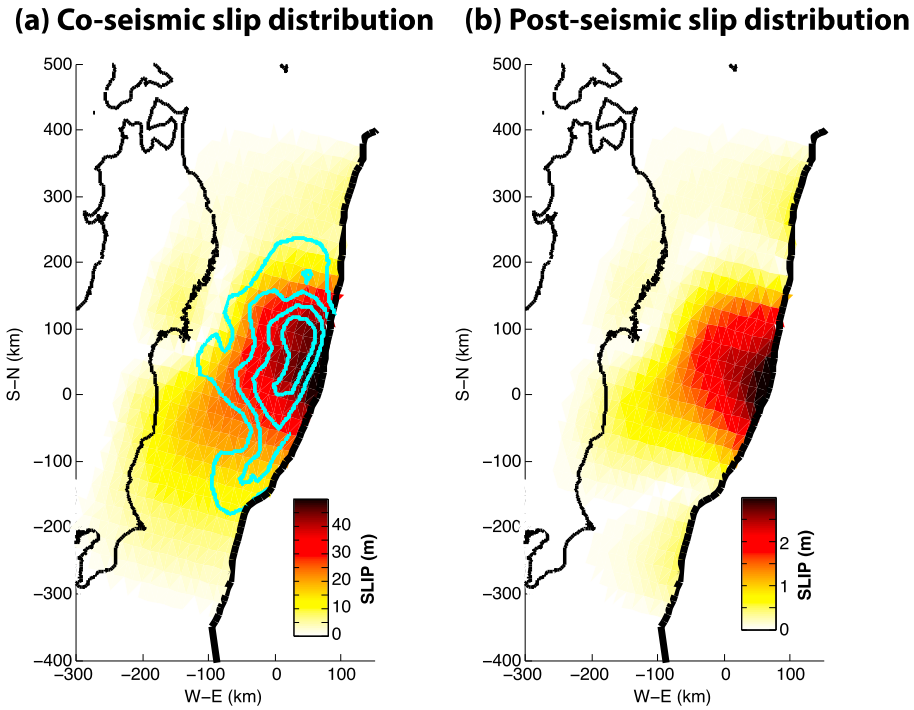

Figure 16. (a) Coseismic and (b) postseismic distribution considering only the near-trench stations, an imposed slip azimuth ($\phi = 112°$), and a smoothing parameter of $\gamma = 10$. The cyan contour corresponds to the coseismic model of *Wei et al.* [2012] for comparison.

to promote lower slip, a nearly constant coseismic ($M_w^{cos} \approx 9.0$) and postseismic moment ($M_w^{post} \approx 8.7$), and a larger degree of overlap between the coseismic and postseismic distributions.

The fact that rougher models imply larger slip amplitudes is not surprising as the slip potency is a robust quantity of the inversion: a rougher model tends to concentrate slip on smaller regions implying a larger slip amplitude to maintain a constant slip potency.

5.3. Respective Influence of the GPS and Seafloor Measurements

Here we assess the respective influence of the offshore and inland data on our results. A simple way to address this issue is to consider those data sets separately.

Figure 15 show the coseismic and postseismic distribution considering only the inland stations. Not surprisingly, the model closely resembles our preferred model since the single near trench measurements weight much less in the data matrix that the 400 continuous GPS stations operating during 279 days, making the PCAIM decomposition (and hence the inversion results) nearly identical. The only difference is that the smoothing parameter had to be adjusted to 3×10^5 to obtain a model comparable to our preferred model of Figure 8a.

Figure 16 shows the coseismic and postseismic distribution considering the near-trench measurements only. In this case, the data matrix is extremely sparse with only two measurements at each of the six sites. In that inversion, the number of stations is drastically reduced (from 400 to 6), so that the smoothing parameter had to be reduced by a factor 10^4. The first measurement corresponds to the origin of time (the time of the main shock) and null displacements. The time of the second measurement varies between stations and can take the values 17 (for stations MYGI and MYGW), 18 (for station FUKU), 23 (for station KAMN), 25 (for station KAMS), or 31 days (for station GJT3). Those various measurement times can be used to build a time series for the seafloor stations. The PCAIM decomposition is then performed on this time series with the same procedure as in the joint inversion presented above. The first component, forced to be associated to a step function, represents the coseismic slip incremented with any postseismic slip that would have happened until the date of the first measurement (17 days after the main shock). This model predicts a large-slip amplitude near the trench, up to nearly 50 m with a moment magnitude of nearly $M_w \approx 9.3$ for a rigidity of 50 GPa, and about $M_w \approx 9.2$ for a rigidity of 38 GPa. The postseismic slip (between days 17 and 31) is

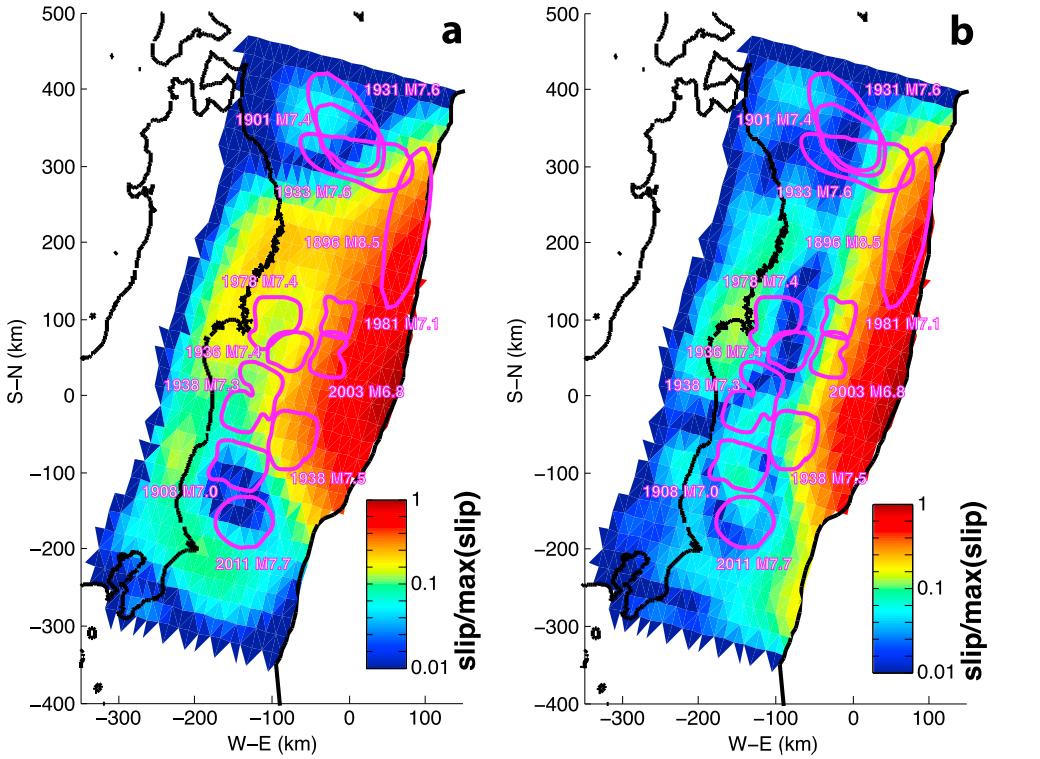

Figure 17. (a) Afterslip model of Figure 8a plotted with a logarithmic color scale. The pink contours correspond to the rupture area of historical events compiled by *Johnson et al.* [2012]. (b) Same as Figure 17a for the variable azimuth model of Figure 5.

small with about 3m of peak slip, and the corresponding moment magnitude is of the order of $M_w \approx 8.4$. It is remarkable that this sparse set of seafloor data alone turns out sufficient to derive a reasonable model, though far less well constrained than the models derived with the GPS data. This model also predicts postseismic slip near the trench and the amount of afterslip is roughly consistent with the prediction of the joint model for the period covered by the seafloor data (between days 17 and 31).

Inclusion of the inland stations introduce a distinctive strip of postseismic slip below the coastline, a feature not observed so clearly when considering the model based on the near-trench measurements only. It should be emphasized that, due to its proximity to the coastline, this strip of deep afterslip contributes to the postseismic displacement measured inland significantly more than the shallow patch of afterslip. This is visible on Figure 3d that shows the contribution of each patch to the total postseismic displacement of the inland stations. In that regard, the representation of the postseismic slip distribution with a logarithmic scale as shown in Figure 17 gives a better rendering of the postseismic slip distribution that attenuates the apparent outweight of the shallow slip in Figure 8a, despite its significant contribution to explain the measured inland geodetic signal. The results obtained from these separate inversions show that there is no inconsistency between the inland and offshore data, but that the temporal sampling of the seafloor data is obviously inappropriate to solve for coseismic and postseismic displacements. Noteworthily, both of these inversions call for some significant shallow afterslip.

5.4. Sensitivity to the Green Functions

In this study, we have assumed a homogeneous elastic half-space. Variations of the elastic structure could formally be included in the green functions (GF) through, for example, computation of the GF with a Finite Element Model [e.g., *Moreno et al.*, 2009]. First of all, it is important to note, as pointed out by *Wald and Graves* [2001], that the use of inadequate GF to model surface displacements is more forgiving for static data than for seismic data owing to the relative insensitivity of geodetic data to short-wavelength structures. The most likely bias introduced by our assumption of homogenous elastic properties is that we probably underestimate slip at shallow depth as, in a model with variable elastic properties, the presumably lower shear modulus near the trench would attenuate the inland geodetic signal. Our coseismic models are nevertheless

quite similar to the various coseismic models which were determined considering a more realistic Earth structure and a combination of strong motion and GPS data. In particular the finite-source kinematic model of *Wei et al.* [2012] is very close to the model we obtained allowing for a variable slip azimuth as illustrated by Figure 5.

Similar conclusions have been reached considering other subduction earthquakes such as the Maule [*Lin et al.*, 2013], the great Valdivia [*Moreno et al.*, 2009], and the Nias earthquakes [*Hsu et al.*, 2011]. Although some differences exist regarding the details of the coseismic distribution, they are not significant, and the overall slip pattern, amplitude, and seismic moment do not seem to depend much on the assumed elastic structure. Furthermore, the relative position of the coseismic and postseismic slip distribution should not be affected by the details of the elastic model. It is in particular difficult to imagine that variations of the elastic structure alone could explain the existence of afterslip near the trench if not required by the data.

6. Discussion

6.1. Comparison With Published Coseismic Models

The moment of our coseismic models always fall in the range between 2.8 and 6.7×10^{22} N m corresponding to moment magnitudes between M_w8.9 and M_w9.15 (calculated assuming a shear modulus of 50 MPa). Our preferred model (Figure 6a) has a moment of 4.44×10^{22} N m (M_w9.03). This range of values is in good agreement with the seismological moment estimated to 5.31×10^{22} N m from point-source modeling of long-period surface waves (http://www.globalcmt.org/CMTsearch.html) which corresponds to a moment magnitude of M_w9.0. Comparison with other coseismic models derived from inversion of geodetic data shows that our preferred coseismic model (Figure 6a) has a slip potency comparable to the models derived without taking into account the seafloor measurements [*Simons et al.*, 2011; *Ozawa et al.*, 2011] and somewhat lower than the models including those seafloor measurements [*Ozawa et al.*, 2012; *Iinuma et al.*, 2012]. The joint inversion of the inland GPS data and the tsunami waveforms [*Romano et al.*, 2012] yields a model that seems closer to the coseismic model derived with inclusion of the seafloor data [e.g., *Wei et al.*, 2012]. Actually, our model obtained with no constraints on slip azimuth (Figure 5a) does produce more slip near the trench in closer agreement with those models. The moment calculated for this model exceeds the seismological moment by 30% and is probably overestimated due to the assumption of uniform shear modulus of 50 GPa. As discussed in section 5.2, when using the value of 38 GPa inferred from *Wei et al.* [2012], the estimated moment for the variable azimuth coseismic model is close to the seismological estimate.

When the various coseismic slip distribution models are compared, significant variations are observed regarding the location and extent of the rupture area and peak slip value. The position of peak slip along the coast is generally consistent between the various published models. The value of peak slip varies from 30 m [*Evans and Meade*, 2012] up to 90 m [*Iinuma et al.*, 2012], but most studies predict a peak slip in the range of 40 to 65 m [*Miyazaki et al.*, 2011; *Ozawa et al.*, 2012; *Simons et al.*, 2011; *Wei et al.*, 2012]. Our model with variable slip azimuth (Figure 5a) predicts a maximum value of the order of 50 m. It is clear that the peak slip value strongly depends on whether the slip azimuth is allowed to vary or not. The peak slip value also depends strongly on the weight put on the regularizing criterion. When only inland data are considered, peak slip tends to be much smaller, around 25 m in the model of Figure 15. It is much larger, around 50 m, in the model of *Simons et al.* [2011]. But clearly, their preferred model is rougher than ours and should be rather compared to the model of Figure A9 in the case $\gamma = 10^4$ and for which peak slip reaches nearly 40 m. Peak slip, unlike slip potency, is not a reliable parameter of the inversion.

All geodetic studies yield coseismic slip models with similar slip potency as this quantity is relatively well constrained from the GEONET data. The assumed elastic structure is probably the main factor of variability among the various models. Models that take into account depth variations of elastic moduli do however tend to produce comparatively more slip at the trench as the inland geodetic signal induced by shallow slip is attenuated. This point is supported by the observation that the amplitude of slip varies depending on the relative weight assigned respectively to the inland stations and the near-trench measurements. When the near-trench stations are considered solely, our model predicts a peak slip of nearly 50 m (see Figure 16), consistent with the 40–65 m range mentioned above. It should be recalled that this slip would then include any postseismic slip which would have occurred up to day 17 after the main shock. The seafloor measurements tend to push the location of peak slip toward the trench as may be seen comparing our preferred model with the model of Figure 16. Peak slip is located near the trench in all data set incorporating the near-trench

stations [*Ozawa et al.*, 2012; *Iinuma et al.*, 2012; *Wei et al.*, 2012]. When free to reach the trench (our free trench BC), peak slip is as shallow as allowed by the fault model [*Iinuma et al.*, 2012; *Wei et al.*, 2012], but it is deeper when slip is forced to taper off at the the trench [*Ozawa et al.*, 2012] as seen also from our "blocked trench" inversions.

Compared to published coseismic models, our preferred model seems to slightly underestimate the amount of shallow slip, essentially because a large fraction of the seafloor displacements is interpreted as post-seismic, and to a lesser degree because the assumption of homogeneous elastic properties tend to damp shallow slip. The difference with published models is reduced if the slip azimuth is allowed to vary.

6.2. Comparison With Published Postseismic Models

The few published postseismic models [*Evans and Meade*, 2012; *Ozawa et al.*, 2012] considered a smaller time period than the 279 days analyzed in this study. *Evans and Meade* [2012] considered 2 weeks of post-seismic relaxation and *Ozawa et al.* [2012], 7 months. Both of these studies found evidence for significant afterslip. *Ozawa et al.* [2012] report a postseismic moment of the order of 6.9×10^{21} N m after 7 months of afterslip, assuming a homogeneous half-space with a shear modulus of 40 GPa. *Evans and Meade* [2012] report a moment of 2.6×10^{21} N m over 2 weeks of afterslip, assuming a homogeneous half-space with a shear modulus of 58 GPa. If we consider the slip potency of our preferred model for the same time periods, we found that our model yields a slip potency 1.93 larger than the estimate of *Evans and Meade* [2012] and 1.65 larger than the estimate of *Ozawa et al.* [2012].

In both *Evans and Meade* [2012] and *Ozawa et al.* [2012], afterslip is located below the rupture area, in the ring-shaped region following the coastline. Our model also predicts this feature (see Figure 17). In our models, the average slip in this region varies from 1 to 2 m for the fixed azimuth model and from 2 to 3 m for the variable azimuth model. This value is lower but of the order of the value found by *Evans and Meade* [2012] (between 2 and 5 m) or *Ozawa et al.* [2012] (between 2 and 3 m). The main difference is that our models show, in addition, a zone with large afterslip near the trench.

An obvious reason for our larger estimate of the postseismic moment is that our analysis requires a fraction of the measured seafloor measurements to be postseismic. Other sources of differences between our models and the one proposed by *Ozawa et al.* [2012] are the boundary conditions and smoothing constraint. If we penalize postseismic slip near the trench, afterslip is forced to drift away from the trench (Figure A10). Actually, the model of Figure A10 obtained for a large value of the smoothing parameter, namely, $\gamma = 10^6$, resembles the postseismic model of *Ozawa et al.* [2012] (see Figure 10i of their paper), both in amplitude and spatial distribution. So the two ingredients for our postseismic model to mimic the model of *Ozawa et al.* [2012] is a locked trench and a large degree of smoothing.

The same factors explain the differences between our postseismic models and the one presented by *Evans and Meade* [2012]. Clearly, they penalize slip near the trench as do our blocked trench models of Figure A10, so that shallow afterslip is prohibited. The influence of the smoothing parameter is not comparable since *Evans and Meade* [2012] use a sparsity constraint which tend to favor slip at the patches which contributes most to the inland geodetic signal (hence beneath the coastline) rather than the Laplacian regularization used in this study and the work of *Ozawa et al.* [2012].

6.3. Characteristics of Shallow Afterslip

A distinctive characteristic of our study is that it implies a large fraction of shallow afterslip, updip of the epicenter of the Tohoku earthquake, which we have shown to be a robust feature of our inversion.

The details of the slip distribution near the trench are very poorly constrained though. For instance, comparison of Figures 8a and 14 shows that we cannot discriminate models with a single patch updip of rupture and models with two patches along the northern and southern edges of the rupture. The temporal evolution of shallow afterslip is also poorly constrained.

The data set does not allow discriminating potential spatial variations of the afterslip relaxation time. As only one component suffices to explain the temporal variations of postseismic geodetic displacements (i.e., the $\mathbf{V_2}$ eigenvector), the time evolution of afterslip is forced to follow everywhere on the fault the same time evolution. In reality shallow afterslip could have had a different time evolution over the fault, but this is not really resolvable with the available data set. Figure A3 of section A1. clearly shows that the decay of shallow afterslip is much faster than predicted by the decomposition results of inland data. The inland data

see essentially the time evolution of deep afterslip. This suggests that the relaxation of shallow afterslip is much faster than that of deep afterslip, possibly of the order of only 30–40 days (Figure A3) . This would be consistent with afterslip driven by frictional sliding as such a model requires the relaxation time to scale as the effective normal stress σ [*Perfettini and Avouac*, 2004a]. A faster relaxation is therefore expected at shallow depths, as suggested by the separate inversion of the sea bottom data (Figure A3). Therefore, it is very likely that our model fails to predict the correct time evolution of shallow afterslip by overestimating its duration.

Drill hole observations during the Japan Fast Drilling Program (JFAST) experiment demonstrate that no significant afterslip occurred on the megathrust 16 to 25 months after the main shock [*Fulton et al.*, 2013; *Chester et al.*, 2013]. So either no significant afterslip occurred at the location of the drill hole, and our preferred models erroneously predict some because of the smoothing effect of the regularization, or afterslip was mostly over at the time of the first drilling.

Also, although the time evolution of afterslip in our model does predict a relatively minor contribution of aseismic slip in the first day (based on the time function of Figure A2), it is possible that early afterslip would have contributed both to the tsunami and to the displacements of the seafloor, but not so much to the released seismic moment. Testing this hypothesis would require to do a similar study considering more geodetic measurements during the first day following the main shock. We leave this point for further studies.

6.4. Complementarity of Coseismic, Postseismic, and Interseismic Slip Distributions: Implications for the Return Period of M_w9.0 Earthquakes

In this section we discuss how the long-term slip on the megathrust is partitioned into seismic and aseismic slip. Our kinematic models suggest that, to first order, some areas of the megathrust are mostly creeping aseismically in the interseismic period (e.g., the white to pale yellow areas in Figures 11a and 11b) or in the postseismic period (e.g, the yellow to red areas in Figures 8a and 14). In addition, we observe that most of the seismic slip was released within the strongly locked area which actually seems to have ruptured entirely if the interseismic model with a creeping trench is retained (Figure 11b). If the interseismic model with a locked trench is selected (Figure 11a) then the deficit of slip accumulated near the trench in the interseismic period would need to be released by both seismic slip and afterslip. This kinematics is not very different from that of *Loveless and Meade* [2010] and is similar to first order with the kinematics observed on a number of subduction megathrust [e.g., *Konca et al.*, 2008; *Moreno et al.*, 2009; *Perfettini et al.*, 2010] and as well as on some continental faults [e.g., *Harris and Segall*, 1987; *Hsu et al.*, 2006b].

There are however important differences. While, as noticed by *Evans and Meade* [2012], deep afterslip show only very limited overlap with the coseismic rupture, the shallow afterslip largely overlap with the coseismic rupture (Figure 8a). This situation is very different with the complementarity observed, for example, in the case of the M_w8.6 Nias earthquake, offshore Sumatra, or the M_w8.0 Pisco earthquake, offshore Peru, which both triggered significant shallow afterslip but with very limited overlap of the coseismic and postseismic slip distributions [*Hsu et al.*, 2006a; *Perfettini et al.*, 2010].

The slip budget on the megathrust is closely related to the return period of large earthquakes as in the long run seismic and aseismic slip must match the 80 cm/yr long-term slip rate on the megathrust. This return period might be estimated assuming that (i) the seismic moment released is dominated in the long run by earthquakes similar to the 2010 Tohoku-Oki event and (ii) the pattern of interseismic coupling measured over the two decades preceding the Tohoku-Oki earthquakes is stationary in time and can be extrapolated throughout the interseismic period.

Assuming that the characteristic magnitude of the repeating event is $M_W = 9.0$ ($M_0 \approx 4\,10^{22}$ N m), we can estimate the recurrence time T_{rec}

$$T_{\text{rec}} = \frac{M_{\text{coseismic}} + M_{\text{postseismic}}}{\dot{M}_0}, \tag{8}$$

the estimated period over which a deficit of moment equivalent to the moment released by seismic slip and afterslip in 2011 would have accumulated at the current rate of interseismic stress buildup. In

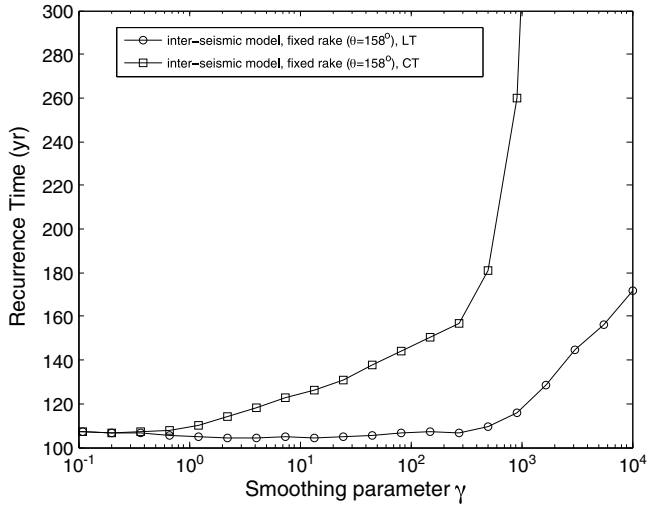

Figure 18. Estimated recurrence times for a uniform slip azimuth ($\phi = 292°$) coupling model with a locked trench (label BT) or creeping trench (label CT).

equation (8), $\dot{M}_0$ is the total moment rate predicted by our coupling model in the area of interest (between −200 km south and 400 km north in Figure 11a or 11b).

Figure 18 shows the recurrence times as a function of the smoothing parameter γ. As discussed in section A2.2., a reasonable compromise between data fitting and model roughness is obtained for a smoothing parameter in the range $\gamma = 1$–100. For this range of smoothing parameters, we found the recurrence time T_{rec} in the range $T_{rec} = 100$–150 years. The upper bound is obtained for a coupling model with creeping trench while the lower bound corresponds to a locked trench in the interseismic period. Such a short return period is at odd with the known seismicity in the Tohoku-Oki area where only one major tsunamigenic earthquake, the A.D. 869 Jogan earthquake [*Sawai et al.*, 2008, 2012; *Sugawara et al.*, 2012], exceeded a magnitude M_w8.5 over the historical period [*Tsumura*, 2005]. In addition paleotsunami investigations revealed only two comparable events in the past 3000 years [*Minoura et al.*, 2001]. This reasoning neglects the contribution of more moderate earthquakes than Tohoku-Oki and of tsunami earthquakes, like the 1896 Sanriku earthquake, which have been quite frequent over the historical period (Table 1).

Figure 19 shows the cumulated moment due to interseismic loading (averaged over the fault) as a function of time, going backward in time starting in 2011, together with the cumulated moment due to the Tohoku-Oki earthquake (coseismic and postseismic contribution) and the historical earthquakes of Table 1. The interseismic moment crosses the seismic moment around 1800 to 1850. So taking into account the moment released by other earthquakes than Tohoku-Oki, T_{rec} increases from about 100–150 years to 150–200 years. Such a return period is still way too small in view of the historical and paleotsunami records.

A more comprehensive way of assessing slip budget and the return period of Tohoku-Oki-like earthquakes consists in adding coseismic, postseismic, and interseismic slip and determine whether these distributions sum to a uniform slip distribution and, if so, for what duration of interseismic loading. Again, we will assume that interseismic coupling is stationary, but we now take into account past known earthquakes. In this analysis we consider all possible boundary conditions: (i) a free trench model where slip is allowed near the trench (but not on the other edges of the fault) and (ii) a blocked trench model where slip is penalized near the trench. Figure 20 shows the temporal evolution of the interseismic, coseismic, and postseismic slip profiles as a function of depth-averaged along strike within a 600 km wide swath ([−200; 400] along the north axis of Figure 11). Due to the various possible combinations of boundary conditions at the trench for each of the three phases of the cycle, we ended up with eight possible scenarios. We refer to each profile using the label cosXpostYinterZ. The labels *X* and *Y* of the coseismic and postseismic slip models can take the values FT or BT, the first one meaning that a free trench boundary condition is used (allowing slip near the trench), while the second one corresponds to a blocked trench (for which slip is inhibited near the trench). For the interseismic model, the label *Z* can take the values BT for a blocked trench or CT for a creeping trench (Figure 20). We plot the cumulated average slip since the time indicated in abscissa which goes backward starting at $t_1 = 2012$. We use this plot to assess whether it is possible to close the slip budget over a certain period that would represent the duration of the seismic cycle. The criterion is that over a cycle, the cumulated interseismic, coseismic, and postseismic slip over this return period should be the same at all depths. That would mean that the deficit slip accumulated during the interseismic period would be perfectly balanced by seismic slip and afterslip. We neglect the afterslip due to the moderate earthquakes as well as possible slow earthquakes for lack of any reliable information.

Table 1. Composite Catalog of Historical Seismicity in the Rupture Area of the Tohoku-Oki Earthquake[a]

Source	Year	Magnitude	Longitude	Latitude
Sawai et al.	869	8.4	142.34414063800	37.63329059290
Figure 4-1	1611	8.1	143.00000000000	39.00000000000
Figure 4-1	1616	7.0	142.01268607500	38.08597738070
Figure 4-1	1677	7.4	142.22331253800	41.00398220820
Figure 4-1	1678	7.5	142.50730327600	38.99238115120
Figure 4-1	1717	7.5	142.50966986500	38.48829759220
Figure 4-1	1763	7.4	142.22331253800	41.00398220820
Figure 4-1	1763	7.3	142.01978584300	41.00634879770
Figure 4-1	1763	7.0	142.01978584300	41.00634879770
Figure 4-1	1772	7.5	143.51310380400	39.50119788910
Figure 4-1	1835	7.0	142.50966986500	38.48829759220
Figure 4-1	1855	7.3	142.01268607500	38.08597738070
Figure 4-1	1856	7.5	142.20201323300	41.11994509270
Figure 4-1	1858	7.3	142.01978584300	40.75075713400
Tanioka [1996]	1896	8.3	143.78948512300	39.27867855840
Figure 4-2	1897	7.4	141.98835342600	38.41057647660
Figure 4-2	1897	7.7	143.58655344000	38.39377857860
Figure 4-2	1898	7.2	141.97875462800	38.60495215390
Figure 4-2	1901	7.2	142.46829337000	40.51511313040
Figure 4-2	1901	7.4	142.97223031100	40.55110862620
Figure 4-2	1915	7.5	142.88584112200	38.59535335500
Figure 4-2	1931	7.6	142.95543241300	40.81747529510
Figure 4-2	1936	7.5	142.06274411800	38.05062151870
Figure 4-2	1937	7.5	141.63309858600	36.85162833250
Figure 4-2	1938	7.4	141.81155816100	37.31562322860
Figure 4-2	1938	7.3	141.81155816100	37.04793386550
Figure 4-2	1938	7.0	141.58550936600	36.70588634590
Figure 4-2	1960	7.2	143.39457746200	39.85279600790
Figure 4-2	1968	7.5	143.38257896300	41.23742274590
Utsu [1999]	1968	8.2	143.58000000000	40.73000000000
Figure 4-2	1978	7.4	142.16833090500	38.42017527550
Figure 4-2	1989	7.1	143.02982310500	39.87919270480
Figure 4-2	1994	7.5	142.87864202200	40.39032874500

[a]Figures 4.1 and 4.2 refer to the "National Seismic Hazard Maps for Japan" report [*Tsumura*, 2005].

The contribution of historical earthquakes is estimated based on the $M_w > 7$ events listed in Table 1. The estimated rupture areas of these events and their epicenters are shown in Figures 17 and 21. They indeed mostly occurred in areas which had remained locked in the interseismic period and relocked in the postseismic period (except for the 1896 tsunami earthquake which seems to overlap with the shallow afterslip patch, even more so if the postseismic model of Figure 14 is considered rather than the reference models of Figure 8a or 5c). This correlation suggests that those earthquakes indeed contributed to balance the interseismic deficit of slip. To estimate their coseismic slip distributions, we assume circular ruptures with uniform slip assuming a constant stress drop of 3 MPa [*Kanamori and Anderson*, 1975]. We consider all the events between 1700 and the ending year of our study $t_1 = 2012$. The contribution of these events is reported as magenta lines in Figure 20.

None of the kinematic models tested there really allow closing the slip budget (Figure 20). The scenario that is the closest to produce a balanced slip budget is the case "cosFTpostBTinterBT." The isochrons get nearly flat by about 1700–1750. If so this would suggest a return period of 250–300 years. This value is similar although larger to the value estimated above but seems still too short. The case cosFTpostBTinterBT implies that near the trench coseismic slip is allowed while afterslip and interseismic slip are inhibited. From a rheological point of view, the boundary conditions of this scenario would imply rate weakening near the trench, in contradiction with our common view of subduction zones [*Hyndman et al.*, 1997; *Scholz*, 1998]. These slip budget plots show that a longer return period would imply either not documented mechanisms of

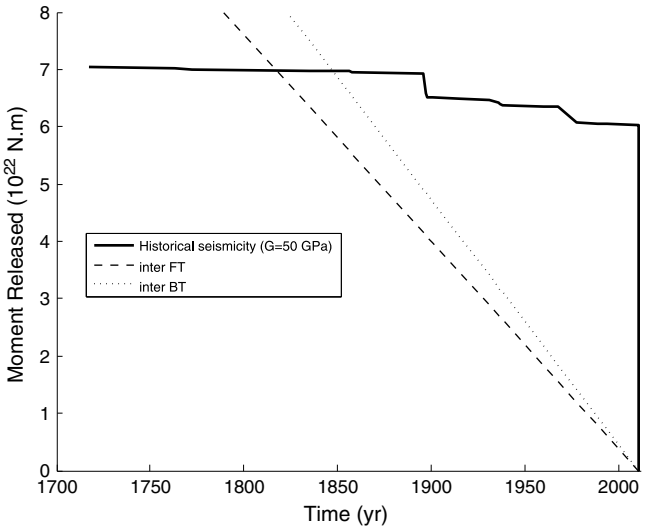

Figure 19. Accumulated interseismic moment as a function of reversed time (dotted line: locked trench model, dashed line: creeping trench model). The cumulated moment due to the historical seismicity is also displayed assuming a shear modulus of 50 GPa (thick continuous line).

strain release in the seismogenic depth range (major slow earthquakes for example) or, equivalently, a lesser rate of accumulation of slip deficit in the interseismic period. If the return period of earthquakes similar to Tohoku-Oki is indeed of the order of 1000 years as suggested by the historical and paleotsunami records, the deficit of slip potency accumulated over such a period of time would be extremely large. The rate of M_w7.0 to M_w8.2 over historical times is at least 1 order of magnitude too small to play any role in releasing this interseismic strain. A possible explanation might be that the historical period would have been particularly quiet compared to the millenary average, possibly as a manifestation of the ending of the seismic cycle associated to Tohoku-like earthquakes. This hypothesis would imply a significant deficit of slip in the 30–50 km depth range for the M_w7.0–8.2 earthquakes over historical times. This assumption could therefore provide an explanation for the paradoxical observation that interseismic deformation, as well as coseismic and postseismic deformation due to the Tohoku-Oki earthquake have all contributed to a net subsidence of the coastal area while uplifted marine terraces show a long-term uplift rate of the order of 0.1 mm/yr [*Matsu'ura et al.*, 2009].

In any case, it is difficult to balance the slip budget over historical times with the assumptions made in this section. We conclude that the known seismicity provides an incomplete picture of the long-term seismic behavior of this portion of the Japan megathrust or that some of the assumptions entering the analysis are incorrect. We can think of three possibilities:

1. The long-term (or plate) velocity is variable during the seismic cycle. This is a plausible explanation supported by observations following very large earthquakes [*Freymueller and Beavan*, 1999; *Khazaradze*

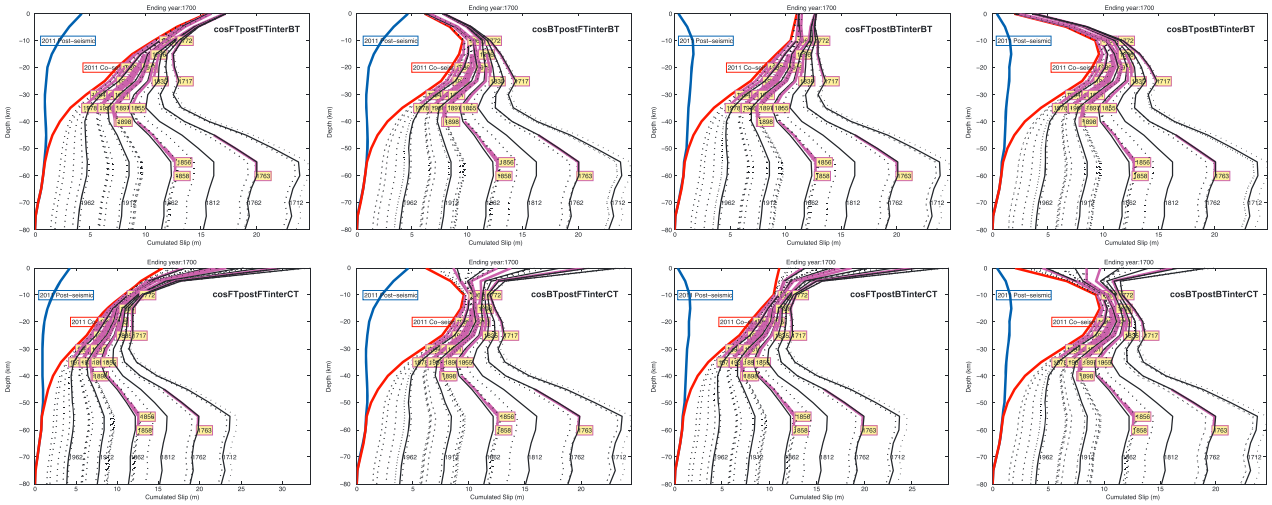

Figure 20. Coseismic (red line), postseismic (blue line), and interseismic (black lines) slip profiles averaged with depth considering various boundary conditions. Each thick line corresponds to a 50 year interval of interseismic accumulation. Seismic slip due to the major historical earthquakes listed in Table 1 is also shown (pink lines), with dates outlined in yellow.

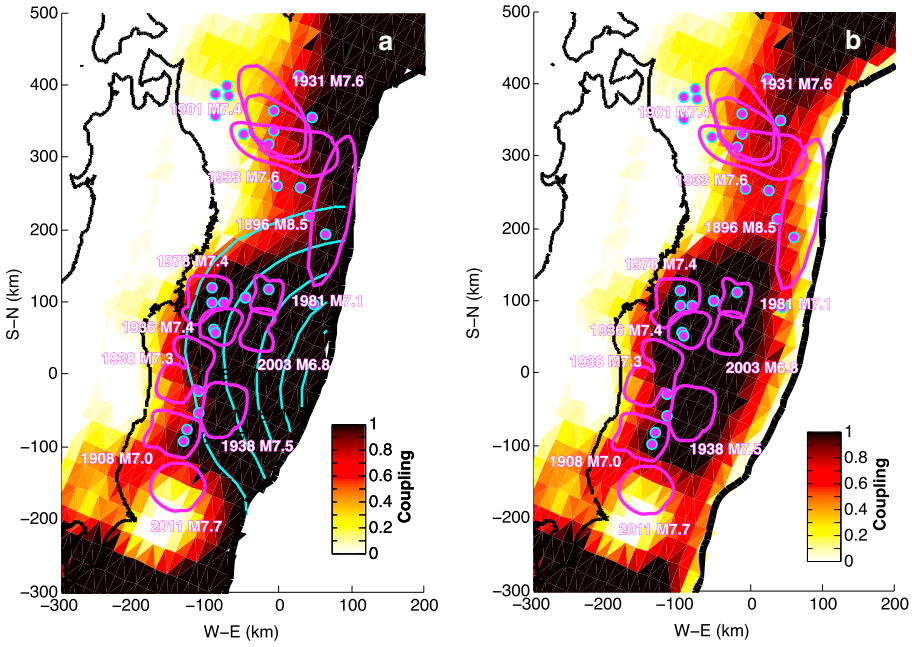

Figure 21. (a) Comparison between the location of historical seismicity (magenta circles with cyan border) and our preferred coupling model with blocked trench (Figure 11a). The pink contours correspond to the historical events considered by *Johnson et al.* [2012]. The cyan contour corresponds to our preferred coseismic model of Figure 6a. (b) Same for the coupling model with creeping trench (Figure 11b).

et al., 2002] and stress-driven models of the seismic cycle which take into account viscoelastic relaxation [*Johnson and Segall*, 2004; *Perfettini and Avouac*, 2004b; *Perfettini et al.*, 2005].

2. Some permanent (inelastic) deformation builds up during the cycle so that the stored elastic energy is lower than our estimates obtained assuming a pure elastic medium (hypothesis of the back slip model of *Savage* [1983]). Inelastic deformation off the subduction interface is documented within the accretionary prism [*Fujiwara et al.*, 2011] but could, in fact, affect the fore arc at the larger scale.
3. Interseismic coupling varies over the seismic cycle [e.g., *Nishimura et al.*, 2004].

In any case, it is probable that the shallow portion of the plate interface (at depth less than about 15 km) both slip as a result of aseismic slip and of seismic slip during infrequent mega-earthquakes. Despite the wealth of data available on that area, it is not possible to determine accurately the relative contribution of these two modes of slip.

6.5. Frictional Properties of the Megathrust

In this section, we use our kinematic description of seismic an aseismic fault slip to derive some constraints on the spatial distribution of the frictional properties of the megathrust in the area of the 2011 Tohoku-Oki earthquake.

Figure 22 shows the evolution of afterslip at the center of the site of peak postseismic slip (Figure 8a). First, the areas which are creeping aseismically in the interseismic and postseismic period should obey a rate-strengthening friction law so that aseismic slip is promoted [*Marone*, 1998]. More precisely, the time evolution of afterslip (Figure 22) is quantitatively consistent with experimental friction laws according to which friction is a logarithmic function of the sliding rate. If rate and state friction is assumed, the evolution of afterslip $S(t)$ is logarithmic according to [*Marone et al.*, 1991; *Perfettini and Avouac*, 2004a; *Perfettini et al.*, 2010]

$$S(t) \approx V_L t_r \log\left(1 + \frac{V^+}{V_L t_r} t\right), \tag{9}$$

where V_L is the long-term sliding velocity, V^+ the velocity of the rate-strengthening patch at the end of the coseismic phase, and t_r the relaxation time of afterslip. The analytical function predicted by equation (9) is indeed found to predict quite accurately the time evolution of afterslip. This observation was reported

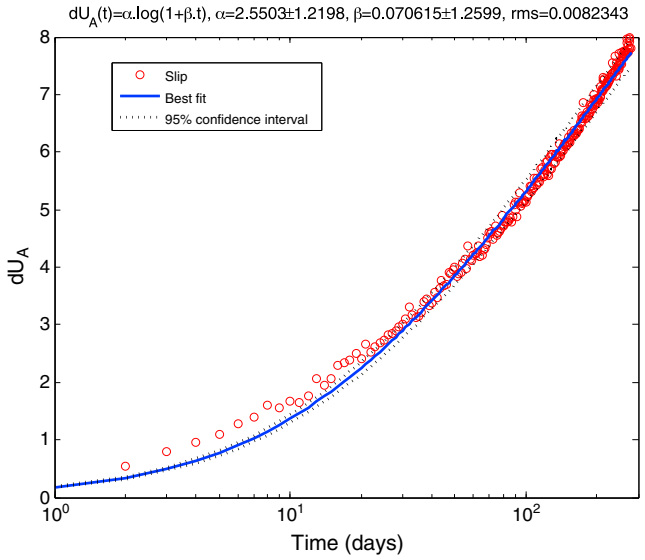

Figure 22. Evolution of afterslip at the location of peak afterslip (averaged over a 20 km radius). As only one component is used in addition to the one describing the coseismic phase the time evolution in our model is the same at all afterslip patches. This time evolution is well fitted from the one single of freedom analytical law [*Perfettini and Avouac*, 2004a].

already by *Ozawa et al.* [2012] and a similar behavior has been observed following a number of recent large megathrust events including the 2003 (M_w8.0) Tokachi-Oki earthquake [*Miyazaki et al.*, 2004], the 2005 (M_w8.6) Nias earthquake [*Hsu et al.*, 2006a], the 2007 (M_w8.0) Pisco earthquake [*Perfettini et al.*, 2010], and the 2010 (M_w8.8) Maule earthquake [*Lin et al.*, 2013]. As shown by these studies, this observation can be used to quantify the rate dependency of friction. In the present case, we find that the best fit to the data is obtained for $V_L t_r \approx 2.55 \pm 1.22$ m, and $V^+ \approx (2.08 \pm 38.2)\,10^{-6}$ m/s. Uncertainties are given at the 95% confidence level. We leave the discussion of the corresponding frictional parameters to a follow up study. As also observed by *Fukuda et al.* [2013], the model does not fit the early period of afterslip (over the first 20 days) suggesting that a better fit could be obtained assuming, for instance, temporal changes of frictional parameters [*Fukuda et al.*, 2013].

Most of the historical events lie at the bottom of the strongly coupled areas (Figure 21). This observation makes sense given that the boundary between the strongly coupled (locked) regions and the weaker (creeping) part of the fault is the zone where the rate of stress buildup is expected to be maximum in the interseismic period and where the highest seismicity rates are observed as well documented in some other contexts [*Ader et al.*, 2012]. So, as conjectured in a number of studies in the past [e.g., *Lay et al.*, 1982], one can imagine that the megathrust is paved with asperities capable of nucleating earthquakes, presumably characterized by a rate-weakening friction law, embedded in zone of dominantly aseismic creep, characterized by a rate-strengthening law. The variability of earthquakes would then arise from the interactions of these asperities which would be capable of rupturing independently or jointly [*Kanamori and McNally*, 1982; *Rundle and Kanamori*, 1987; *Konca et al.*, 2008; *Kaneko et al.*, 2010; *Dublanchet et al.*, 2013].

The frictional behavior of the shallow portion of the megathrust is more enigmatic. The significant overlap of coseismic and afterslip suggests either a neutral dependency of friction to sliding velocity or the possibility that the rate dependency can occasionally change from rate strengthening at low sliding rate to rate weakening at higher rate. Laboratory experiments at low-stressing rate on lithologies thought to govern the frictional behavior of megathrust generally show a rate-strengthening behavior [*Saffer and Marone*, 2003; *Ikari and Saffer*, 1998; *den Hartog et al.*, 2012a]. A transition to rate weakening at high sliding rate has also been documented in laboratory experiments in particular for megathrust lithologies thought to be characteristic of megathrust settings [*Reinen et al.*, 1991, 1994; *Niemeijer and Spiers*, 2009]. Such a behavior can be also observed in seismic cycle models due to thermal pressurization of pore fluids [*Sibson*, 1992; *Noda and Lapusta*, 2013]. This mechanism would be consistent with the near complete stress drop on the shallow portion of the megathrust during the Tohoku-Oki earthquake [*Hasegawa et al.*, 2011] and its very low apparent friction, estimated to be less than 0.01 [*Cubas et al.*, 2013]. It seems reasonable to assume that this destabilizing effect can be strong enough to compensate for the damping of the seismic rupture when entering the shallow portion with intrinsically rate-strengthening frictional behavior. In that regard, it is interesting to note that most M_w7.0 to M_w8.2 earthquakes are inferred to have rupture the portion of the megathrust thought to be locked in the interseismic period (Figure 21) and relocked right after the Tohoku earthquake (Figure 17). The only recent historical event that stands in a region of large afterslip is the 1896

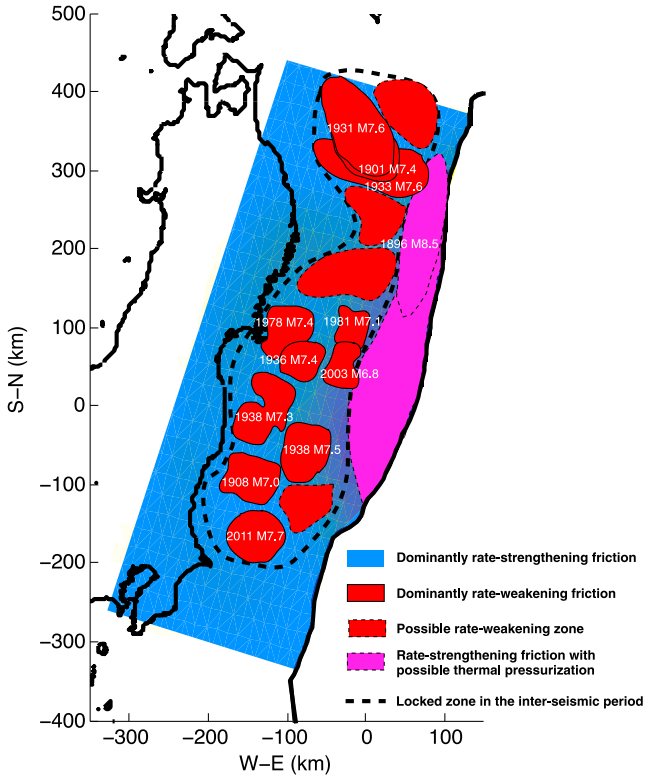

Figure 23. Schematic representation of a possible distribution of rate-strengthening and rate-weakening regions on the Japan megathrust in the area of the Tohoku-Oki earthquake.

tsunami earthquake. Note also that the tsunami source of the 869 Jogan earthquake correlates well with our region of maximum afterslip near the trench [see *Lay et al.*, 2011, Figure 1]. Consequently, we believe that the shallow zone of afterslip might, in fact, represents a rate-strengthening region which can occasionally transition to rate weakening and become tsunamigenic as happened in 2011, 1896, and 869. This tsunamigenic area might actually mostly creep in the interseismic period although it is difficult to demonstrate it based on the interseismic models, the locked and creeping trench models nearly equally adjusting the interseismic data. On the other hand, the slip budget considerations of section 6.4 tend to favor a locked trench in the interseismic period, as would be the case if this rate-strengthening region was screened by the locked rate-weakening region below, as result of a stress shadow effect [*Burgmann et al.*, 2005]. So the most reasonable scenario would be that this region is slowly creeping in the interseismic period but can release large amount of slip when perturbed, for instance, by the rupture of a nearby brittle asperity.

Figure 23 shows a schematic picture of the main thrust interface in the region of the Tohoku-Oki earthquake. The seismogenic zone (Figure 23, dashed contour) would correspond to the region locked during the interseismic period and is constituted from a mosaic of rate-weakening patches corresponding to the past historical ruptures, embedded in a rate-strengthening region. Above the seismogenic zone would be the tsunamigenic zone (Figure 23, magenta region) mentioned previously and corresponding to our region of maximum afterslip. The largest tsunamis such as those following the 869, 1896, and 2011 earthquakes would be observed when this shallow region of the fault slips during the coseismic phase. The rest of the fault would be composed of rate-strengthening regions which creep steadily during the interseismic period and basically as the logarithm of time in the postseismic phase.

Considering a blocked trench raises some strong concerns, too. Such an assumption is in contradiction with the well admitted idea that the shallow part of faults is aseismic [*Hyndman et al.*, 1997; *Scholz*, 1998]. Assuming a locked trench (i.e., the BT boundary condition) pushes the region of large afterslip to depth. This implies that rupture would have had to cross a stable region before reaching its peak slip near the trench. If we refer as earlier to the paradigm that stable regions damp rupture then somehow seismic rupture would have had to slow down at middepths, which is not observed [e.g., *Ide et al.*, 2011; *Meng et al.*, 2011; *Wei et al.*, 2012]. The existence of a stable region at middepths would also contradict the spatial distributions of interseismic slip and historical seismicity (Figure 21).

In any case, the notion that stable sliding regions systematically impede seismic rupture does not seem to apply to the Tohoku-Oki earthquake, suggesting that such areas might be rate-strengthening at low stressing rate and rate weakening at fast stressing rate. This behavior is observed in the lab for Serpentinite [*Reinen et al.*, 1991, 1992] and could also result from thermal pressurization [*Noda and Lapusta*, 2013]. The magnitude of the tsunami clearly demonstrates that coseismic slip was large near the upper part of the fault. This behavior might be typical of the shallow potentially tsunamigenic areas of megathrusts but could also be more general.

7. Conclusion

The 2011 Tohoku-Oki earthquake is exceptional because of the abundance and quality of the data available to constrain the event itself, its after effects, and preseismic deformation but also because of the possibility to place this information in the context of a well-documented historical seismicity.

To determine coseismic and postseismic models, we benefited from the inland data collected by the GEONET network and seafloor campaign measurements at six sites located as close as 100 km from the trench. The methodology adopted in this study allowed estimating the contribution of postseismic deformation to the seafloor measurements. Thanks to those stations, the resolution of the model is greatly improved near the trench compared to the resolution afforded by the inland data only (Figure 3). In spite of these sea bottom data, some uncertainties remain regarding the amount of coseismic slip near the trench and the degree of locking of that area in the interseismic period (recall that the models of Figures 11a and 11b adjust the data equally well).

We find that the earthquake was followed by afterslip both downdip and updip of the coseismic rupture. The time evolution of afterslip is consistent with experimental rate-strengthening friction law as pointed out by *Ozawa et al.* [2012], although there is indication that the frictional properties might have changed during postseismic relaxation [*Fukuda et al.*, 2013]. The most outstanding feature of our analysis is the evidence for both seismic slip and aseismic afterslip near the trench. This finding contrasts with published studies which only evidenced the strip of afterslip along the downdip edge of the rupture area [*Evans and Meade*, 2012; *Ozawa et al.*, 2012]. We believe those differences to be mostly due to the choice of the boundary conditions (free versus locked trench) and the degree of smoothing of the slip inversions, together with the fact that our inversion scheme naturally separates the postseismic contribution from the coseismic one unlike previously published works. The time evolution of shallow afterslip is poorly resolved however; but there is indication that shallow afterslip might have decayed much faster than deep afterslip. The zones with seismic and aseismic behavior in the deeper 40–60 km depth range complement each other quite nicely as reported in particular in the previous study of *Evans and Meade* [2012]. The large overlap between the shallow afterslip zone and the coseismic rupture contrasts with the complementarity observed at depth.

We also find that the Tohoku-Oki earthquake initiated in an area of the megathrust which had remained locked in the interseismic period and within which most of the M_w7.0 to 8.2 historical ruptures had occurred. The 20–40 km deeper portion of the megathrust can therefore be interpreted as a zone where rate-weakening patches are dominant and can rupture either independently or collectively. The main shock in 2011 ruptured most of this area and propagated upward near the trench. Whether this area was locked or creeping in the interseismic period is more difficult to assess given the lack of resolution of the inversions, as already pointed out by *Loveless and Meade* [2011]. It is likely that aseismic slip there is essentially triggered by seismic ruptures, a mechanism that could explain as well tsunami earthquakes such as the 1896 Sanriku earthquake. The difference with the 2011 event would be that the triggering seismic event would have been quite smaller in 1896.

Constraining the return period of M_w9.0 earthquakes in the Tohoku-Oki area is a challenge since, as pointed to by *Avouac* [2011], simple slip budget consideration lead to estimates of the order of centuries way too short in view of the historical record. It is however clear that the seismicity prior to 2011 was way short of balancing the rapid accumulation of slip potency deficit in the area [*Suwa et al.*, 2006; *Hashimoto et al.*, 2009; *Loveless and Meade*, 2011], calling for the need of either larger or more frequent earthquakes that reported in historical catalogs. By contrast, it would have been difficult to anticipate the amount of coseismic slip near the trench which occurred in 2011, in an area thought to generally damp seismic rupture.

Appendix A: Sensitivity Tests

A1. Results of the PCAIM Decomposition

Figures A1 and A2 present the result of the PCAIM decomposition described in 3.2. The first component (Figure A1) is imposed to be a Heaviside function in order to mimic the coseismic step. The second component (Figure A2) is left free and is observed to evolve approximately as the logarithm of time (see section 3.2 for more details).

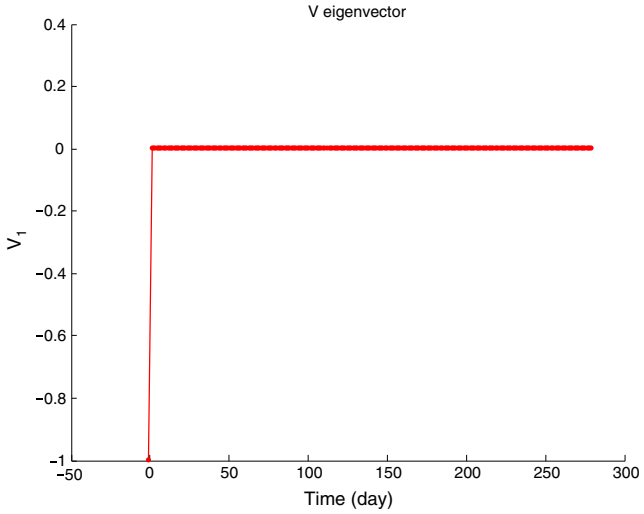

Figure A1. Time function associated to the first component of the PCAIM decomposition ($\mathbf{V_1}$). A step function is imposed to isolate the coseismic phase.

Figure A3 shows the $\mathbf{V_2}$ eigenvectors considering the offshore data alone, the inland data alone, and the combination of those two data sets. The decomposition results are only shown starting from day 17, the first day of the offshore measurements. The $\mathbf{V_2}$ vectors have been all shifted to start at a value of 1 for easier comparison. Not surprisingly, the results of the decomposition are nearly identical considering the inland data alone or together with the offshore data, the latter weighting very little in the decomposition. The most interesting feature is that the vector $\mathbf{V_2}$ obtained considering the decomposition of the offshore data alone shows a much faster decay than when considering inland stations, suggesting that the decay of shallow afterslip is much faster than deep afterslip. These results should be taken with caution given the limited amount of data and the fact that the time series is the result of combining epochs from different sites.

A2. Sensitivity to Smoothing and Slip Azimuth Constraints

A2.1. Coseismic and Postseismic Models

Rougher models always provide a better fit to the data, but they might be meaningless due to the possibility that the improved fit would be due to the ability of the model to fit noise in the data. Smoother models are useful to get a picture of the average slip models but do not adjust the data properly. A compromise needs to be found.

A common way to select the optimal value of the smoothing parameter is to plot the misfit to the data as a function of the smoothing parameter [*Hansen*, 1992]. Two regimes are generally observed and the optimal value of the smoothing parameter corresponds to the departure from the rough regime toward the smooth one.

We consider two types of models with either free or fixed slip azimuth. For each of those models, we consider two distinct boundary conditions (BC): (i) a free trench model where slip is authorized near the trench or (ii) a blocked trench model where slip is penalized near the trench. The BC can be set independently for each component, meaning that a given BC can be assigned to the coseismic phase, while a distinct BC is assumed for the second component describing postseismic slip. We start by considering the variable azimuth models.

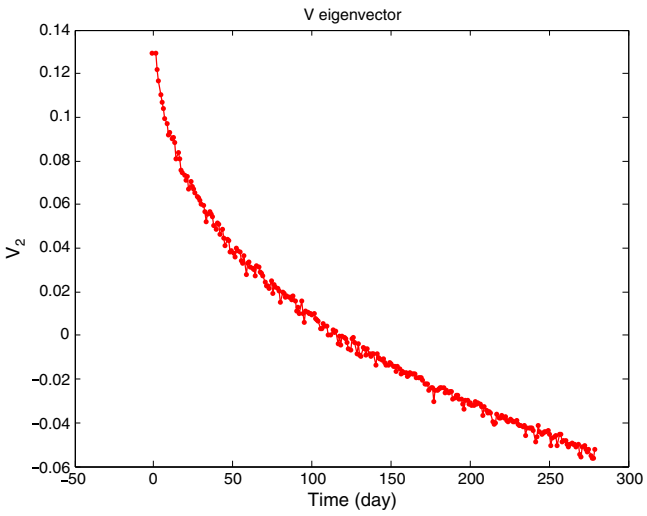

Figure A2. Time function $\mathbf{V_2}$ associated to the second component of the PCAIM decomposition. The function follows approximately a logarithmic evolution typical of postseismic relaxation.

Figure A4 shows the reduced chi-square as a function of the smoothing parameter considering the variable and fixed azimuth models with free or blocked trench. Depending on the BC assumed for

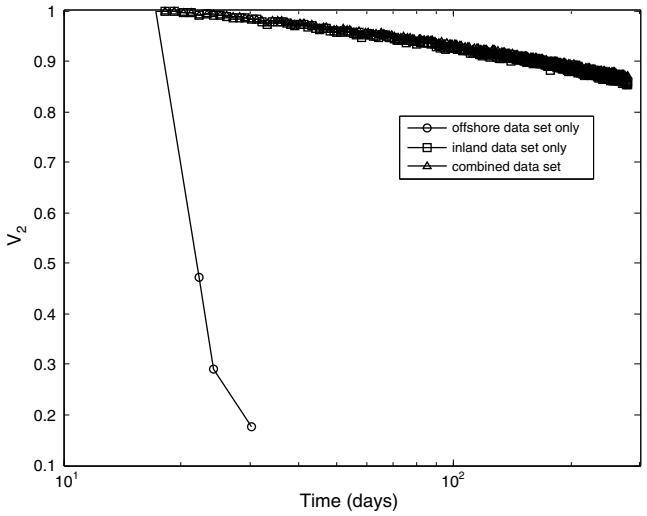

Figure A3. Time function $\mathbf{V_2}$ associated to the second component of the PCAIM decomposition for (1) the offshore data set only (open circles), (2) the inland data set only (open squares), and (3) both the inland and offshore data (open triangles). Note the logarithmic time scale.

each component (or phase) of the model, four combinations exist. The best fit is obtained for the cosFT and postFT models that correspond to a freely slipping trench during both the coseismic and postseismic phase, while the worst model corresponds to the cosBT and postBT case. We will retain the cosFT and postFT case as our reference model. For the models of Figure A4, a value of the smoothing parameter of the order of $\gamma = 5 \times 10^5$ appears to offer the best compromise.

It is interesting to impose the slip azimuth because the inversion is less ill-posed than when the azimuth is left free. Also it allows imposing a consistency between the azimuth of plate convergence and the interseismic, coseismic, and postseismic slip. The issue is that, in reality, slip azimuth might be variable so that imposing a uniform value could substantially degrade the fit to the data. In practice, there is some trade-off between slip amplitude and slip azimuth variations so that imposing a constant slip azimuth is generally not penalizing much the fit to the data.

Figures 5a and 5b show the coseismic and postseismic free azimuth models considering a free trench BC for both the coseismic and postseismic phases. For both figures, the slip azimuth distribution is fairly homogeneous. For the postseismic case of Figure 5b, some variations in the slip azimuth are observed, but they are mostly located on the northern edge of the fault which is the most distant from the GPS network. Consequently, they can be ignored and we will consider that a uniform slip azimuth approximation is satisfying.

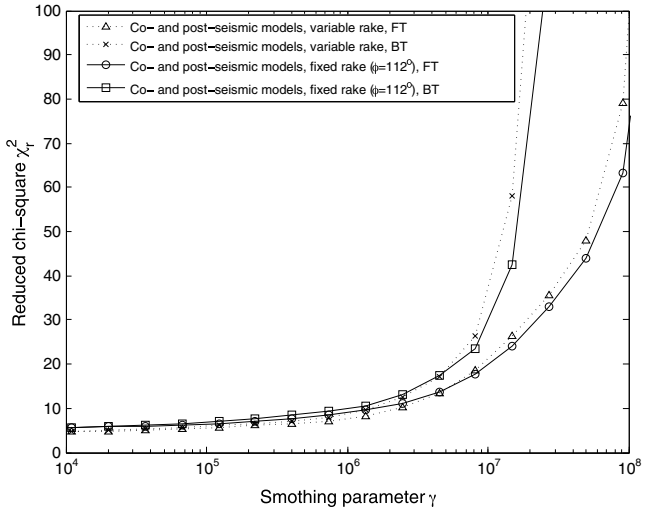

Figure A4. Reduced chi-square as a function of smoothing parameter γ for the coseismic and postseismic free and fixed rake models with free or blocked trench. The legends mean as follows: cosBT and postBT = blocked trench for the coseismic or postseismic model. cosFT or postFT = freely slipping trench for the coseismic or postseismic models.

Figure A5 shows the misfit to the data as a function of the slip azimuth ϕ considering the free (FT for free trench) or blocked (BT for blocked trench) trench model for both the coseismic and postseismic phases, assuming a smoothing parameter of $\gamma = 5 \times 10^5$ corresponding to our optimal value. The lowest misfit is obtained for an optimal value of $\phi \approx 112°$. This value is retained when assuming a uniform tectonic deformation. We refer to it as the "fixed azimuth" model.

A2.2. Interseismic Models

The seismic coupling is obtained by normalizing the deficit of slip in the interseismic period by the long-term slip rate. In the case of the Tohoku-Oki area, we normalize the inverted velocity field by the value $V_{pl} = 80$ mm/yr (the slip rate on the Japan Megathrust determine by *Loveless and Meade*

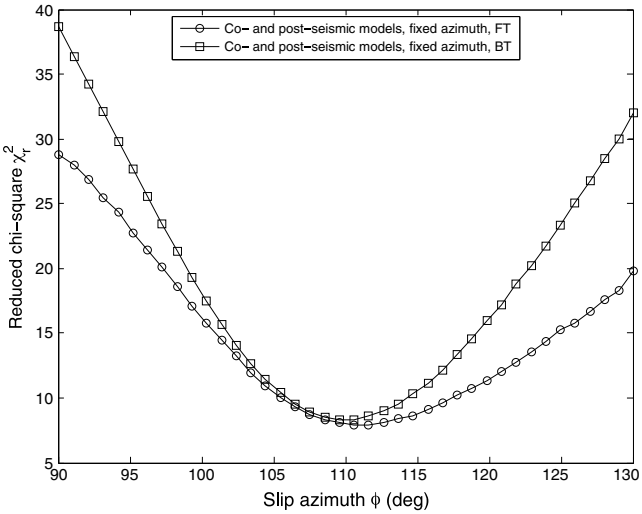

Figure A5. Reduced chi-square as a function of the slip azimuth ϕ for the coseismic and postseismic models with free or blocked trench. The smoothing parameter is set to $\gamma = 5 \times 10^5$.

[2010]). In a back slip model, a coupling of 0 means that the area is creeping at the plate velocity V_{pl}, while a coupling of 1 means that the fault is locked.

The interseismic velocities are forced to stand in the range $[-V_{pl}; V_{pl}]$ in free rake models. The interseismic velocities is imposed to stand in the range $[0; V_{pl}]$ in fixed rake models (meaning that interseismic slip is imposed to have thrust component). We refer to this condition as a positivity constraint.

Figure A6 shows the reduced chi-square as a function of the smoothing parameter γ considering the free rake models with a locked or creeping trench and the fixed azimuth models with the same boundary conditions. For all those models, a value of the smoothing parameter of the order of $\gamma = 10$ appears to be a good compromise and will be retained so far as the optimal smoothing parameter for the coseismic and postseismic models.

Figures A7a and A7b show that for whatever boundary conditions considered (LT or CT for locked trench or creeping trench) in free rake models, slip azimuth is nearly constant. This shows that it is probably valid to assume a constant slip azimuth.

Figure A8 shows the misfit to the data as a function the slip azimuth ϕ for fixed azimuth models with either a locked or creeping trench BC. The smoothing parameter is set to the optimal value of $\gamma = 10$. The lowest misfit is obtained for an optimal value of $\phi \approx 298°$ close to the $\phi = 292°$ optimal slip azimuth of the coseismic and postseismic fixed rake models. For consistency a slip azimuth of $\phi = 292°$ is assumed in the fixed rake models used to build our models of the seismic cycle combining coseismic, postseismic, and interseismic phases.

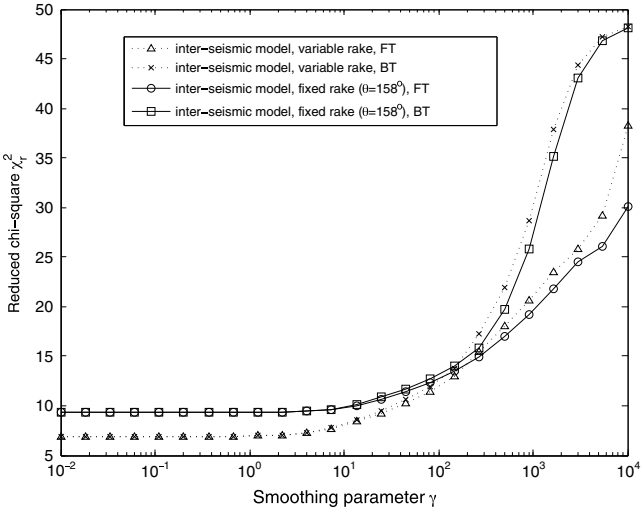

Figure A6. Reduced chi-square as a function of smoothing parameter γ for the interseismic model with free or blocked trench, considering the free or fixed rake models.

A3. Sensitivity to Smoothing

Figure A9 presents the coseismic and postseismic free trench models for a smoothing parameter of $\gamma = 10^4$, 5×10^4, 10^5, 5×10^5, and 10^6 ($\gamma = 5 \times 10^5$ is the value we consider to be optimal based on Figure A4). Figure A10 presents the corresponding coseismic and postseismic blocked trench models. It should be noted that in both cases the overlap between coseismic and postseismic slip decreases for rougher models.

Figure A11 presents the interseismic models for a smoothing parameter of $\gamma = 1$, 5, 10, 50, and 100 considering a locked or creeping trench ($\gamma = 10$ is the value we consider to be optimal based on Figure A6).

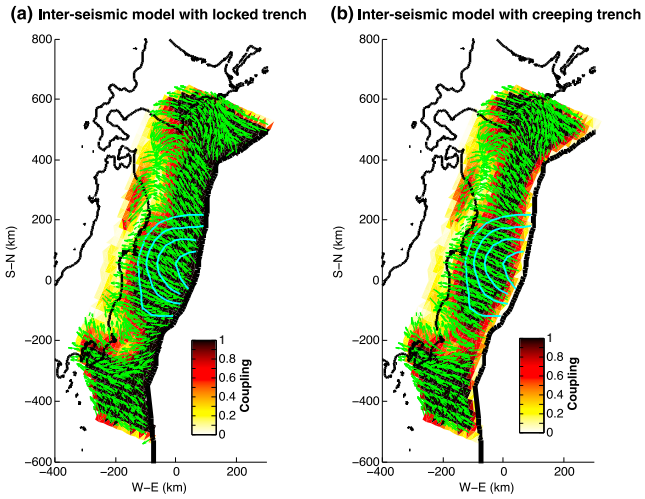

Figure A7. Coupling models obtained with no constraints on slip azimuth (free rake) for (a) a locked trench or (b) a creeping trench. The smoothing parameter is $\gamma = 10$. The blue slip contour lines correspond to our preferred coseismic model of Figure 6a.

A4. Rescaling of the Uncertainties

We have initially considered the nominal uncertainties on the horizontal and vertical GPS daily solutions of the GEONET network respectively to 2 mm and 10 mm. The value of χ_r^2 (greater than 1) for our preferred model suggests that the uncertainties needed to account for all sources of misfits are, in fact, larger. Our preferred coseismic and postseismic models obtained considering only the inland stations (Figure 15) yield $\chi_r^2 \approx 8.59$. This requires a rescaling factor of $\sqrt{\chi_r^2} \approx 2.93$ for the inland stations, leading to a posteriori estimated uncertainties of the order of 6 mm horizontally and 29 mm vertically.

A5. Postseismic-Only Model

Figure A12 shows a postseismic model obtained considering only the postseismic deformation field. This model is very close to the model of Figure 8a obtained simultaneously with the coseismic model of Figure 6a. This model was obtained considering a single component in the PCAIM decomposition and a smoothing factor of $\gamma = 3 \times 10^5$. The similarity of both models shows that the postseismic slip distribution is independent of the decomposition scheme. The advantage of the joint inversion for coseismic and postseismic slip is that it allows incorporating the sea bottom data in the analysis.

Appendix B: Resolution Tests

B1. Checkerboard Tests

Figures B1 and B2 present the results of a checkerboard test. An initial slip distribution consisting of a collection of circular asperities with unit slip is imposed and we test the ability of our model to recover this imposed pattern. Two asperity radius are considered: 60 km (Figure B1) and 80 km (Figure B2), as well as various values of the smoothing parameter: 10, 10^2, and 10^3. Note that those values are different from our best preferred values since this inversion is static and does not require any decomposition. To test the resolution of our model near the trench, the inversions were carried on considering the inland stations only. Inclusion of the offshore stations would increase the resolution near the trench. So we present here the worst case resolution.

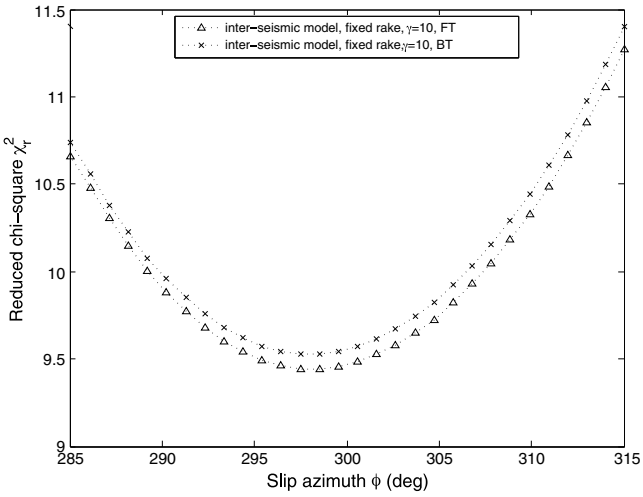

Figure A8. Reduced chi-square as a function of the slip azimuth ϕ for the interseismic models with locked or blocked trench.

Figures B1 and B2 show the recovered slip distribution for a smoothing parameter of 10, 10^2, or 10^3 (compared to the optimal value of 10 determined in our interseismic model). The larger the radius

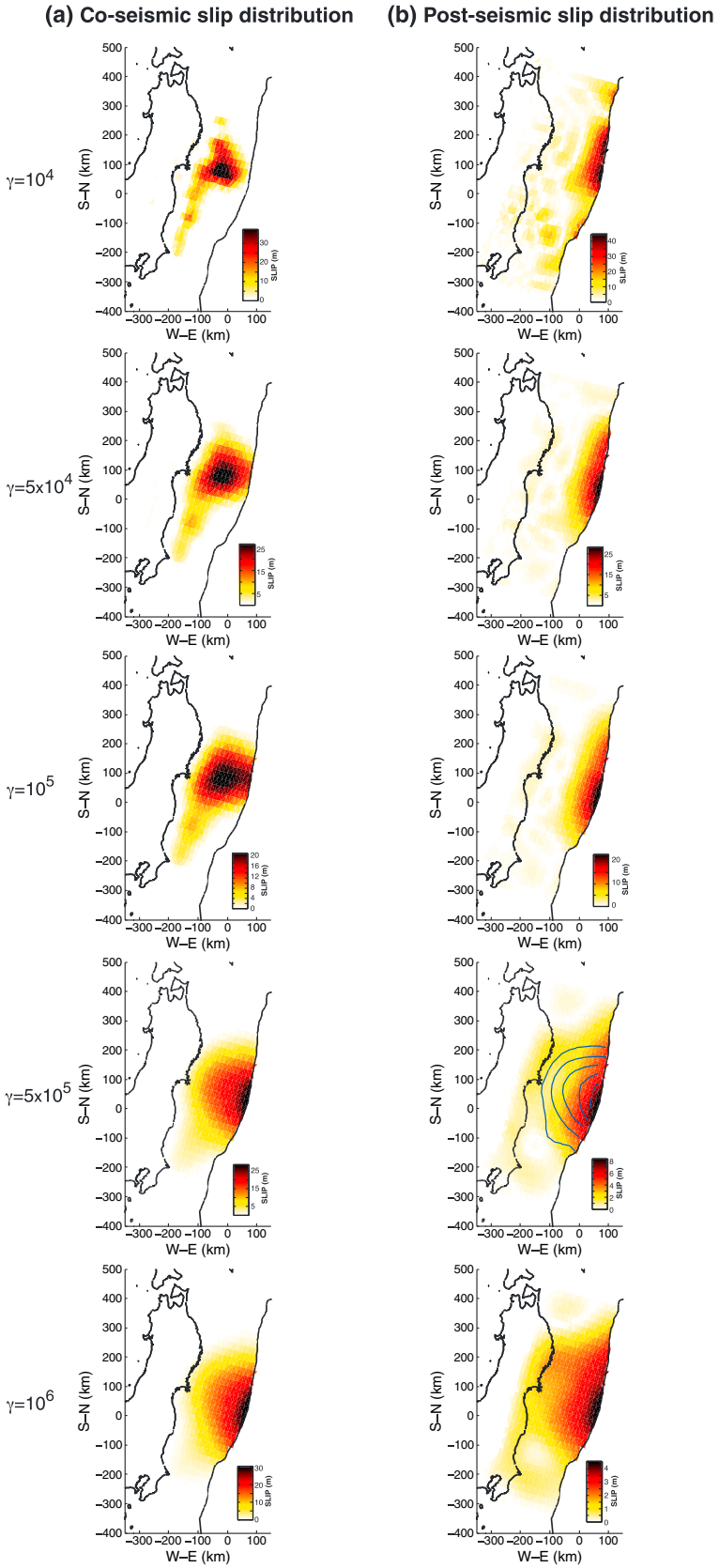

Figure A9. (a) Coseismic and (b) postseismic models for various values of the smoothing parameter ($\gamma = 10^4$, 5×10^4, 10^5, 5×10^5, and 10^6) with imposed slip azimuth (fixed rake) and free trench.

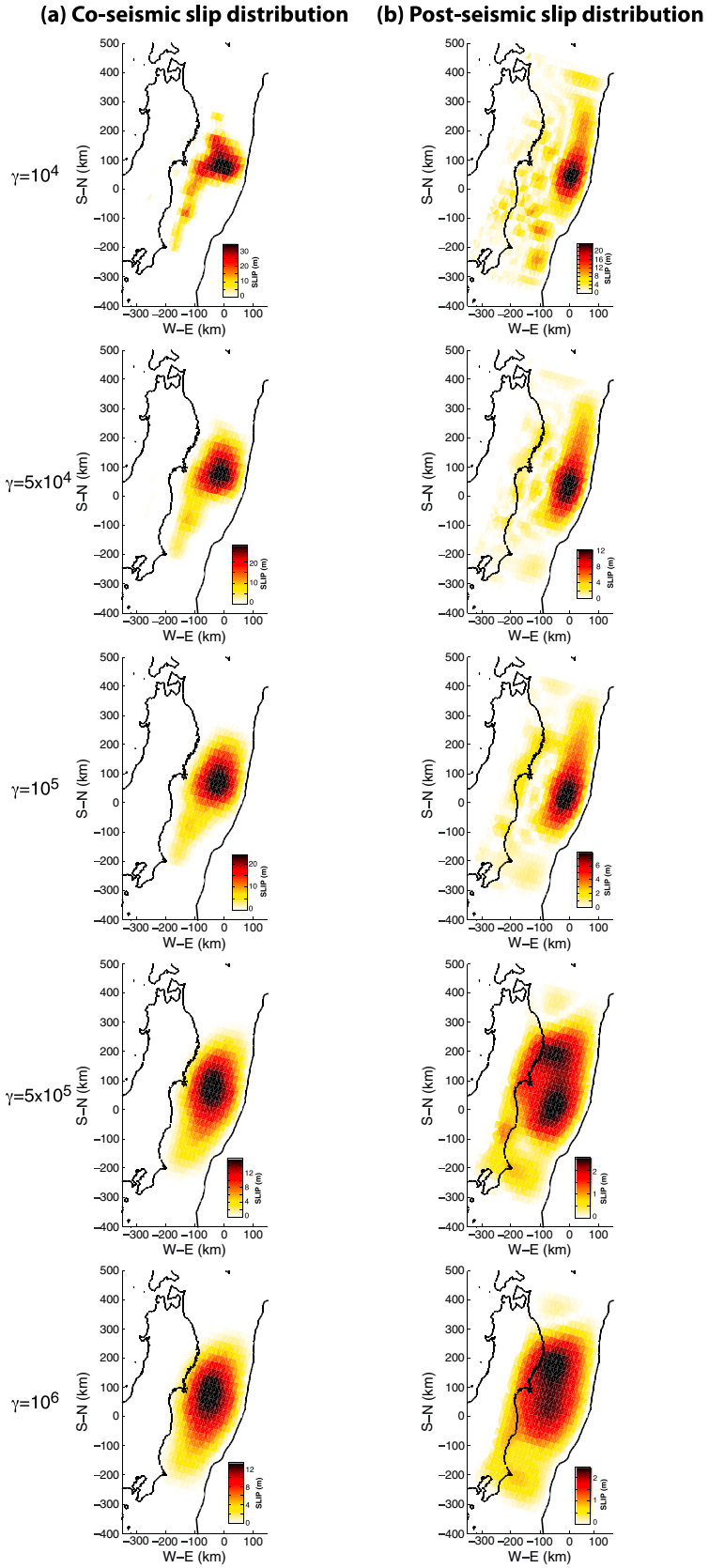

Figure A10. (a) Coseismic and (b) postseismic models for various values of the smoothing parameter ($\gamma = 10^4$, 5×10^4, 10^5, 5×10^5, and 10^6) with an imposed slip azimuth model (fixed rake) and blocked trench.

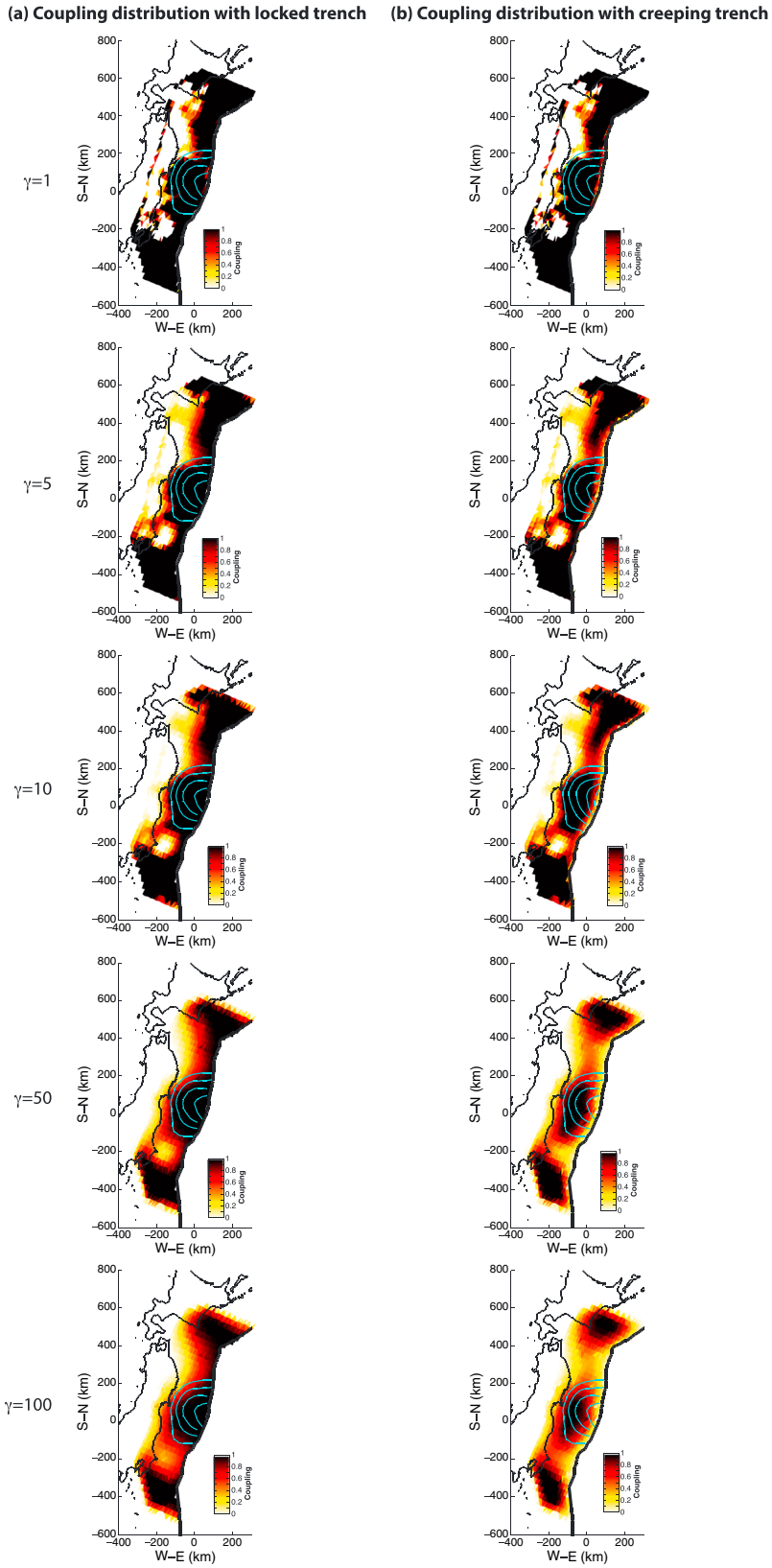

Figure A11. (a) Interseismic model for various values of the smoothing parameter (γ = 1, 5, 10, 50, and 100) considering a fixed slip azimuth of 292° with locked trench. The cyan contour lines correspond to our preferred coseismic slip model of Figure 6a. (b) Same for the model obtained assuming free creep at the trench.

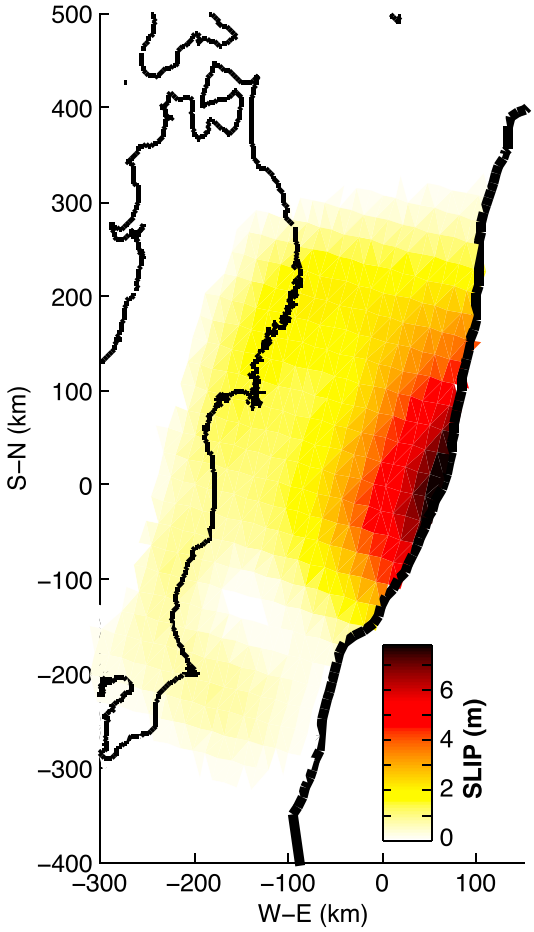

Figure A12. Cumulated postseismic slip over 279 days following the main shock determined considering only the postseismic deformation field. Only one free component is used in the PCAIM decomposition in this case. This model was obtained with slip left free at the trench, a slip azimuth constrained to $\phi = 112°$) and a smoothing parameter $\gamma = 3 \times 10^5$. Note the similarity with the postseismic model of Figure 8a obtained simultaneously with the coseismic slip distribution.

of the circles, the better it is recovered, but we note that for the range of smoothing parameters used here even the smaller asperities are reasonably well resolved in absence of noise on the measurements. The variable azimuth model (Figures B1 and B2, right) generates artificial variations in slip azimuth. The free trench model (Figures B1 and B2, left) shows a better ability to recover the imposed slip pattern than does the blocked trench model (Figures B1 and B2, middle), although the differences are moderate. Not surprisingly, the resolution decreases as the distance from the coast increases. The results of Figures B1 and B2 show that our model has a good spatial resolution all over the fault plane.

B2. Synthetic Resolution Tests

We present here some synthetic tests designed to examine the robustness of our results.

We start by building synthetic slip models for the coseismic and postseismic phase. We impose the two synthetic slip models to mimic our preferred models. They correspond to a uniform slip (14 m for the coseismic case and 6.3 m for the postseismic one) distributed over the blue contours of Figure B3 with moment-magnitude released comparable to our preferred models, namely, M_w9.0 for the coseismic case and M_w8.7 for the postseismic case. Note that the two imposed distributions overlap spatially as do the models determined from our inversions.

Using the Green functions used in our inversion, we build a data set of synthetic time series assuming the same fixed azimuth as in our preferred models ($\phi = 112°$SE). We used a smoothed version of the V_2 vector of Figure A2 to build our reference time series and add to the smooth time series a Gaussian noise with standard deviation corresponding to our initial assumption of the measurement uncertainties (2 mm horizontally and 10 mm vertically). We then decompose the synthetic time series and invert the slip distribution assuming the same values of the smoothing parameter ($\gamma = 5 \times 10^5$ as in our preferred models).

Figure B3 shows the coseismic (Figure B3a) and postseismic (Figure B3b) slip distributions inverted from the synthetic time series. A variable slip azimuth has been considered to evaluate the potential of the inversion process to recover the imposed azimuth. The smoothing parameter ($\gamma = 5 \times 10^5$) used is the same as the one of Figure 8.

The inverted slip distributions are similar to the imposed ones, both in terms of inverted moment-magnitude (M_w9.10 and M_w8.63 for the coseismic and postseismic cases) and spatial distribution. The predicted slip azimuth is mostly consistent with a uniform azimuth, although some small variations can be observed at the edges of the slip patches, suggesting that the variations in azimuth of our variable azimuth models might be in fact some artifacts of the inversion, further justifying our preference for models derived with a fixed slip azimuth. The recovered time series (see Figure B4) are in very good agreement with the initial synthetic ones with a reduced chi-square close to one (≈ 1.12) as it should be in this test.

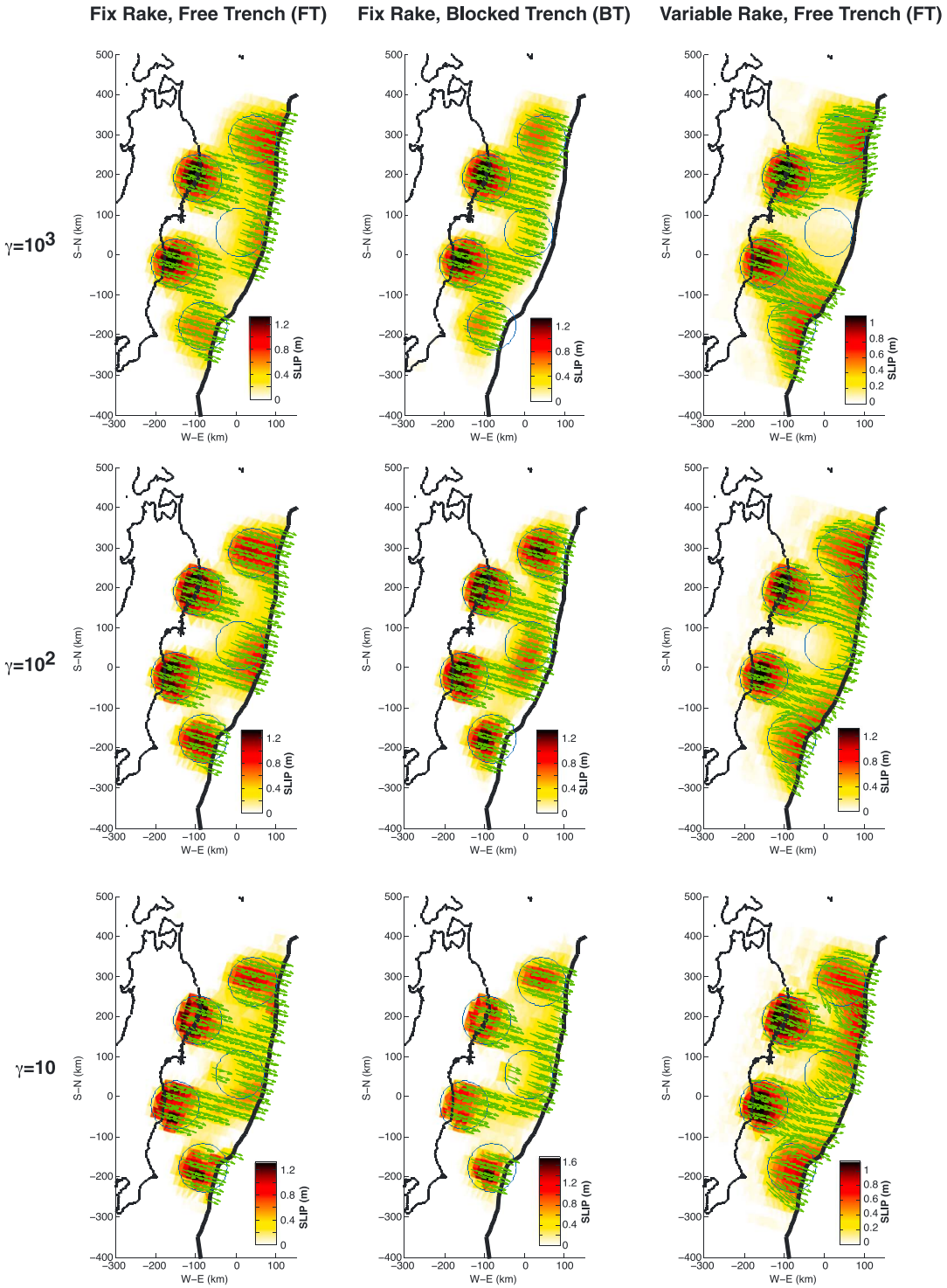

Figure B1. Resolution test for our coseismic and postseismic fault model considering a pattern of circular asperities of radius $R = 60$ km. For each value of the smoothing parameter $\gamma = 10$, 10^2, and 10^3, three different models are considered: (left) Fix rake model with free trench, (middle) fix rake model with blocked trench, and (right) variable rake with free trench. The green vectors show the slip azimuth along the fault.

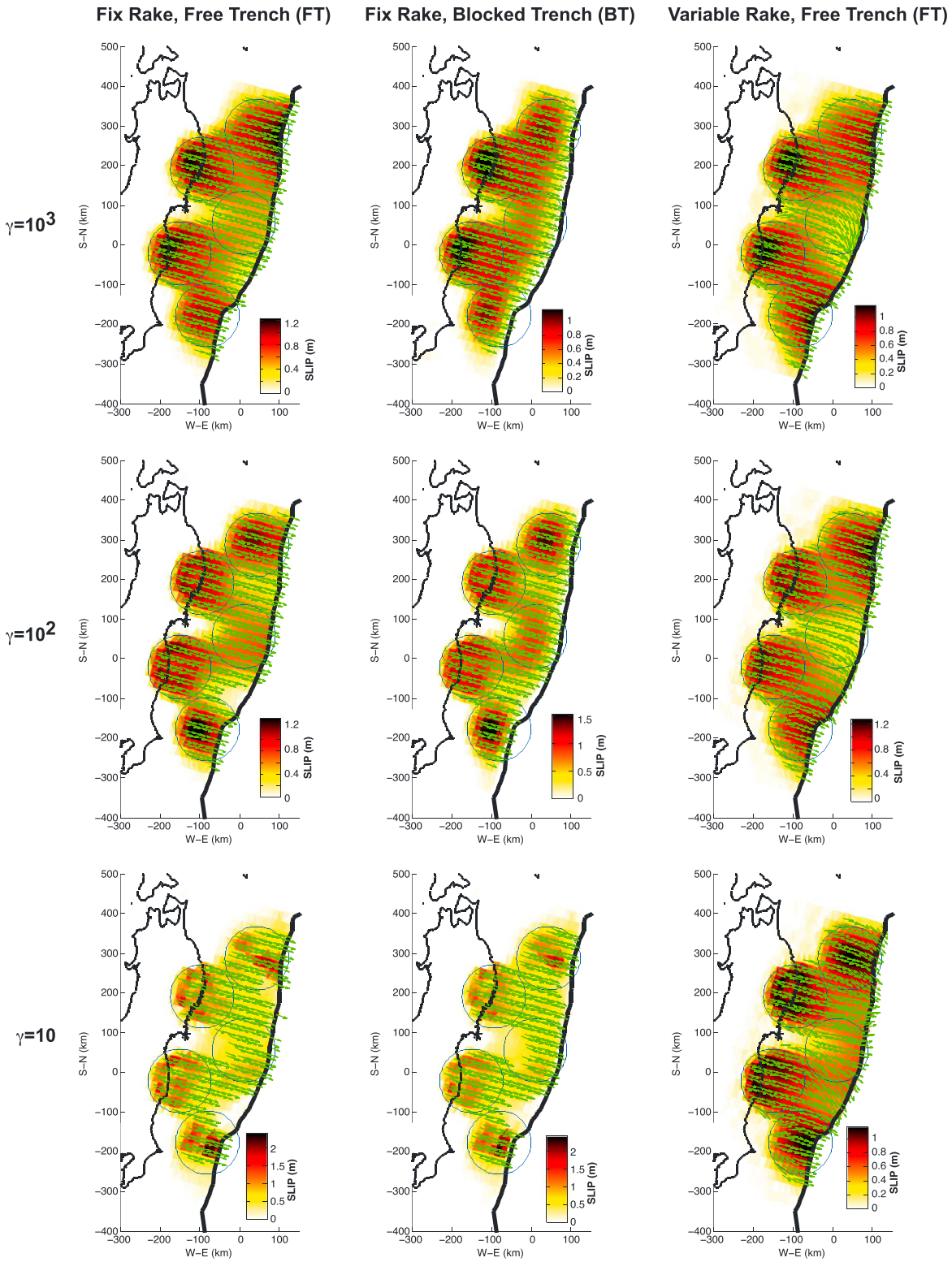

Figure B2. Same as Figure B1 for a radius of $R = 80$ km.

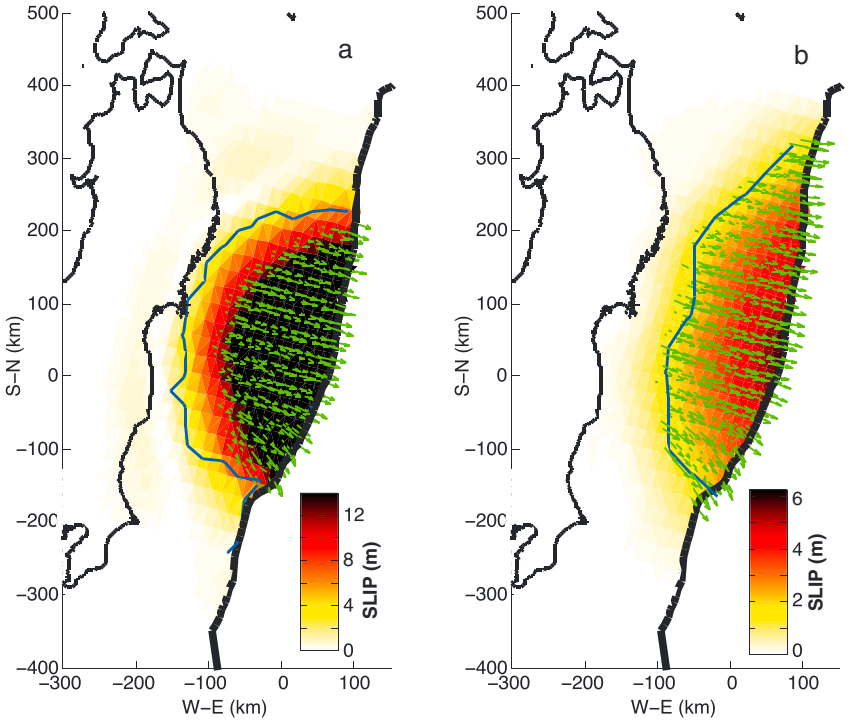

Figure B3. (a) Coseismic and (b) postseismic slip distribution obtained inverting a set of synthetic time series for a smoothing parameter of $\gamma = 5 \times 10^5$ as in our preferred models. The initial imposed models correspond to an uniform slip distributed within the blue contours and correspond to an imposed moment-magnitude of M_w9.0 for the coseismic case and M_w8.7 for the postseismic case. In this inversion, both the inland and offshore data are included.

Figure B5 shows the results of a similar test carried on considering only the inland stations. The smoothing parameter ($\gamma = 3 \times 10^5$) used is the same as the one of Figure 8. Figure B5 is very similar to Figure B3 as Figure A12 is close to Figure 8. The inverted slip distributions are similar to the imposed ones, both in terms of inverted moment-magnitude (M_w9.07 and M_w8.61 for the coseismic and postseismic cases) and spatial distribution. The fit to the time series is good (not shown here) with a reduced chi-square of the order of 1.4.

This synthetic resolution test shows that our model is able to properly retrieve an imposed slip distribution similar to our preferred coseismic and postseismic models without generating significant artifacts. This is true when considering the inland stations only. The slip distribution, amplitude, and seismic moment are well resolved for both phases and so is the imposed temporal evolution. The imposed overlap between the initial coseismic and postseismic distributions is also properly resolved. The main difference between our recovered models and the initial ones is that our inverted slip distributions show smooth slip gradients due to the smoothness operator (the Laplacian) used in the inversion, instead of a uniform slip as initially imposed. But this is an intrinsic drawback of any inversion where smoothing is mostly introduced to reduce the overdetermination of the system.

Appendix C: The Iterative Decomposition Method

C1. Principle

Our goal is to minimize the chi-square given by

$$\chi^2 = \sum_{i=1}^{N} \sum_{j=1}^{M} w_{ij}(X_{ij} - U_i V_j - m_i)^2, \tag{C1}$$

where X_{ij} is the data matrix of size $N \times M$, N being the number of stations, M the number of epochs, and w_{ij} is a weight function, typically $w_{ij} = \frac{1}{\sigma_{ij}^2}$. We look for an algorithm that derives U_i, V_j, and the mean vector m_i with $i = 1, N$ and $j = 1, M$.

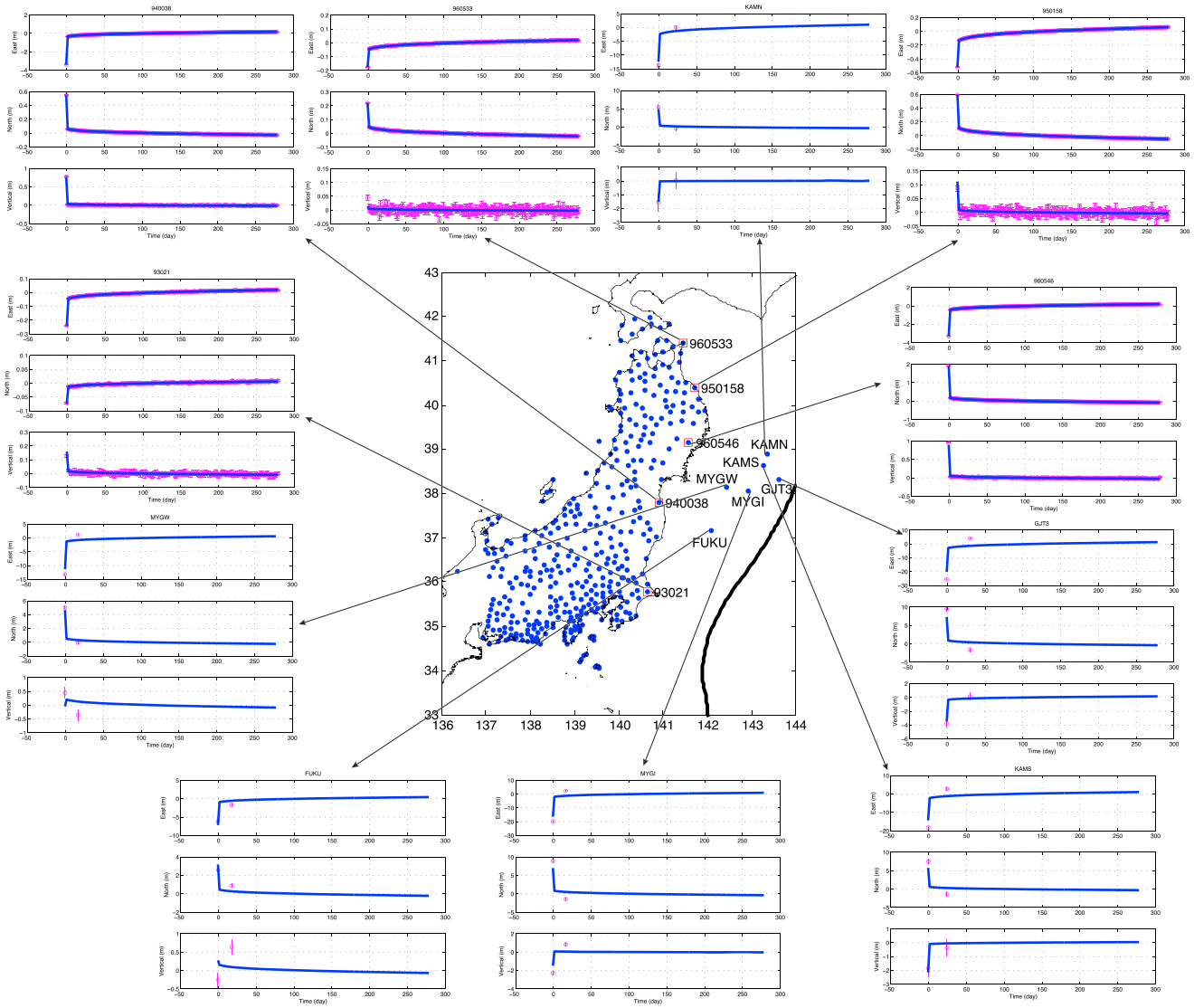

Figure B4. Time series at selected stations for our slip model of Figure B3, obtained inverting some synthetic data. The fit to the data is very good, demonstrating that our model is able to retrieve the initial imposed model.

In the standard PCAIM algorithm, the vectors U, V, and m are determined simultaneously using a conjugate gradient method (see the PCAIM manual, http://www.tectonics.caltech.edu/resources/pcaim/). The advantage of this standard approach is that it insures the orthogonality of the eigenvectors, but the drawback is a large computational time and memory usage. We present here a simplified iterative method that allows for a faster determination of the U and the V eigenvectors. This method is similar to the iterative decomposition of *Lin et al.* [2010] and is extended to compute not only the U and the V but also the mean vector m.

We start by noting that the optimal vectors U, V, and m can be found solving for $\frac{\partial \chi^2}{\partial m_k} = 0$, $\frac{\partial \chi^2}{\partial U_k} = 0$, and $\frac{\partial \chi^2}{\partial V_k} = 0$.

Considering the mean vector, we get

$$\frac{\partial \chi^2}{\partial m_k} = \sum_{j=1}^{M} w_{kj}(X_{kj} - U_k V_j - m_k) = 0, \tag{C2}$$

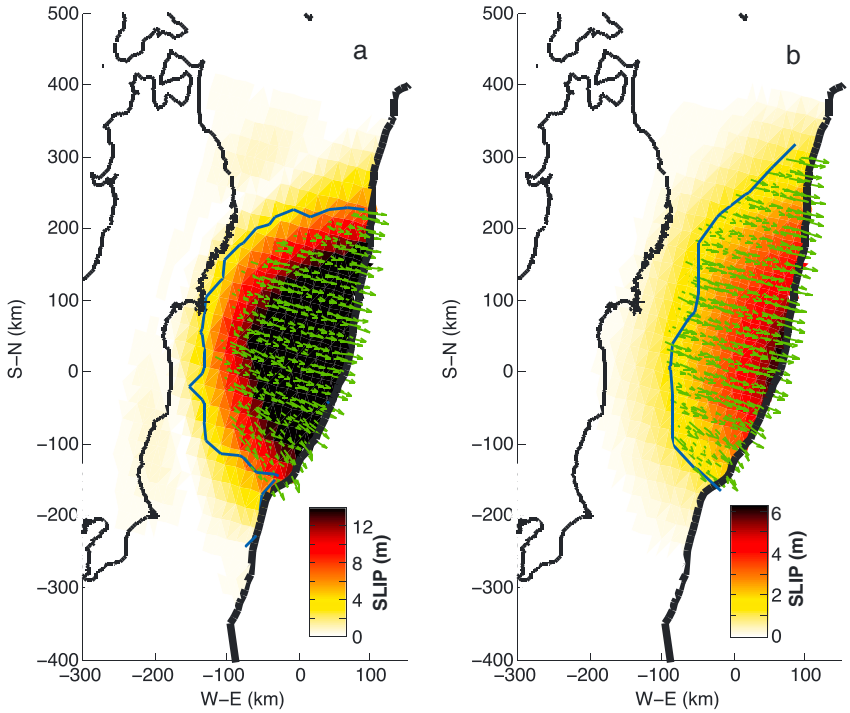

Figure B5. Same as Figure B3 inverting only the inland stations. The smoothing parameter is $\gamma = 3 \times 10^5$ as in the model of Figure A12.

which leads to

$$m_k = \frac{\sum_{j=1}^{M} w_{kj}(X_{kj} - U_k V_j)}{\sum_{j=1}^{M} w_{kj}}. \tag{C3}$$

Considering the vector U, we obtain

$$\frac{\partial \chi^2}{\partial U_k} = \sum_{j=1}^{M} w_{kj} V_j (X_{kj} - U_k V_j - m_k) = 0, \tag{C4}$$

yielding

$$U_k = \frac{\sum_{j=1}^{M} w_{kj} V_j (X_{kj} - m_k)}{\sum_{j=1}^{M} w_{kj} V_j^2} \tag{C5}$$

Considering the vector V, we obtain

$$\frac{\partial \chi^2}{\partial V_k} = \sum_{i=1}^{N} w_{ik} U_i (X_{ik} - U_i V_k - m_i) = 0, \tag{C6}$$

leading to

$$V_k = \frac{\sum_{i=1}^{N} w_{ik} U_i (X_{ik} - m_i)}{\sum_{i=1}^{N} w_{ik} U_i^2}. \tag{C7}$$

C2. Description of the Algorithm

The analytical expressions from equations (C3), (C5), and (C7) can be used to solve iteratively for the decomposition.

We start with an initial guess $[m(0), U(0), V(0)]$ and get the next triplet $[m(1), U(1), V(1)]$ with the use of equations (C3), (C5), and (C7). This is done iteratively until the difference between the triplet $[m(l), U(l), V(l)]$

for the lth iteration and the triplet $[m(l+1), U(l+1), V(l+1)]$ for iteration $l+1$ is lower than a given precision. Note that a good starting point for the initial triplet $[m(0), U(0), V(0)]$ is $m(0) = \text{mean}(X, 2)$ (mean of the data matrix averaged over time), while $U(0) = S_{\text{svd}} \times U_{\text{svd}}$ and $V(0) = V_{\text{svd}}$ where $[U_{\text{svd}}, S_{\text{svd}}, V_{\text{svd}}] = \text{svd}(X, 1)$ is the result of the standard Singular Value Decomposition (SVD) decomposition assuming one component.

After convergence is achieved, we obtain the triplet $[m_1, U_1, V_1]$ corresponding to the first component. To find the next component, we apply the same procedure considering the residuals of the decomposition, namely, $X_2 = X_1 - U_1 V_1 - m1$, where $X_1 = X$ is the original data matrix. Using the iterative procedure described above, one gets the triplet $[m_2, U_2, V_2]$ for the second component. This is done up to the number of components required.

In order to recover the classical SVD decomposition, we introduce for the component k the quantity $S_k = \|U_k\|\|V_k\|$ and then normalize the vectors U_k and V_k by their respective norm to obtain unit vectors. The matrix S of the SVD decomposition is obtained considering the diagonal matrix of size $N \times M$ which diagonal is made of the S_ks.

C3. Correcting for a Step Due to an Imposed Component of V

The algorithm described above easily accounts for an imposed component of V.

Suppose that V_1 is imposed. Then it is straightforward to obtain U_1 and m_1 using only equations (C3) and (C5). The subsequent components are derived using the procedure described in section C2. A problem often arising is that a discontinuity in V_1 will induce discontinuities in the other V_k, $k > 1$. We present here a simple method to remove those discontinuities. This method is analogous to the one used in the standard PCAIM decomposition to correct from discontinuities due to an imposed V vector.

We start by noting that

$$USV^T = \sum_{i=1}^{N_{\text{comp}}} (U_i S_i V_i^T), \tag{C8}$$

where N_{comp} is the number of components and $(\ldots)^T$ means matrix transpose. Our goal being to separate the influence of V_1, we write equation (C8) as

$$USV^T = \sum_{i=1}^{N_{\text{comp}}} \left(U_i S_i V_i^T - c_i U_i S_i V_1^T + c_i U_i S_i V_1^T \right), \tag{C9}$$

where the c_is are constant to be found. Equation (C9) transforms into

$$USV^T = \left(\sum_{i=1}^{N_{\text{comp}}} c_i U_i S_i \right) V_1^T + \sum_{i=2}^{N_{\text{comp}}} U_i S_i \left(V_i^T - c_i V_1^T \right), \tag{C10}$$

where we have imposed $c_1 = 1$.

Equation (C10) shows that we can choose new eigenvectors such as

$$U_1^{\text{new}} = \left(\sum_{i=1}^{N_{\text{comp}}} c_i U_i^{\text{old}} S_i^{\text{old}} \right), V_1^{\text{new}} = V_1^{\text{old}}, S_1^{\text{new}} = \left\| U_1^{\text{new}} \right\| \tag{C11}$$

and

$$V_i^{\text{new}} = V_i^{\text{old}} - c_i V_1^{\text{old}}, U_i^{\text{new}} = U_i^{\text{old}}, S_i^{\text{new}} = S_i^{\text{old}}, \; i = 2, N_{\text{comp}}. \tag{C12}$$

With those new vectors, equation (C10) becomes

$$USV^T = U_1^{\text{new}} (V_1^{\text{new}})^T + \sum_{i=2}^{N_{\text{comp}}} U_i^{\text{new}} S_i^{\text{new}} (V_i^{\text{new}})^T. \tag{C13}$$

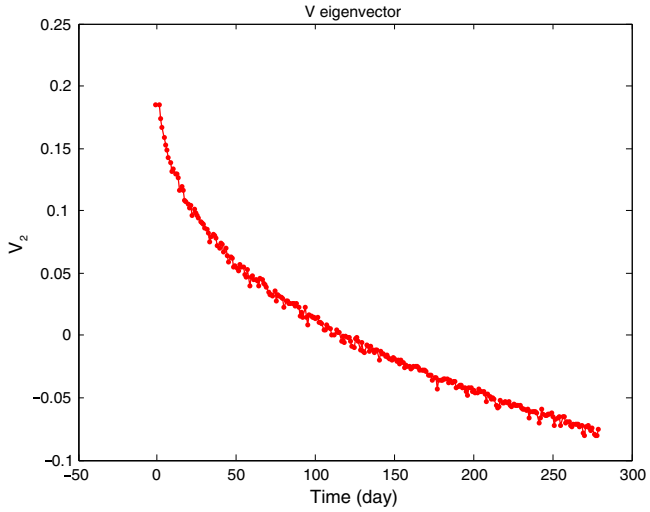

Figure C1. Time function associated to the second component of the iterative decomposition ($\mathbf{V_2}$). A Heaviside function for the vector ($\mathbf{V_1}$) is imposed to mimic the coseismic step.

Let us consider two consecutive epochs corresponding to index s and $s+1$ of the time vector V. According to equation (C12), the old and new V_i vectors are related through

$$V_i^{\text{new}}(s+1) - V_i^{\text{new}}(s) = V_i^{\text{old}}(s+1) - V_i^{\text{old}}(s) - c_i \left[V_1^{\text{old}}(s+1) - V_1^{\text{old}}(s)\right]. \tag{C14}$$

Imagine that there is a discontinuity at the index s in the imposed vector V_1 so that $V_1^{\text{old}}(s+1) \neq V_1^{\text{old}}(s)$. If we want this discontinuity to disappear from V_i^{new}, then one can solve for (C14) assuming that $V_i^{\text{new}}(s+1) = V_i^{\text{new}}(s)$ leading to

$$c_i = \frac{V_i^{\text{old}}(s+1) - V_i^{\text{old}}(s)}{V_1^{\text{old}}(s+1) - V_1^{\text{old}}(s)},\ i = 2, N_{\text{comp}} \tag{C15}$$

Equation (C15) allows the determination of the coefficient c_i, $i = 2, N_{\text{comp}}$ to avoid any discontinuities in the imposed V_1 vector. Using equations (C11) and (C12), remember that $c_1 = 1$ allows the construction of the new eigenvectors. Note that $c_1 = 1$ is also true in equation (C15) for $i = 1$ so that it may be generalized to any component.

C4. Simplified Variance

In the PCAIM package, the covariance matrix C_u of U (see section 3.2) is computed using its exact mathematical formulation in the least squares problem [*Tarantola*, 2005, equation (3.41)]. This calculation is time consuming, and we present here an alternative formulation that is much faster to compute numerically. We simplified the weight function $w_{ij} = \frac{1}{\sigma_{ij}^2}$ into $w_i = \frac{1}{\text{MEAN}(\sigma_{i:}^2)}$, meaning that we weight the residuals between the model prediction and the data by the mean uncertainty at station i. Other choices can be assumed (like taking the median or the max of the uncertainty at a given station), but they usually lead to the same results if the measurements error do not vary much in time.

Since $w_i = \frac{1}{\text{MEAN}(\sigma_{i:}^2)}$, the matrix C_u' in equation (6) yields $C_u' = \text{diag}\left(\frac{1}{\text{MEAN}(\sigma)}\right)$ so that

$$C_u = \text{diag}(\text{MEAN}(\sigma^2)) \tag{C16}$$

after use of equation (7).

C5. Results

Figure C1 shows the second V eigenvector that looks similar to the prediction of the standard PCAIM decomposition (see Figure A2). This is not surprising, noting that the first component has been imposed to a Heaviside function both for the iterative and standard decomposition.

Figure C2 show the coseismic (Figure C2a) and postseismic distribution (Figure C2b) using the iterative decomposition with simplified variance (see C16) and considering various values of the smoothing parameter, namely, $\gamma = 5 \times 10^3$ and 10^4. The results of the iterative decomposition are consistent with the inversion carried on using the standard decomposition and variance as may be seen comparing Figures C2 with our preferred model of Figures 6 and 8 although some differences might be observed. For instance, the rougher model of Figure C2 splits the zone of shallow afterslip in two subpatches, the northern one corresponding to the location of the 1896 tsunami earthquake. When smoother models are considered, a unique shallow patch of afterslip is observed (Figure C2).

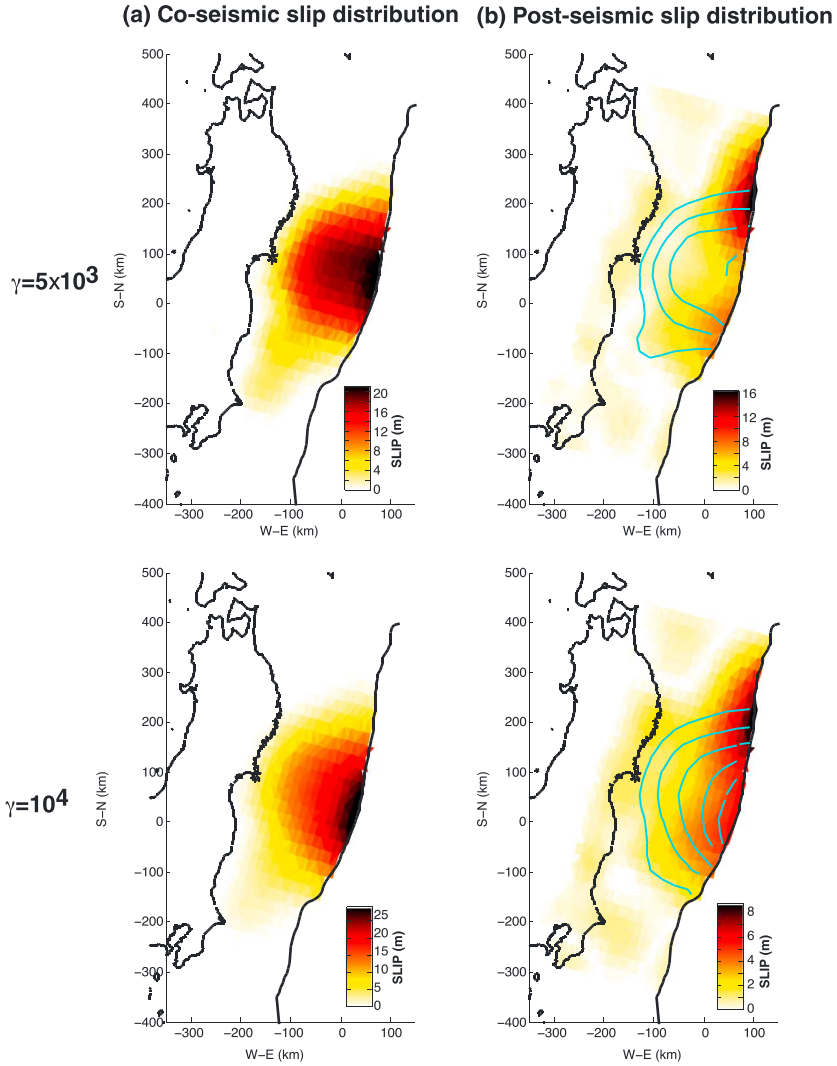

Figure C2. (a) Coseismic and (b) postseismic distribution considering the iterative decomposition and the simplified covariance matrix of section C4, an imposed slip azimuth ($\phi = 112°$), and a smoothing parameter of $\gamma = 5 \times 10^3$ and 10^4.

Acknowledgments
We thank Michiko Onogaki for providing the GEONET data, Brendan Meade for providing the interseismic velocities of *Loveless and Meade* [2010], Shinzaburo Ozawa, Mohamed Chlieh, Hiroo Kanamori, Michael Bevis, Erwan Pathier, and Michel Bouchon for useful discussions. We thank Tom Parson, Marcos Moreno and an anonymous reviewer for their constructive reviews that really helped improving the manuscript. Some of the figures of this paper have been done using GMT (http://gmt.soest.hawaii.edu/). This is Tectonics Observatory contribution #260.

References

Ader, T., et al. (2012), Convergence rate across the Nepal Himalaya and interseismic coupling on the main Himalayan thrust: Implications for seismic hazard, *J. Geophys. Res.*, *117*, B04403, doi:10.1029/2011JB009071.

Avouac, J.-P. (2011), The lessons of Tohoku-Oki, *Nature*, *475*, 300, doi:10.1038/nature10265.

Burgmann, R., M. G. Kogan, G. M. Steblov, G. Hilley, V. E. Levin, and E. Apel (2005), Interseismic coupling and asperity distribution along the Kamchatka subduction zone, *J. Geophys. Res.*, *110*, B07405, doi:10.1020/2005JB003648.

Byrne, D. E., D. M. Davis, and L. R. Sykes (1988), Loci and maximum size of thrust earthquakes and the mechanics of the shallow region of subduction zones, *Tectonics*, *7*, 833–857.

Chester, F. M., et al. (2013), Structure and composition of the plate-boundary slip zone for the 2011 Tohoku-Oki earthquake, *Science*, *342*(6163), 1208–1211.

Cubas, N., J. P. Avouac, Y. M. Leroy, and A. Pons (2013), Low friction along the high slip patch of the 2011 Mw 9.0 Tohoku-Oki earthquake required from the wedge structure and extensional splay faults, *Geophys. Res. Lett.*, *40*, 4231–4237, doi:10.1002/grl.50682.

den Hartog, S. A. M., C. J. Peach, D. A. M. de Winter, C. J. Spiers, and T. Shimamoto (2012a), Frictional properties of megathrust fault gouges at low sliding velocities: New data on effects of normal stress and temperature, *J. Struct. Geol.*, *38*, 156–171.

den Hartog, S. A. M., A. R. Niemeijer, and C. J. Spiers (2012b), New constraints on megathrust slip stability under subduction zone p-t conditions, *Earth Planet. Sci. Lett.*, *353*, 240–252.

Dublanchet, P., P. Bernard, and P. Favreau (2013), Interactions and triggering in a 3-D rate-and-state asperity model, *J. Geophys. Res. Solid Earth*, *118*, 2225–2245, doi:10.1002/jgrb.50187.

Evans, E. L., and B. J. Meade (2012), Geodetic imaging of coseismic slip and postseismic afterslip: Sparsity promoting methods applied to the great Tohoku earthquake, *Geophys. Res. Lett.*, *39*, L11314, doi:10.1029/2012GL051990.

Freymueller, J. T., and J. Beavan (1999), Absence of strain accumulation in the western Shumagin segment of the Alaska subduction zone, *Geophys. Res. Lett.*, *26*, 3233–3236.

Fujiwara, T., S. Kodaira, T. No, Y. Kaiho, N. Takahashi, and Y. Kaneda (2011), The 2011 Tohoku-Oki earthquake: Displacement reaching the trench axis, *Science*, *334*, 1240, doi:10.1126/science.1211554.

Fukuda, J., A. Kato, N. Kato, and Y. Aoki (2013), Are the frictional properties of creeping faults persistent? Evidence from rapid afterslip following the 2011 Tohoku-Oki earthquake, *Geophys. Res. Lett.*, *40*, 3613–3617, doi:10.1002/grl.50713.

Fulton, P. M., et al. (2013), Low coseismic friction on the Tohoku-Oki fault determined from temperature measurements, *Science*, *342*(6163), 1214–1217.

Hansen, P. C. (1992), Analysis of discrete ill-posed problems by means of the L-curve, *SIAM Rev.*, *34*(4), 561–580.

Hansen, P. C., and D. P. O'Leary (1993), The use of the L-curve in the regularization of discrete ill-posed problems, *SIAM J. Sci. Comput.*, *14*, 1487–1503.

Harris, R. A., and P. Segall (1987), Detection of a locked zone at depth on the Parkfield, California segment of the San Andreas fault, *J. Geophys. Res.*, *92*, 7945–7962.

Hasegawa, A., K. Yoshida, and T. Okada (2011), Nearly complete stress drop in the 2011 m_w9.0 off the Pacific coast of Tohoku earthquake, *Earth Planets Space*, *63*, 703–707, doi:10.5047/eps.2011.06.007.

Hashimoto, C., A. Noda, T. Sagiya, and M. Matsuura (2009), Interplate seismogenic zones along the Kuril-Japan trench inferred from GPS data inversion, *Nat. Geosci.*, *2*, 141–144, doi:10.1038/ngeo421.

Hayes, G. P., D. J. Wald, and R. L. Johnson (2012), Slab1.0: A three-dimensional model of global subduction zone geometries, *J. Geophys. Res.*, *117*, B01302, doi:10.1029/2011JB008524.

Heki, K., and Y. Tamura (1997), Short term afterslip in the 1994 Sanriku-Haruka-Oki earthquake, *Geophys. Res. Lett.*, *24*, 3285–3288.

Hsu, Y. J., J. P. Avouac, S. B. Yu, C. H. Chang, Y. M. Wu, and J. Woessner (2006a), Spatio-temporal slip, and stress level on the faults within the Western Foothills of Taiwan: Implications for fault frictional properties, *Pure Appl. Geophys.*, *166*(10–11), 1853–1884.

Hsu, Y.-J., M. Simons, J.-P. Avouac, J. Galtezka, K. Sieh, M. Chlieh, D. Natawidjaja, L. Prawirodirdjo, and Y. Bock (2006b), Frictional afterslip following the 2005 Nias-Simeulue earthquake, Sumatra, *Science*, *312*, 1921–1926.

Hsu, Y.-J., M. Simons, C. Williams, and E. Casarotti (2011), Three dimensional FEM derived elastic Green's functions for the coseismic deformation of the 2005 M_w 8.7 Nias Simeulue, Sumatra earthquake, *Geochem. Geophys. Geosyst.*, *12*, Q07013, doi:10.1029/2011GC003553.

Hyndman, R. D., M. Yamano, and D. A. Oleskevich (1997), The seismogenic zone of subduction thrust faults, *Island Arc*, *6*, 244–260, doi:10.1111/j.1440-1738.1997.tb00175.x.

Ide, S., A. Baltay, and G. C. Beroza (2011), Shallow dynamic overshoot and energetic deep rupture in the 2011 M_w9.0 Tohoku-Oki earthquake, *Science*, *6036*, 1426–1429.

Iinuma, T., et al. (2012), Coseismic slip distribution of the 2011 off the Pacific coast of Tohoku earthquake (M9.0) refined by means of seafloor geodetic data, *J. Geophys. Res.*, *117*, B07409, doi:10.1029/2012JB009186.

Ikari, M. J., and D. M. Saffer (1998), Comparison of frictional strength and velocity dependence between fault zones in the Nankai accretionary complex, *Geochem. Geophys. Geosyst.*, *12*, Q0AD11, doi:10.1029/2010GC003442.

Ito, Y., T. Tsuji, Y. Osada, M. Kido, D. Inazu, Y. Hayashi, H. Tsushima, R. Hino, and H. Fujimoto (2011), Frontal wedge deformation near the source region of the 2011 Tohoku-Oki earthquake, *Geophys. Res. Lett.*, *38*, L00G05, doi:10.1029/2011GL048355.

Johnson, K. M., and P. Segall (2004), Viscoelastic earthquake cycle models with deep stress-driven creep along the San Andreas fault system, *J. Geophys. Res.*, *109*, B10403, doi:10.1029/2004JB003096.

Johnson, K. M., J. Fukuda, and P. Segall (2012), Challenging the rate-state asperity model: Afterslip following the 2011 M9 Tohoku-Oki, Japan, earthquake, *Geophys. Res. Lett.*, *39*, L20302, doi:10.1029/2012GL052901.

Kanamori, H., and D. L. Anderson (1975), Theoretical basis of some empirical relations in seismology, *Bull. Seismol. Soc. Am.*, *65*, 1073–1095.

Kanamori, H., and K. C. McNally (1982), Variable rupture mode of the subduction zone along the Ecuador-Colombia coast, *Bull. Seismol. Soc. Am.*, *72*(4), 1241–1253.

Kanda, R. V. S., and M. Simons (2010), An elastic plate model for interseismic deformation in subduction zones, *J. Geophys. Res.*, *115*, B03405, doi:10.1029/2009JB006611.

Kaneko, Y., J. P. Avouac, and N. Lapusta (2010), Towards inferring earthquake patterns from geodetic observations of interseismic coupling, *Nat. Geosci.*, *3*, 363–369, doi:10.1038/ngeo843.

Kato, A., and T. Igarashi (2012), Regional extent of the large coseismic slip zone of the 2011 M_w 9.0 Tohoku-Oki earthquake delineated by on-fault aftershocks, *Geophys. Res. Lett.*, *39*, L15301, doi:10.1029/2012GL052220.

Khazaradze, G., K. Wang, J. Klotz, Y. Hu, and J. He (2002), Prolonged post-seismic deformation of the 1960 great Chile earthquake and implications for mantle rheology, *Geophys. Res. Lett.*, *29*(22), 2050, doi:10.1029/2002GL015986.

Kido, M., Y. Osada, H. Fujimoto, R. Hino, and Y. Ito (2011), Trench-normal variation in observed seafloor displacements associated with the 2011 Tohoku-Oki earthquake, *Geophys. Res. Lett.*, *38*, L24303, doi:10.1029/2011GL050057.

Konca, A. O., et al. (2008), Partial rupture of a locked patch of the sumatra megathrust during the 2007 earthquake sequence, *Nature*, *456*, 631–635.

Kositsky, A., and J. P. Avouac (2010), Inverting geodetic time series with a principal component analysis-based inversion method, *J. Geophys. Res.*, *115*, B03401, doi:10.1029/2009JB006535.

Lay, T., H. Kanamori, and L. Ruff (1982), The asperity model and the nature of large subduction zone earthquakes, Earthquake Pred. Res., 3–71.

Lay, T., C. J. Ammon, H. Kanamori, M. J. Kim, and L. Xue (2011), Outer trench-slope faulting and the 2011 M_w 9.0 off the Pacific coast of Tohoku earthquake, *Earth Planets Space*, *63*, 713–718, doi:10.5047/eps.2011.05.006.

Lin, Y. N. N., A. P. Kositsky, and J. P. Avouac (2010), PCAIM joint inversion of insar and ground-based geodetic time series: Application to monitoring magmatic inflation beneath the Long Valley Caldera, *Geophys. Res. Lett.*, *37*, L23301, doi:10.1029/2010GL045769.

Lin, Y.-N. N., et al. (2013), Coseismic and postseismic slip associated with the 2010 Maule earthquake, Chile: Characterizing the Arauco Peninsula barrier effect, *J. Geophys. Res. Solid Earth*, *118*, 3142–3159, doi:10.1002/jgrb.50207.

Lohman, R. B. (2004), The inversion of geodetic data for earthquake parameters, PhD thesis, California Institute of Technology.

Loveless, J. P., and B. J. Meade (2010), Geodetic imaging of plate motions, slip rates, and partitioning of deformation in Japan, *J. Geophys. Res.*, *115*, B02410, doi:10.1029/2008JB006248.

Loveless, J. P., and B. J. Meade (2011), Spatial correlation of interseismic coupling and coseismic rupture extent of the 2011 $m_w = 9.0$ Tohoku-oki earthquake, *Geophys. Res. Lett.*, *38*, L17306, doi:10.1029/2011GL048561.

Marone, C. (1998), Laboratory-derived friction laws and their application to seismic faulting, *Annu. Rev. Earth Planet. Sci.*, *26*, 643–696.

Marone, C. J., C. H. Scholz, and R. Bilham (1991), On the mechanics of earthquake afterslip, *J. Geophys. Res.*, *96*, 8441–8452.

Matsumoto, Y., T. Ishikawa, M. Fujita, M. Sato, H. Saito, M. Mochizuki, T. Yabuki, and A. Asada (2008), Weak interplate coupling beneath the subduction zone off Fukushima, Ne Japan, inferred from GPS/acoustic seafloor geodetic observation, *Earth Planets Space*, *60*, e9–e12.

Matsu'ura, T., A. Furusawa, and H. Saomoto (2009), Long-term and short-term vertical velocity profiles across the forearc in the NE Japan subduction zone, *Quat. Res.*, *71*(2), 227–238.
Melbourne, T. I., F. H. Webb, J. M. Stock, and C. Reigber (2002), Rapid postseismic transients in subduction zones from continuous GPS, *J. Geophys. Res.*, *107*(B10), 2241, doi:10.1029/2001JB000555.
Meng, L. S., A. Inbal, and J. P. Ampuero (2011), A window into the complexity of the dynamic rupture of the 2011 M_w9 Tohoku-Oki earthquake, *Geophys. Res. Lett.*, *38*, L00G07, doi:10.1029/2011GL048118.
Minoura, K., F. Imamura, D. Sugawara, Y. Kono, and T. Iwashita (2001), The 869 Jogan tsunami deposit and recurrence interval of large scale tsunami on the Pacific coast of Northeast Japan, *J. Nat. Disaster Sc.*, *23*(2), 83–88.
Miyazaki, S., P. Segall, J. Fukuda, and T. Kato (2004), Space time distribution afterslip following the 2003 Tokachi-Oki earthquake: Implications for variations in fault zone frictional properties, *Geophys. Res. Lett.*, *31*, L06623, doi:10.1029/2003GL019410.
Miyazaki, S., J. J. McGuire, and P. Segall (2011), Seismic and aseismic fault slip before and during the 2011 off the Pacific coast of Tohoku earthquake, *Earth Planets Space*, *63*, 637–642, doi:10.5047/eps.2011.07.001.
Moreno, M. S., J. Bolte, J. Klotz, and D. Melnick (2009), Impact of megathrust geometry on inversion of coseismic slip from geodetic data: Application to the 1960 Chile earthquake, *Geophys. Res. Lett.*, *36*, L16310, doi:10.1029/2009GL039276.
Nakagawa, H. (2009), Development and validation of Geonet new analysis strategy (version 4) [in Japanese], *J. Geog. Surv. Inst.*, *118*, 1–8.
Niemeijer, A. R., and C. J. Spiers (2009), Velocity dependence of strength and healing behaviour in simulated phyllosilicate-bearing fault gouge, *Tectonophysics*, *427*(1–4), 231–253.
Nishida, K., H. Kawakatsu, and K. Obara (2008), Three-dimensional crustal S wave velocity structure in Japan using microseismic data recorded by hi-net tiltmeters, *J. Geophys. Res.*, *113*, B10302, doi:10.1029/2007JB005395.
Nishimura, T., T. Hirasawa, S.-I. Miyazaki, T. Sagiya, T. Tada, S. Miura, and K. Tanaka (2004), Temporal change of interplate coupling in Northeastern Japan during 1995–2002 estimated from continuous GPS observations, *Geophys. J. Int.*, *157*, 901–916, doi:10.1111/j.1365-246X.2004.02159.x.
Noda, H., and N. Lapusta (2013), Stable creeping fault segments can become destructive as a result of dynamic weakening, *Nature*, *493*, 518–521, doi:10.1038/nature11703.
Okada, Y. (1992), Internal deformation due to shear and tensile faults in a half-space, *Bull. Seismol. Soc. Am.*, *82*, 1018–1040.
Ozawa, S., T. Nishimura, H. Suito, T. Kobayashi, M. Tobita, and T. Imakiire (2011), Coseismic and postseismic slip of the 2011 magnitude-9 Tohoku-Oki earthquake, *Nature*, *475*, 373–376, doi:10.1038/nature10227.
Ozawa, S., T. Nishimura, H. Munekane, H. Suito, T. Kobayashi, M. Tobita, and T. Imakiire (2012), Preceding, coseismic, and postseismic slips of the 2011 Tohoku earthquake, Japan, *J. Geophys. Res.*, *117*, B07404, doi:10.1029/2011JB009120.
Perfettini, H., and J.-P. Ampuero (2008), Dynamics of a velocity strengthening fault region: Implications for slow earthquakes and postseismic slip, *J. Geophys. Res.*, *113*, B09411, doi:10.1029/2007JB005398.
Perfettini, H., and J.-P. Avouac (2004a), Postseismic relaxation driven by brittle creep: A possible mechanism to reconcile geodetic measurements and the decay rate of aftershocks, application to the Chi-Chi earthquake, Taiwan, *J. Geophys. Res.*, *109*, B02304, doi:10.1029/2003JB002488.
Perfettini, H., and J.-P. Avouac (2004b), Stress transfer and strain rate variations during the seismic cycle, *J. Geophys. Res.*, *109*, B06402, doi:10.1029/2003JB002917.
Perfettini, H., J.-P. Avouac, and J. C. Ruegg (2005), Geodetic displacements and aftershocks following the 2001, $M_w = 8.4$ Peru earthquake: Implications for the mechanics of the earthquake cycle along subduction zones, *J. Geophys. Res.*, *109*, B09404, doi:10.1029/2004JB003522.
Perfettini, H., et al. (2010), Seismic and aseismic slip on the central Peru megathrust, *Nature*, *465*, 78–81, doi:10.1038/nature09062.
Reinen, L. A., J. D. Weeks, and T. E. Tullis (1991), The frictional behavior of serpentinite: Implications for aseismic creep on shallow crustal faults, *Geophys. Res. Lett.*, *18*, 1687–1924.
Reinen, L. A., T. E. Tullis, and J. D. Weeks (1992), Two-mechamism model for frictional sliding of serpentinite, *Geophys. Res. Lett.*, *19*, 1535–1538.
Reinen, L. A., J. D. Weeks, and T. E. Tullis (1994), The frictional behavior of lizardite and antigorite serpentinites: Experiments, constitutive models, and implications for natural faults, *Pure Appl. Geophys.*, *143*, 317–358.
Romano, F., A. Piatanesi, S. Lorito, N. D'Agostino, K. Hirata, S. Atzori, Y. Yamazaki, and M. Cocco (2012), Clues from joint inversion of tsunami and geodetic data of the 2011 Tohoku-Oki earthquake, *Sci. Rep.*, *2*, 385.
Rundle, J. B., and H. Kanamori (1987), Application of an inhomogeneous stress (patch) model to complex subduction zone earthquakes—A discrete interaction matrix approach, *J. Geophys. Res.*, *92*(B3), 2606–2616.
Saffer, D. M., and C. Marone (2003), Comparison of smectite- and illite-rich gouge frictional properties: Application to the updip limit of the seismogenic zone along subduction megathrusts, *Earth Planet. Sci. Lett.*, *215*, 219–235.
Sagiya, T., S. Miyazaki, and T. Tada (2000), Continuous gps array and present-day crustal deformation of Japan, *Pure Appl. Geophys.*, *157*, 2303–2322.
Sato, M., T. Ishikawa, N. Ujihara, S. Yoshida, M. Fujita, M. Mochizuki, and A. Asada (2011), Displacement above the hypocenter of the 2011 Tohoku-Oki earthquake, *Science*, *332*, 1395, doi:10.1126/science.1207401.
Savage, J. C. (1983), A dislocation model of strain accumulation and release at a subduction zone, *J. Geophys. Res.*, *88*, 4984–4996.
Sawai, Y., Y. Fujii, O. Fujiwara, T. Kamataki, J. Komatsubara, Y. Okamura, K. Satake, and M. Shishikura (2008), Marine incursions of the past 1500 years and evidence of tsunamis at Suijin-numa, a coastal lake facing the Japan trench, *Geophys. Res. Lett.*, *18*, 517–528, doi:10.1177/0959683608089206.
Sawai, Y., Y. Namegaya, Y. Okamura, K. Satake, and M. Shishikura (2012), Challenges of anticipating the 2011 Tohoku earthquake and tsunami using coastal geology, *Geophys. Res. Lett.*, *39*, L21309, doi:10.1029/2012GL053692.
Scholz, C. H. (1998), Earthquakes and friction laws, *Nature*, *391*, 37–42.
Sibson, R. H. (1992), Fault-valve behavior and the hydrostatic lithostatic fluid pressure interface, *Earth Sci. Rev.*, *32*, 141–144.
Simons, M., et al. (2011), The 2011 magnitude 9.0 Tohoku-Oki earthquake: Mosaicking the megathrust from seconds to centuries, *Science*, *332*, 1421–1425, doi:10.1126/science.1206731.
Sugawara, D., K. Goto, F. Imamura, H. Matsumoto, and K. Minoura (2012), Assessing the magnitude of the 869 Jogan tsunami using sedimentary deposits: Prediction and consequence of the 2011 Tohoku-Oki tsunami, *Sediment. Geol.*, *282*, 14–26.
Suwa, Y., A. Hasegawa, T. Sato, and K. Tachibana (2006), Interplate coupling beneath NE Japan inferred from three-dimensional displacement field, *J. Geophys. Res.*, *111*, B04402, doi:10.1029/2004JB003203.
Tarantola, A. (2005), The least-squares problem, in *Inverse Problem Theory and Methods for Model Parameter Estimation*, edited by Society for Industrial and Applied Mathematics (SIAM), p. 342, Philadelphia, Pa.

Tsumura, K. (2005), *National Seismic Hazard Maps for Japan*, 162, Earthquake Res. Comm. of the Minist. of Educ. Cult. Sports Sci. and Technol. of Jpn., Tokyo, Japan.

Vergne, J., R. Cattin, and J. P. Avouac (2001), On the use of dislocations to model interseismic strain and stress build-up at intracontinental thrust faults, *Geophys. J. Int.*, *147*(1), 155–162.

Wald, D. J., and R. W. Graves (2001), Resolution analysis of finite fault source inversion using one-and three-dimensional green's functions 2. Combining seismic and geodetic data, *J. Geophys. Res.*, *106*, 8767–8788.

Wei, S., R. Graves, D. Helmberger, J.-P. Avouac, and J. Jiang (2012), Sources of shaking and flooding during the Tohoku-Oki earthquake: A mixture of rupture styles, *Earth Planet. Sci. Lett.*, *333-334*, 91–100.